Physics Reports 937 (2021) 1–73

Contents lists available at ScienceDirect

Physics Reports

journal homepage: www.elsevier.com/locate/physrep

Undulator design for a laser-plasma-based free-electron-laser

A. Ghaith [a,*], M.-E. Couprie [a], D. Oumbarek-Espinos [a,b], I.A. Andriyash [c], F. Massimo [d], J.A. Clarke [e,f], M. Courthold [g], V. Bayliss [g], A. Bernhard [h], M. Trunk [i], M. Valléau [a], O. Marcouillé [a], A. Chancé [j], S. Licciardi [k], V. Malka [c,l], F. Nguyen [k], G. Dattoli [k]

[a] Synchrotron SOLEIL, L'Orme des Merisiers, Saint-Aubin, Gif-sur-Yvette 91192, France
[b] Université Paris Saclay, Espace Technologique, Bat. Discovery - RD 128, 91190 Saint-Aubin, France
[c] Laboratoire d'Optique Appliquée, Ecole Polytechnique - ENSTA - CNRS - Institut Polytechnique de Paris, Palaiseau, France
[d] Laboratoire Leprince-Ringuet-École Polytechnique, CNRS-IN2P3, Palaiseau, F-91128, France
[e] ASTeC, STFC Daresbury Laboratory, Sci-Tech Daresbury, Daresbury, Cheshire WA4 4AD, UK
[f] The Cockcroft Institute, Sci-Tech Daresbury, Daresbury, Cheshire, WA4 4AD, UK
[g] STFC Rutherford Appleton Laboratory, Didcot, Oxfordshire, UK
[h] Karlsruhe Institute of Technology (KIT), Kaiserstr. 12, 76131 Karlsruhe, Germany
[i] Center for Free-Electron Laser Science and Department of Physics, Universität Hamburg, Hamburg, Germany
[j] CEA Saclay, F-91191 Gif-sur-Yvette, France
[k] ENEA—Frascati Research Center, Via Enrico Fermi 45, 00044 Rome, Italy
[l] Department of Physics of Complex Systems, Weizmann Institute of Science, Rehovot 7610001, Israel

ARTICLE INFO

Article history:
Received 3 November 2020
Received in revised form 16 August 2021
Accepted 6 September 2021
Available online 29 September 2021
Editor: R. Redmer

Keywords:
Undulator radiation
Free electron laser
Laser plasma acceleration
Transverse gradient undulators
Cryogenic permanent magnet undulators
Superconducting undulators

ABSTRACT

The fourth generation of synchrotron radiation sources, commonly referred to as the Free Electron Laser (FEL), provides an intense source of brilliant X-ray beams enabling the investigation of matter at the atomic scale with unprecedented time resolution. These sources require the use of conventional linear accelerators providing high electron beam performance. The achievement of chirped pulse amplification allowing lasers to be operated at the Terawatt range, opened the way for the Laser Plasma Acceleration (LPA) technique where high energy electron bunches with high current can be produced within a very short centimeter-scale distance. Such an advanced acceleration concept is of great interest to be qualified by an FEL application for compact X-ray light sources. We explore in this paper what the LPA specificities imply on the design of the undulator, part of the gain medium. First, the LPA concept and state-of-art are presented showing the different operation regimes and what electron beam parameters are likely to be achieved. The LPA scaling laws are discussed afterwards to better understand what laser or plasma parameters have to be adjusted in order to improve electron beam quality. The FEL is secondly discussed starting with the spontaneous emission, followed by the different FEL configurations, the electron beam transport to the undulator and finally the scaling laws and correction terms in the high gain case. Then, the different types of compact undulators that can be implemented for an LPA based FEL application are analyzed. Finally, examples of relevant experiments are reported by describing the transport beamline, presenting the spontaneous emission characteristics achieved so far and the future prospects.

* Corresponding author.
E-mail address: ghaith@synchrotron-soleil.fr (A. Ghaith).

https://doi.org/10.1016/j.physrep.2021.09.001

Contents

1. Introduction

The understanding of the concepts associated with spontaneous and stimulated emission, during the first half of the last century [1], was a major scientific revolution that led to the invention of the laser almost four decades later [2,3]. The origin of the LASER [4] (Light Amplification by Stimulated Emission of Radiation) traces back to the very beginning of XX-th century [5–8], with the introduction of the concept of photon by Planck leading to Einstein's prediction on energy enhancement by atom de-excitation [9] in the analysis of the black-body radiation and was later on recognized as the elementary component of the electromagnetic field itself. This breakthrough opened the possibility of conceiving optical devices capable, to a large extent, of controlling the power and associated photon beam qualities produced. The MASER (Microwave Amplification by Stimulated Emission of Radiation), where an excited NH_3 molecule is introduced in a microwave cavity resonant at the frequency of the molecule transition, was first operated in the micro-waves [10] in 1954. The "optical maser" or LASER [4] requires the use of an open Fabry–Perot type resonant cavity [1]. Lasers were then successfully operated (Ruby [11,12], He–Ne [13], GaAs [14] and others [15]). Limits in extending lasers towards very short wavelengths were pointed out. Two major new concepts arose from the laser discovery in the seventies, the free electron laser [16] and laser plasma acceleration [17]. Along with the laser technology, other sources of coherent radiation, based on traveling wave tubes, had been developed. In this case, the emission mechanism is ensured by a beam of free electrons freely propagating inside a cavity. The electron beam interacts with the modes of the cavity, gets modulated in energy and undergoes a bunching process, in which it transfers energy to one of the cavity modes (if certain kinematic conditions are satisfied [18]). This phenomena led to the construction of high efficiency powerful devices like gyrotrons, Coherent Resonance Maser, klystrons ... which are currently used in several applications in the THz, microwave and millimeter region of the spectrum. With the advent of high energy accelerators, another source of radiation known as the free electron laser emerged [16].

Free Electron Laser (FEL) devices belong to the family of coherent radiation devices [19], whose fundamental mechanism is the electron beam density bunching induced by an appropriate energy modulation [20–22]. In the FELs, in particular, the energy modulation is realized through an undulator, creating a periodic magnetic field and providing a transverse component of the electron motion and the consequent coupling to a co-propagating electromagnetic wave. The FEL transforms the kinetic energy of an electron beam into electromagnetic radiation with laser-like properties. The FEL mechanism does not rely on the stimulated emission by atomic or molecular ensembles where the population inversion is realized [23]. No quantum energy gap therefore limits the tuneability of the device, which emits in the electromagnetic spectrum with continuity from microwaves to X-rays according to the value of the period and strength of the undulator field as well as to the energy of the electron beam. Several FELs have been implemented in the last decades in various laboratories with striking results in fundamental and applied physics and have also offered unprecedented opportunities to the user community [24]. In general, FELs [25] are operated in oscillator, seeded amplification and in Self Amplified Spontaneous Emission (SASE) modes [26–31].

The choice of FEL configuration and radiation scheme is based on the user requirements of the properties of the FEL pulses, such as radiation wavelength, peak power, polarization and average repetition rate. The temporal structure of the pulse has to be matched to the characteristic timescales of physical processes under study. For X-ray imaging [32] and high intensity applications, the photons should be delivered in ultra-short high intensity pulses. On the other hand, the spectroscopic studies [33] require limited peak intensity so as to avoid non-linear processes, but also a high repetition rate in order to collect sufficient data in acceptable experimental periods.

FEL offers to the users the unique possibility of tailoring the radiation characteristics to the needs of the specific application [34]. In fact, the FEL wavelength range can be readily varied, as well as the output bandwidth [35], power, temporal structure [36–39], thus allowing a number of options including multi-frequency operation [40–45], polarization control [46,47], attosecond pulse duration [48–50], and pump and probe configurations with naturally synchronized beams.

The concept of laser electron acceleration [17] was conceived following the laser invention. Actual realization of this concept benefited from laser developments, in particular the Chirped Pulse Amplification technique [51] that enabled very high peak powers. For electron acceleration a high-power femtosecond laser pulse is focused into a gas target and resonantly drives a nonlinear plasma wave in which plasma electrons are trapped and accelerated with high energy gain gradients of 100 GeV/m [52,53]. The beginning of the twenty first century saw the advent of efficiently laser plasma accelerated electron beams [54–58]. Nowadays, electron beams with multi-GeV energies [59], femtosecond durations [60], hundreds of pC charge [61], intermediate energy spread and milliradian divergence can be produced, even though all these performance are not yet achieved simultaneously. Many of the current experimental developments are focused (or dedicated to) on overcoming this limitation. To date the beams with the record electrons energies of 8 GeV and to 0.2 mrad FWHM divergence were obtained using a 850 TW laser pulse guided in a laser-heated capillary discharge plasma [59]. The use of sharp density transition has been exploited to demonstrate a reduction of the injected electron beam's energy spread through a phase space rotation in the plasma [62]. Recently, it was also demonstrated the possibility to use a laser in a first plasma stage to drive wakefields injecting and accelerating an electron beam, to be injected in a second plasma stage, where another electron beam would be injected and accelerated [63]. This compact configuration could couple the benefits of laser driven plasma accelerators and electron beam driven plasma accelerators [64], at a high energy efficiency [65], without the need of a long conventional accelerator to generate an electron beam for a beam-driven plasma stage.

The physical schemes of beam-driven (PWFA) and laser-driven (LPA) plasma accelerators have much in common [66–68]. Indeed, both laser and particle beams can drive plasma wakefields in the blowout regime (beneficial for the quality), and for the accelerated witness bunch, the nature of the driver makes no apparent difference. For PWFA , a high current of energetic particles is not slowed down by plasma and does not lose energy via diffraction as does the laser, leading to more promising accelerator performance/efficiency defined by dephasing and driver depletion. However, the inherent complexity of the specific involved technologies makes the LPA simpler to implement. For a PWFA driven by a conventional accelerator, the features of the available beam drivers (duration $\approx$0.1–1 ps, I$\approx$1–10 kA, R $>$ 50 μm) require lower plasma densities, thus implying long acceleration distances. As a result, witness and driver beams quality become a subject to the degradation via beam–plasma interaction, e.g. hosing and streaming instabilities, transverse overfocussing and dispersion, etc. Although such pure PWFA schemes still promise higher beam quality/brightness and thus advantage in transport, but at the same time requiring GeV-class linear accelerators such schemes completely lose the potential to arrive to a truly compact SR/FEL technology. Such concepts are still under active exploration at large accelerator facilities, cf [69]. The hybrid LPA-PWFA, using LPA to compactly generate both drive and witness beams for the beam-driven stage, concepts provide yet another alternative, that is presently under development.

Combining these two technologies may open the path for a Free Electron Laser driven by a Laser Plasma Accelerator (LPA), which would be a major step towards the quest of compact, intense, and tuneable X-ray sources [70–73]. This dream is getting closer to reality, thanks to the progress on LPA performance and reliability.

The first step towards the LPA based FEL application is the observation of undulator radiation which is the FEL spontaneous emission. Indeed, several measurements, even at short wavelengths [74–82] and recently down to 4 nm [82,83] have been reported. However, the quality of the photon spectra do not yet meet what is currently achieved and utilized on synchrotron radiation based facilities in terms of spectral bandwidth, intensity and stability.

As compared to conventional accelerators, LPAs do generate in general a larger energy spread and divergence, that have to be mitigated at an early stage of the electron transport in order to avoid emittance growth [84–86]. Collective effects and coherent synchrotron radiation can also play a role [87]. The energy spread can be a real issue since it can limit the possible energy modulation and bunching required for an efficient FEL. Solutions such as energy sorting in a chicane [88] or transverse gradient undulators [89], which had been proposed during the early FEL times [90], are considered. Another method one might consider to reduce the energy spread, is by using a low density plasma dechirper [91–93]), however this technique would add an additional plasma complexity as well as an increase in the distance between the electron beam source and the first focusing elements, making the transport of the highly divergent electron beam more difficult. The LPA ultra-short electron bunches require also short undulator systems, for the photon beam not to overtake the electron beam distribution due to the slippage effect. Recent high performance LPA electron beam enabled to demonstrate a two orders of magnitude LPA based amplification at 27 nm at SIOM [94].

The path towards an LPA based FEL facility consists of several steps such as the achievement of reliable electron beam performance at the source and at the undulator entrance, the design and daily operation of an electron manipulation line, and the generation of narrow bandwidth stable undulator radiation after the electron beam transport. In such a context, the choice of the undulator must enable the overall length to be kept rather small. To avoid generating an additional challenge to the FEL success, only state of the art frontier undulator technology should be considered. Short period high field undulators are thus investigated, focusing in particular on cryogenic permanent magnet based devices and superconducting systems. In addition, the combined solution of gain amplifying medium and energy spread handling offered by the transverse gradient undulator is of particular interest.

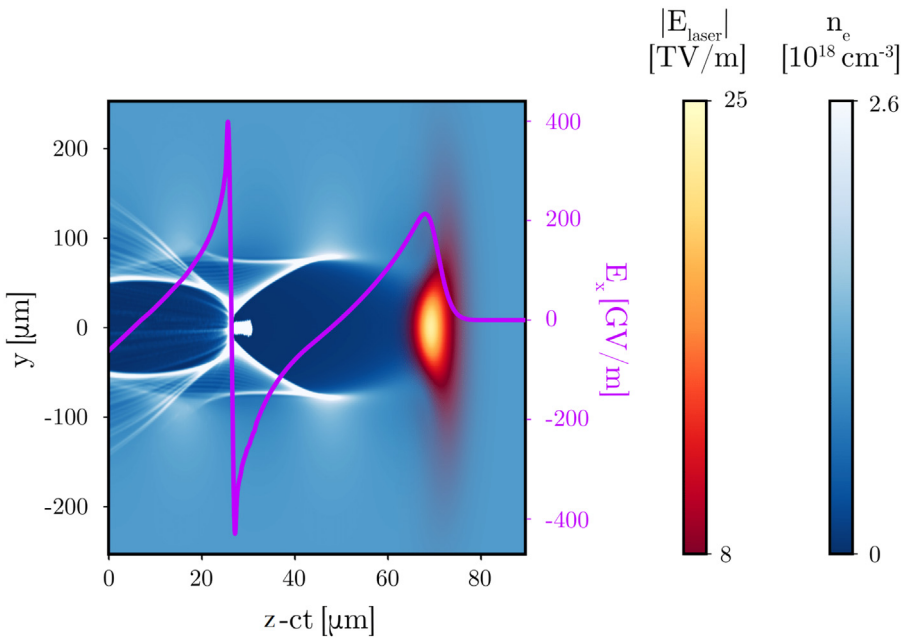

Fig. 1. Principle of LPA: a short, intense laser pulse (envelope of its electric field in the red–yellow colorbar) propagates in an underdense plasma in the positive x direction. In the wake of the laser, a relativistic plasma wave is excited (Blue–white colorbar: plasma electron density). In the wake of the laser, an electron bubble is formed (Purple line: corresponding longitudinal electric field on the propagation axis). The negative electric field at the end of the electron bubble can accelerate an electron beam in the propagation direction of the laser, creating a moving accelerating cavity for electrons. An electron beam is injected at the end of the bubble through self-injection.

We shall explore here what are the undulator choices to design an LPA-based FEL and what performance can be anticipated from the point of view of the undulator design [95]. We shall first review the LPA concepts and realizations, present the FEL theory discuss the issues associated with the use of an LPA beam and the strategies open to mitigate them. We shall then review the possible undulator technologies to be employed. In particular, we shall investigate how to push towards higher magnetic fields with shorter undulator periods, while keeping a deflection parameter value slightly larger than 1, in order to produce harmonics. Cryogenic and superconducting undulators are examined in detail. In addition, depending on the strategy chosen for handling the initial large energy spread, transverse gradient undulators are of particular interest. We shall then finish with some examples of LPA based FEL set-ups.

2. Laser plasma acceleration

2.1. Laser plasma acceleration process

Since the first proposals in the late 1970s [17], a great interest has been continuously attracted to the plasma and laser-plasma acceleration. Fig. 1 reports a particle-in-cell simulation (performed with the code Smilei [96]) of a basic LPA set up: a high intensity laser is injected into an underdense plasma, with duration and waist size of the order of the plasma wavelength. Electrons of the plasma are pushed away from the laser trajectory by its radiation pressure, and re-attracted towards their initial position by the plasma ions, almost immobile in the timescales of interest. A relativistic electrostatic plasma wave is excited, and electrons are self-injected at the end of the electron bubble and accelerated, following the laser pulse. In LPA, acceleration is produced by laser-driven electrostatic plasma waves, and, in contrast to RF cavities, the amplitudes of the generated micrometer-scale plasma fields are not limited by the DC breakdown. This allows plasma accelerators to operate thousand times higher gradients than the conventional accelerators, and thus produce extremely compact sources of bright and energetic electrons [53,97]. In 2004, the generation of hundreds of MeV, hundreds of pC electron beams with quasi-monoenergetic spectra and a few milliradian divergence were reported [98–100]. Thus LPA demonstrated its potential to become a new kind of compact electron source with beam quality suitable for the applications in the synchrotron radiation source.

Further experimental and theoretical studies of LPA helped to identify the phenomena, which define the characteristics of the accelerated beams. In the modern LPA schemes, the accelerating structure is a non-linear plasma wave following the laser pulse (called bubble or blowout region [59,100–102]) (see Fig. 1). The quality of the produced beams mainly depends on how they get injected into this structure. In the first experiments [98–100], the injection was triggered by the plasma wave deformations resulting from the laser relativistic self-focusing [103,104], and now this mechanism is known

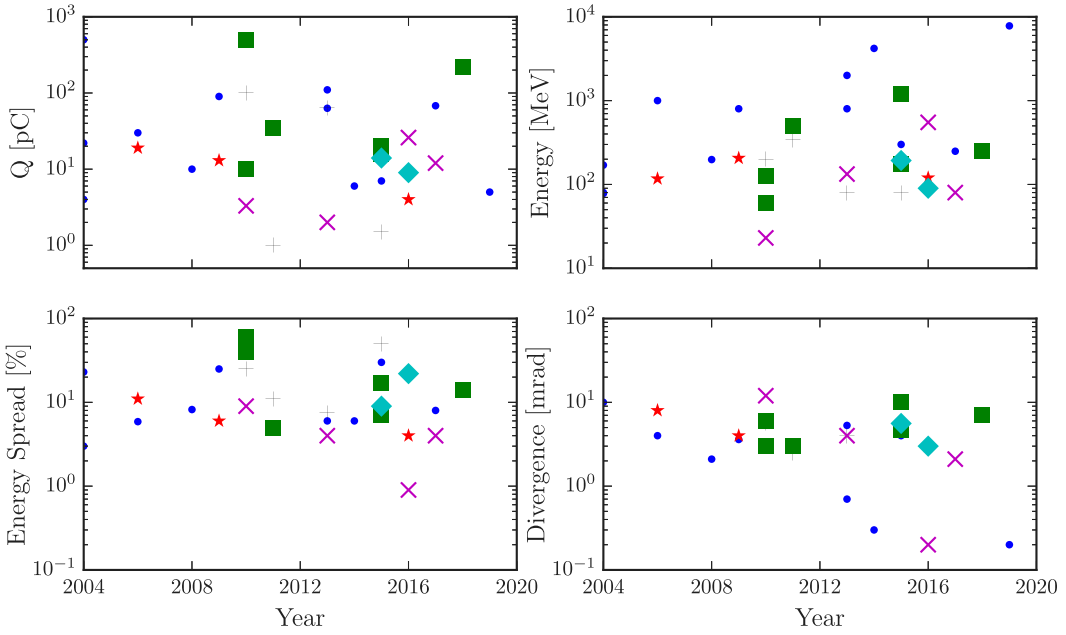

Fig. 2. Beam charge (top left), energy (top right), energy spread (bottom left) and divergence (bottom right) reported in LPA experiments obtained through different injection techniques. (●) Self-Injection [98–100,123,124,127–131], ?, [132], (★) Colliding Pulse Injection [108,109,133], (■) Ionization Injection [61,110–113,134,135], (✚) Downramp Injection [115,117,136,137], (×) Density Transition (/Shock) Injection [119,120,138,139], (◆) Downramp/Shock + Ionization Injection [121,140].

as *self-injection* [105,106]. More injection schemes have been demonstrated later, including the *optical injection* using an auxiliary laser [107–109], the *ionization injection* using the high-Z and low-Z gas mixtures [110–113], *downramp injection*, where the plasma wave is locally slowed down in a density gradient [114–118], and the *shock (or density-transition) injection* triggered at the sharp transitions of plasma density [62,119–122].

In the experimental conditions, different injection techniques can be independently realized or can also be combined to achieve the desired beam parameters. For example, self-injection is the simplest to produce, and only requires a relatively high plasma density, and hence can be used in the experiments with the capillary discharge, where the driving laser is guided. This injection technique has demonstrated the highest multi-GeV LPA electron energies to date [59,123]. Localized injection techniques, such as optical and shock injections, provide a better control of beam characteristics, i.e. divergence, mean energy and energy spread [109]. At the same time, such techniques add complexity to the experimental setup, narrowing the choice of the targets to gas jets or gas cells, thus limiting the maximal plasma density and consequently the accelerating gradients. Using the high-Z and low-Z gas-mixtures in either of these schemes adds the ionization injection, thus increasing the total accelerated charge, improving source stability [121], albeit with a higher energy spread. Presently, significant efforts are also made to separate the injection and acceleration stages in LPA, in order to establish a robust control of source performance [113,124,125]. In the near future such *multi-stage LPA* techniques promise to achieve higher energy acceleration whilst preserving beam quality. Shot-to-shot repeatability in each experiment is also an important issue to design a reliable LPA-based FEL [126].

2.2. Laser plasma acceleration performance

To give a qualitative picture of the beam parameters obtained since the *self-injection* results of 2004 [98–100,141], Fig. 2 reports, with no presumption of completeness, the beam charge, energy, energy spread and divergence documented in some articles in the literature. The depicted points come from representative works where various techniques of electron injection have been demonstrated: *self-injection* [59,98–100,123,124,127–132], *optical injection/colliding pulse injection* [108,109,133], *ionization injection* [61,110–113,134,135], *density downramp injection* [115,117,136,137], *density transition/shock injection* [119,120,138,139], *density downramp or shock assisted ionization injection* [121,140]. The definitions of the electron beam parameters might slightly vary with authors and measurement methods. Also, only parameters averaged over those of similar shots were considered, where possible. The reported parameters in the literature in general address most likely the whole-beam parameters or those of the electrons in a spectrum peak, rather than the slice parameters, of interest for the FEL application.

It should be noted that, while the state-of-the-art LPA beam characteristics (i.e. multi-GeV energies, hundreds pC charge, sub-percent energy spread and sub-milliradian divergence) have already been experimentally demonstrated, their

simultaneous reproduction and stable operation remains extremely challenging. Practically, the choice of the LPA setup with proper injection method is fundamental for a given application, as it should not only generate the beams of desired quality, but should also be reproducible and robust in the operation.

2.3. LPA scaling laws

As mentioned above, LPA process exploits the fields of the laser-driven plasma waves. The phase velocity of these waves, and of the associated accelerating field is determined by the laser group velocity. In a tenuous plasma, this velocity is close to the speed of light, $v_{\rm ph} \simeq c$. In LPA, a laser pulse acts on plasma mainly via the *ponderomotive* force, $\mathbf{F}_p = -m_e c^2 \nabla \langle |\mathbf{a}_l|^2 \rangle / (2\gamma)$, where a_l is the laser vector potential normalized to $m_e c/e$, γ is the electron Lorentz factor, and $\langle\rangle$ denotes averaging over one laser period. This nonlinear force drives charges towards the areas with the lower field amplitudes. For the moderate field amplitudes laser can generate the electron density fluctuations $\delta n_e \sim a_0^2 n_p$, where n_p is the electron plasma density, and a_0 is the peak value of the normalized laser vector potential. From this follows, that for $a_0 < 1$, plasma waves remain linear, i.e. $\delta n_e \ll n_p$, while the higher fields, $a_0 > 1$, can lead to the electron blow-out from the wave nodes, and formation of the so-called *bubbles*.

Linear regime. The accelerating field generated by a linear wave with the density modulation amplitude δn_e has the amplitude $E_z = m_e c \omega_p \delta n_e / e n_p$, where $\omega_p = \sqrt{4\pi r_e c^2 n_p}$ is the plasma frequency, and r_e is the classical electron radius. To describe the plasma wave excitation in details, one may consider a set of Maxwell equations for the vector and scalar potentials $\mathbf{a}$ and ϕ, assuming the Lorenz gauge:

$$\begin{aligned} &(\partial_t^2 - c^2\nabla^2)\mathbf{a} = -4\pi r_e c^2 \mathbf{j}_e\,, \\ &(\partial_t^2 - c^2\nabla^2)\phi = 4\pi r_e c^2 (n_i - n_e)\,, \\ &\partial_t \phi + c\nabla\cdot\mathbf{a} = 0\,, \end{aligned} \tag{1a}$$

coupled with the equations for the cold non-relativistic electron fluid (ions can be assumed immobile),

$$\begin{aligned} &\partial_t n_e + \nabla\cdot(n_e \mathbf{v_e}) = 0\,, \\ &\partial_t \mathbf{p_e} + (\mathbf{v_e}\cdot\nabla)\mathbf{p_e} = \partial_t \mathbf{a} + c\nabla\phi - \mathbf{v_e}\times\nabla\times\mathbf{a}\,. \end{aligned} \tag{1b}$$

where n_i is the ion density, and ϕ is the electrostatic potential normalized to $m_e c^2/e$, $\mathbf{j}$ is the current density normalized as $\mathbf{J}/ec$, and the momentum of the electron fluid p_e is normalized to $m_e c$.

When following the laser pulse, the plasma perturbations and the laser pulse itself change slowly compared to the laser field oscillations, and to the plasma collective response. It is then convenient to introduce the *phase* coordinate $\xi = ct - z$, which follows the driver beam and re-write Eqs. (1) in terms of (t, ξ). With that, one can assume $\partial_t \ll c^{-1}\partial_\xi$, and drop all dependencies on the "slower" variable t, thus considering all values to be the functions of only ξ. This is known as the *quasi-static approximation*.

Another useful approximation is to assume that the *fast* and *slow* ξ-dependencies in Eqs. (1) can be linearly decoupled, i.e. that each function can be presented as a sum, $\mathbf{a} = \mathbf{a}_f + \mathbf{a}_s$, where $\partial_\xi \mathbf{a}_f \gg \partial_\xi \mathbf{a}_s$. This is known as the *ponderomotive formalism*, and it allows to distinguish the *slow* dynamics associated with the plasma response. In most cases one may attribute all fast varying fields to the laser, $a_f = a_l$, and its action on this time scale appears as the cycle-averaged ponderomotive force.

The slow components of Eqs. (1) can be used to describe the excitation of the wakefield by a laser. It is also convenient to replace the 3-component vector potential $\mathbf{a}$, by the scalar pseudo-potential $\psi = \phi - a_z$, and the transverse components $\mathbf{a}_\perp$. The resulting equations for the potentials read:

$$\begin{aligned} &\nabla_\perp^2 a_{s,\perp} = 4\pi r_e j_{s,\perp}\,, \\ &\nabla_\perp^2 \psi_s = 4\pi r_e (n_s - n_p - j_{s,z})\,, \\ &\nabla_\perp^2 \phi_s = 4\pi r_e (n_s - n_p)\,, \\ &\partial_\xi \psi_s + \nabla_\perp a_{s,\perp} = 0\,. \end{aligned} \tag{2a}$$

where the subscript "e" has been dropped as only electron density and motion is considered. Application of the discussed approximations to equations of electron motion is less straightforward, and requires additional approximations which are not discuss here. For the sake of completeness, one can provide only the final expressions:

$$\begin{aligned} &\partial_\xi p_{s\perp} = \partial_\xi a_{s\perp} + (\gamma_s/(1+\psi_s) - 1)\nabla_\perp \psi_s + \\ &+ \nabla_\perp \phi_s - 1/(1+\psi_s)\nabla_\perp \langle a_l^2\rangle/2\,, \\ &\partial_\xi r_s = p_{s\perp}/(1+\psi_s)\,, \\ &p_{sz} = \gamma_s - 1 - \psi_s\,, \end{aligned} \tag{2b}$$

where γ_s is electrons Lorentz factor and r_s is the radial coordinate. A rigorous and complete derivation of these equations can be found in [142].

In the linear case, all values associated with the wave can be considered to be small (a, $\delta n_e/n_p$, ψ, $\mathbf{j}$, p, etc.). Retaining only the first-order terms, Eqs. (2) can be simplified leading to the equation for the wakefield potential:

$$\partial_\xi^2 \psi + k_p^2\, \psi = k_p^2 \langle |\mathbf{a}_l|^2 \rangle / 2\,, \tag{3}$$

where $k_p = \omega_p/c$ is the wavenumber of the relativistic plasma wave. Eq. (3) has a well-known solution:

$$\psi = k_p/2 \int_{-\infty}^{\xi} \langle |\mathbf{a}_l(\xi')|^2 \rangle \sin[k_p(\xi - \xi')] \mathrm{d}\xi'\,. \tag{4}$$

In Eq. (4), one can see that the laser profile is convoluted with the plasma wave. For a short pulse, this allows for the resonance, when the laser duration is close to the plasma period. In the case of a Gaussian pulse profile with FWHM duration τ_l, this resonance condition can be written more accurately, as $\tau_l = 2\,\omega_p^{-1}\sqrt{2\log 2} \simeq 2.35/\omega_p$, and the generated wakefields read:

$$\begin{aligned} E_z &= \eta a_0^2 mc\omega_p/4e \cos[k_p(\xi - \xi_l)] \exp(-2r^2/w_0^2)\,, \\ E_r &= \eta a_0^2 mc^2 r/e w_0^2 \sin[k_p(\xi - \xi_l)] \exp(-2r^2/w_0^2) \end{aligned} \tag{5}$$

where a_0 is the laser field amplitude, w_0 is the beams waist, r is the distance to the laser axis, and coefficient $\eta = \sqrt{2\pi/\exp(1)} \simeq 1.52$.

In the end of 1980's, the chirped-pulse amplification made the ultra-short high-power laser pulses available [51], and has stimulated the interest to this resonant linear wakefield regime [143,144]. In this early concept, the acceleration is limited mainly by the laser diffraction, and by the *dephasing* of electrons with the accelerating field. The energy gained by the electrons, in a case when the laser freely diffracts (no guiding), as derived in [145], reads:

$$W_e\,[\mathrm{MeV}] \simeq 580 (n_p/n_c)^{1/2} P\,[\mathrm{TW}]\,, \tag{6}$$

where P is the laser power, and $n_c = 1.1 \times 10^{21}/\lambda_0[\mu\mathrm{m}]\ \mathrm{cm}^{-3}$ is a plasma density critical for the laser wavelength λ_0. The acceleration distance in Eq. (6), is provided by the laser Rayleigh length $L_R = \pi w_0^2/\lambda_0$ (for a Gaussian beam), which is typically short. The final energy gained by an electron is simply proportional to the field Eq. (5), and therefore increases as the square root of the plasma density.

In a situation, when laser is guided and does not diffract, the acceleration is defined by the electrons dephasing from the wakefield. This dephasing (or detuning), is determined by the laser group velocity in plasma, which is sub-luminal, $v_g/c \approx 1 - n_p/2n_c$. The total energy gain of electrons is limited by (see [66]):

$$W_e\,[\mathrm{GeV}] \simeq I[\mathrm{W/cm^2}]/n_p[\mathrm{cm^{-3}}]\,, \tag{7}$$

and one may see, that in this case, it is inversely proportional to the plasma density.

Bubble regime. Further development of the high-power lasers has demonstrated the ultrashort pulses with much higher intensities, $a_0 \gg 1$, thus enabling a purely nonlinear regime of laser plasma interaction. In this, so-called bubble or blow-out regime, the laser pulse acts as a *snowplow* for the plasma electrons, expelling them sideways and leaving the bare ion cavity in the wake [146]. It turns out that such interaction provides a better quality of the accelerated beam, and more importantly a few mechanisms of injection of the plasma electrons into the wake. This makes such accelerators self-consistent, and presently the blow-out LPA is a mainline regime in the experimental studies and for applications.

It was shown that in the bubble regime, the longitudinal resonance between plasma and the laser pulse is no longer sensitive to the pulse profile or amplitude. In most practically interesting cases, to maintain stable bubble, it is enough for the laser pulse to be shorter, than the bubble itself, $\tau_l < \omega_p^{-1}$. On the other hand, the transverse laser size (radius) becomes very important, as it now determines the bubble structure and the laser propagation dynamics. The balance of the ponderomotive and electrostatic forces in the bubble leads to the matching condition $k_p w_0 \approx \sqrt{a_0}$, which was formulated and validated numerically in [147] (for a circularly polarized laser). This matching was further validated in [148], where a more refined coefficient was provided as:

$$k_p w_0 \simeq 2\sqrt{a_0}\,, \tag{8}$$

and it was shown that indeed this condition corresponds to an "optimal" interaction (linearly polarized laser).

One obstacle on the way to develop a self-consistent description of the blown out plasma is to accurately describe the electron motion. In this highly nonlinear regime, electron trajectories are crossing behind the bubble and the fluid description Eqs. (1b) is no longer valid. Although it is possible to have a kinetic model based on the linearization of electrons motion [142], describing analytically the currents near the bubble boundaries (sheath) in the general case is challenging. Descriptions of the nonlinear wake are typically based on the approximate theoretical models complemented phenomenologically, and with the help of the particle-in-cell simulations [102,147,149]. Regardless of its exact shape, within the bubble it is possible to find the longitudinal wakefield as:

$$E_z = m_e \omega_p^2/2e\,(\xi - \xi_c)\,, \tag{9}$$

where ξ_c is the phase coordinate where the bubble radius is largest (in spherical case the center of ion cavity). The transverse force acting on the particles in the bubble is electromagnetic, and in contrast to the one in the linear wake, it is always focussing and does not depend on the longitudinal position:

$$F_r = m_e\omega_p^2 r/2\,. \tag{10}$$

A systematic review on the derivation of the regimes can also be found in [150].

In contrast to conventional linacs, where injection and acceleration are separated and the accelerating phase is maintained precisely, the features of today's LPA are much less controllable. Performance of the LPA sources is determined by the laser propagation in plasma, and is affected by the laser self-focussing, diffraction, depletion, dispersion, pulse compression etc. The characteristics of LPA electrons injected via the plasma wave-breaking process can be approached from the similarity theory, which is valid under a number of assumptions [147]. The estimates of the maximum electron energy and the number of accelerated electrons following from this model read:

$$\begin{aligned} W_e &\approx 0.65 m_e c^2 (c\tau/\lambda_0)\sqrt{P/P_r}\,, \\ N_e &\approx 1.8/(k_0 r_e)\sqrt{P/P_r}\,, \end{aligned} \tag{11}$$

where λ_0 is the laser wavelength, and $P_r = m_e^2 c^5/e^2 \simeq 8.7$ GW is a unit relativistic power (constants are in Gaussian units).

An alternative phenomenological approach was considered in [148]. It is based on the optimal choice of parameters including the aforementioned transverse laser matching Eq. (8), the power required for the relativistic self-guiding $P \gtrsim P_c = 17\omega_0^2/\omega_p^2$ GW (cf [104]), and it accounts for the laser depletion, and electron-wake dephasing. Laser depletion length is a fundamental limit of the LPA performance, and it results from a nonlinear processes of laser absorption and diffraction at the front of the pulse. The semi-phenomenological estimate of the depletion length, given in [151] and validated numerically, reads:

$$L_{\mathrm{depl}} \approx \omega_0^2/\omega_p^2\, c\tau_l\,, \tag{12}$$

where τ_l is the full width at half maximum pulse duration. The second factor is the dephasing of electrons in the wake, due to the laser slow-down in plasma. The wake's phase velocity is determined by the laser group velocity, $v_{\mathrm{las}}/c \simeq 1 - \omega_p^2/2\omega_0^2$, and by the laser depletion rate (so-called etching). In [148] dephasing is estimated as:

$$L_{\mathrm{deph}} \approx 2\omega_0^2/3\omega_p^2\, R\,, \tag{13}$$

where the radius of the bubble is around half of the laser waist $R \simeq w_0/2$.

Under the all-optimal conditions, the obtained scaling of electron energy and number is:

$$\begin{aligned} W_e &\approx m_e c^2 (n_c/n_p)^{2/3} (P/P_r)^{1/3}\,, \\ N_e &\approx 0.53/(k_0 r_e)\sqrt{P/P_r}\,. \end{aligned} \tag{14}$$

Note, that the energy scaling in Eqs. (14) depends on the plasma density, and this can be further simplified depending on the laser guiding strategy. In the case of a pre-created plasma channel [66], no self-guiding is required and the plasma density should be chosen to satisfy the requirements for the blow-out intensity $a_0 > 2$, transverse matching $k_p w_0 \simeq 2\sqrt{a_0}$, and to avoid strong relativistic self-focussing $P \sim P_c$. Otherwise, in an homogeneous plasma, laser guiding beyond the Rayleigh length requires relativistic self-guiding, thus adding a constraint $P \gg P_c$. For more details on the underlying optimal conditions see [148].

The provided scalings cover a wide range of laser and plasma parameters. For the laser energies extending from <1 J obtained in the table-top lasers to 100 J achieved at the large systems, the values of typical acceleration lengths vary from a few millimeters to tens of centimeters, resulting in the electron energies from a few MeVs to GeVs. Practically, for each particular case the choice of the optimal laser optics and gas-target parameters involves the detailed PIC modeling. An example of one such numerical experiment will be presented in the following section.

Besides the mean particles energy, another critical parameter for the undulator radiation is the electron beam brightness, which is translated to the brightness of the synchrotron radiation source. Most generally, beam brightness is defined by the density of electrons in the 6D phase-space $(\mathbf{r}, \mathbf{p})$. For the conventional beams, the brightness is characterized by their longitudinal and transverse emittance (the phase-space integral), which are typically conserved in beam transport. In LPA, the size of the accelerated beam is very small (few micrometers), while its longitudinal and transverse momenta spreads can be very high ($\Delta p_{\parallel,\perp} \gg 1$). Therefore, while the intrinsic beam emittance can be rather low [152–154], it may change during beam extraction and along its transport [84,85,155].

Since the focussing force Eq. (10) does not depend on the electrons longitudinal position in the plasma bubble (phase), the transverse momenta spread is preserved during the LPA process. Emittance degradation due to the beam extraction and drift can be minimized by carefully tailoring the plasma density profile at the plasma exit [156], and beam further focussing using the compact magnetic [78,157] or plasma-based [158–160] devices. Discarding the emittance degradation processes, its scaling may be defined from the spread of electron transverse momenta acquired during the injection. The maximum transverse momentum of an electron in the bubble is related to its excursion and its energy as,

$p_{\perp max} = k_p r_{max}\sqrt{\gamma/2}$. For a beam injected with a radius R_b and $\gamma_e \sim 1$, this leads to the scaling of the minimum value $\Delta p_\perp \sim 0.1\, R_b\ [\mu\text{m}]\sqrt{n_p[10^{18}\ \text{cm}^{-3}]}$. The beam radius varies depending on the injection process, and for example, in the case of ionization injection, R_b is defined by the radius of the cylinder where laser field surpasses the ionization threshold.

When considering the spread of the longitudinal momenta, one must account for the dependency of accelerating field Eq. (9) on electron position with respect to the center of the bubble. For a finite-duration LPA beam this leads to the correlations (chirp) in the (z, p_z) phase-space, and hence a large total energy spread. In some cases it is possible to tailor the plasma density profile to compensate for the chirp [62], or to carefully tune the quantity of the injected charge in order flatten accelerating field structure with electrons space-charge fields (beam-loading) [61]. For now, it is not yet clear which will be the best way to maintain the low energy spread in the real-life LPA applications, and this is a subject of active.

2.4. Numerical description of laser plasma acceleration

Numerical modeling provides a detailed insight into the complex nonlinear kinetic phenomena of injection and acceleration in LPA. Since the 1960–1970s, the Particle-in-Cell (PIC) method has become a mainline approach to simulate the plasma kinetics [161,162], and presently it includes a large variety of numerical techniques to model laser-plasma interactions [163].

In PIC codes, the plasma particle species are described by ensembles of macro-particles. Each macro-particle represents a large number of real particles (electrons, protons, ions) and is advanced in time using the so-called *pusher* algorithms (e.g. [164,165]). Thus, the macro-particle motion describes the evolution of the plasma distribution function in a continuous phase space. Electric and magnetic fields are sampled on a numerical grid, and are advanced in time using Maxwell's equations via the algorithms called *Maxwell solvers*. Typically, Maxwell solvers implement Finite Difference Time Domain (FDTD) integration methods [166,167]. The macro-particle phase spaces and fields numerical grid are interfaced via interpolation techniques, either classical [163] or specially adapted to explicitly preserve the charge continuity [168].

When modeling propagation of a laser pulse over a significant distance, the numerical accuracy becomes very important and should include self-consistently three-dimensional effects [169]. Practically full 3D simulation may result in a prohibitive cost in terms of computational resources. On the other hand, a naturally high level of cylindrical symmetry in LPA allows to significantly accelerate such simulations by using the azimuthal Fourier decomposition of the electromagnetic fields and current density (defined on a $r-z$ grid). It was shown that, retaining enough azimuthal modes one can obtain predictions with a 3D-like accuracy [170], and this approach is now known as quasi-cylindric modeling geometry.

Another way to make a large LPA simulation more accessible is to consider it in a *Lorentz-boosted* reference frame. In a frame which co-propagates with the laser pulse, the lengths and the frequencies of laser and plasma approach each other, and in many cases the numerical cost of a simulations can be greatly reduced [171]. Such simulations contain streaming plasma, and turn out to be very sensitive to the numerical dispersion produced in FDTD Maxwell solvers, which artificially slows down electromagnetic waves. In the laboratory frame simulations, numerical dispersion affects the electron injection in LPA, and also allows for the numerical Cherenkov radiation (NCR) [172], which significantly increases the accelerated beam emittance. In many cases these effects can be reduced by modifications of the numerical differential operators [173,174]. In a Lorentz-boosted frame, the NCR growth in relativistic streaming plasma is very fast, and such simulations require the numerical-dispersion-free solvers, e.g. one of the pseudo-spectral analytical time-domain (PSATD) solvers [175–177], or the 1D-dispersionless rhombi-in-plane solver [178].

Let us now consider a numerical LPA experiment restricting it to be fully cylindrically symmetric, so that it can be resolved with the quasi-cylindrical geometry using only first two azimuthal modes. Laser and plasma parameters are equivalent to the ones in [179]: a linearly polarized Gaussian laser pulse with $a_0 = 4.3$, wavelength $\lambda_0 = 2\pi c/\omega_0 = 0.8$ −m and 25 fs FWHM duration is focused to the waist of $w_0 = 30$ −m into the pre-ionized uniform plasma with $n_p = 8.62 \times 10^{17}\ \text{cm}^{-3}$, which starts with a linear 0.5 mm ramp. Note, that these particular parameters do not match exactly the condition Eq. (8), but are chosen so that the interplay of laser self-focusing and diffraction leads to its self-guiding over a long distance. We have run the corresponding numerical simulations in the laboratory and in the Lorentz-boosted reference frames. For the former we have used the quasi-cylindrical FDTD PIC code CALDER-CIRC [170] with the anti-Cherenkov stencil [180], and for the latter we have used a quasi-cylindrical PSATD code FBPIC [177] with the boost Lorentz factor of $\gamma_{\text{boost}} = 8$. The numerical mesh in the simulations has the longitudinal and radial cell-sizes $\Delta z = 0.125\ c/\omega_0$ and $\Delta r = 1.5\ c/\omega_0$, and plasma is modeled as electron and proton species presented by 100 macro-particles per cell per species.

Fig. 3a plots the evolution of electron energy spectrum $\text{d}N_e/\text{d}W_e$ (red colors) and the laser normalized field amplitude $eA_{\text{max}}/m_e c$ (blue curve) along the propagation of 14 mm. As one can observe, after ∼1 mm propagation laser self-focuses and triggers intense electron injection which proceeds for ∼2 mm. Injection results in a total charge of the bunch of 0.8 nC, and it seizes after laser reaches its peak amplitude of $eA_{\text{max}}/m_e c = 7.2$. After the injection, electron beam is accelerated in the co-propagating linear field of the bubble Eq. (9), which remains stable thanks to the laser guiding. From the electron spectral evolution in Fig. 3a, one can see that eventually the energy growth deviates from the linear law, and the acceleration rate starts to decrease. This is due to dephasing described by Eq. (13), that limits the overall

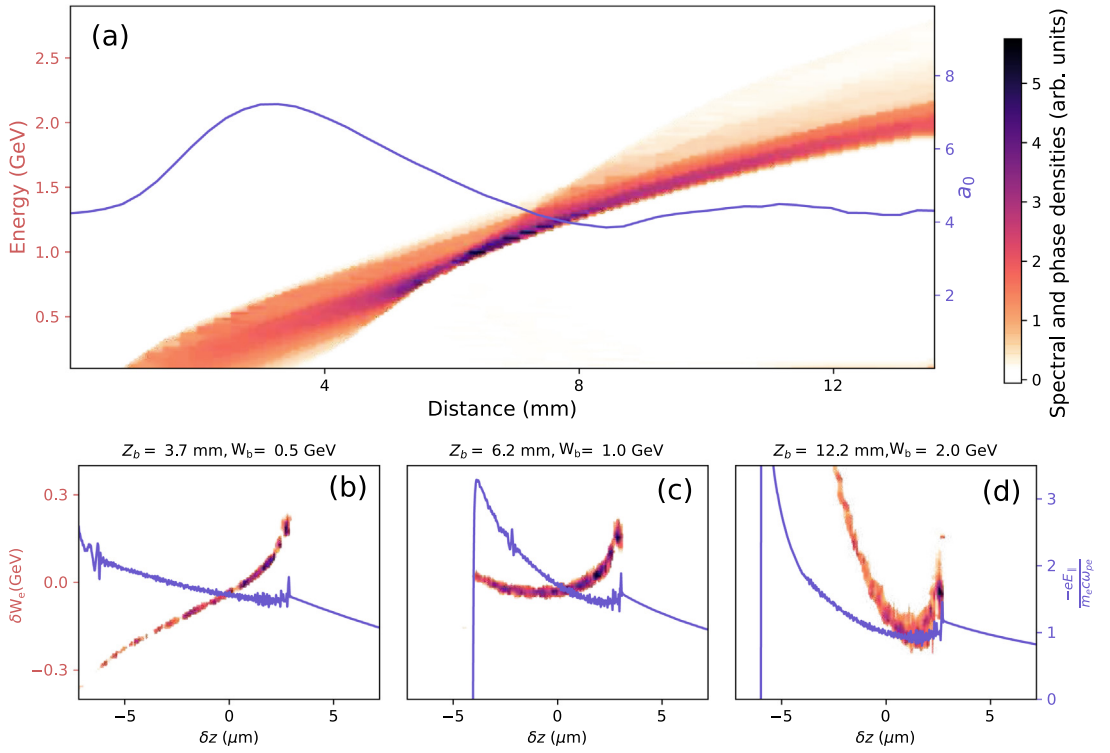

Fig. 3. (a) Evolution of laser normalized field amplitude $a_0 = eA_{\max}/m_e c$ (blues curve), and electron spectrum dN_e/dW_e (red colors) along the propagation. (b, c, d) Electron density in the phase space $(\delta z, \delta W_e)$ (red colors), and distribution of the accelerating force $F_z = -eE_z/m_e c\omega_p$ (blue curve) at three particular positions.

acceleration length by $L_d = 20$ mm. For this interaction parameters, the LPA beam charge and maximum energy provided by Eqs. (11) are 3.3 nC and 0.8 GeV, respectively, while Eqs. (14) provide the more accurate estimates of 1 nC and 3.2 GeV.

Looking into the electrons spectral profile in Fig. 3a, one may note, that the initially broad spectrum gradually narrows with propagation, reaches its thinnest point at ∼6.5 mm, and then starts to broaden again. In Fig. 3b–d, one can see the electrons longitudinal phase distribution $(\delta z, \delta W_e)$ at three specific moments: right after the injection (b), at the point of narrowest spectrum (c), and later when beam approaches dephasing. It is clear, that evolution of the total energy spread observed in Fig. 3a is related to electrons rotation in the longitudinal phase. This dynamics is due to the linear dependency of the accelerating force shown by the blue curves in Fig. 3b–d. One may consider this dynamics as a way to tune the LPA for the best beam quality. In this example, one may consider extracting the beam at ∼6.5 mm to obtain the mean energy of 1 GeV and the minimal energy spread of 4 % (FWHM). It is also clear that the local, "slice" energy spread is much lower that its projected value and is of the order of ∼1 %.

The energy and charge characteristics described by the FDTD laboratory frame and PSATD boosted frame simulations are almost identical. On the other hand, the transverse or angular bunch features described by two models turn out to differ significantly. The PSATD model estimates the projected emittances of the bunch within the bubble as $\sigma_x = 40$ nm and $\sigma_y = 100$ nm (y-axis is along laser polarization), while the FDTD code gives the much higher values $\sigma_x = 0.6$ μm and $\sigma_y = 1.2$ μm. This discrepancy is explained by the remaining numerical Cherenkov radiation, which is still present in the FDTD code and leads to the emittance growth. Practically, even the larger emittance estimates are rather low if compared to the values measured in the experiments. This is the result of the physical emittance growth which occurs when the beam leaves the plasma. While in plasma the beams transverse quality is preserved by the strong focusing plasma fields, at the extraction its emittance grows rapidly and thus should be treated with specialized beam optics [85].

The presented numerical analysis gives a rather qualitative description of LPA and is not aimed to provide the benchmark parameters for the application design. To describe an experimental case, a more detailed modeling would require inclusion of the realistic non-Gaussian laser profiles, gas ionization and higher-order asymmetries. Such an account would significantly affect the final beam parameters [181]. The recent development of advanced diagnostics for the complete spatio-temporal characterization of ultra-intense femtosecond laser pulses [182] will likely enable a more precise simulation of the initial experimental conditions in the coming years. Nevertheless, simulations with more experimentally accurate laser profiles will likely need increased spatial resolution and will thus demand more computational resources.

3. Free electron laser

In view of designing an LPA based FEL, the FEL process is described here, paying particular attention to the concept, FEL scaling laws, and electron beam transport to the undulator.

3.1. Undulator radiation : the FEL spontaneous emission

The theoretical foundations of synchrotron radiation, the electromagnetic radiation emitted by accelerated charged particles, have been established at the end of the nineteenth century [183,184] and developed further [185–191]. After the measurement of particle energy loss [192], synchrotron radiation was first observed in the visible range [193]. Radiation emitted by relativistic electrons performing transverse oscillations was first considered in 1947 [194]. The electromagnetic field created by a relativistic particle in a periodic permanent magnetic field (such as produced by undulators) [195,196] was calculated and observed [197,198].

A single relativistic electron of given energy E traversing a planar undulator that generates a sinusoidal magnetic field in one plane of period λ_u [199–208]:

$$\vec{B_u} = B_u \cos\left(\frac{2\pi}{\lambda_u} z\right) \vec{y} \tag{15}$$

emits radiation at each half period in the forward direction. The radiation adds constructively resulting in a peaked spectrum around the resonant wavelength λ_r and it has harmonics n expressed as :

$$\lambda_r = \frac{\lambda_u}{2n\gamma^2}\left(1 + \frac{K_u^2}{2} + \gamma^2\theta^2\right) \tag{16}$$

where $\gamma = E/mc^2$ is the Lorentz factor, θ the angle of observation and K_u the undulator deflection parameter defined as:

$$K_u = \frac{eB_u\lambda_u}{2\pi mc} \tag{17}$$

B_u being the peak value of the on-axis magnetic field and e, m and c respectively the electron charge, the electron mass and the speed of light. The radiation is tuneable by changing either the magnetic field or the electron energy. The deflection parameter K_u determines the radiation characteristics captured by the window of observation.

The radiation is well collimated, being emitted in a narrow cone of aperture $\sim K_u/\gamma$ in the plane of the electron oscillations and $\sim 1/\gamma$ in the plane without oscillations (case of a planar undulator). The on-axis undulator radiation is polarized, following the plane where the electrons are wiggling due to the Lorentz force, i.e. for a planar undulator generating a vertical sinusoidal field, the polarization is in the horizontal plane.

An elliptically polarized undulator can generate a magnetic field in both the vertical and horizontal planes, with a phase difference between the two. The resonant wavelength is the same as in Eq. (32) with $K_u^2 = K_{ux}^2 + K_{uy}^2$. In the case of a helical undulator with identical deflection parameter in both planes, the resonant wavelength becomes $\lambda_r = \frac{\lambda_u}{2n\gamma^2}(1 + K_u^2 + \gamma^2\theta^2)$.

3.1.1. Homogeneous linewidth

An electron passing through an undulator with N_u periods produces a wavetrain with equal number of oscillations. The electric field of the light wave is written as:

$$E(t) = \begin{cases} E_0 \exp(i\omega_r t) & \text{if } -T/2 < t < T/2 \\ 0 & \text{Otherwise} \end{cases} \tag{18}$$

with the time duration of the wave $T = N_u\lambda_r/c$. Due to its finite length, this wavetrain is not monochromatic but spans over a range of frequencies. This range can be determined by applying the Fourier transformation to the electric field:

$$E(\omega) = \frac{E_0}{\sqrt{2\pi}} \int_{-T/2}^{T/2} e^{i\Delta\omega t} dt \qquad \text{with} \quad \Delta\omega = \omega_r - \omega$$

$$\text{Thus :} \quad E(\omega) = \frac{2E_0}{\sqrt{2\pi}} \frac{\sin \Delta\omega T/2}{\Delta\omega}$$

The spectral intensity $S(\nu)$ is proportional to $|E(\omega)|^2$:

$$S(\nu) \propto \left(\frac{\sin \nu/2}{\nu/2}\right)^2 \tag{19}$$

with

$$\nu = 2\pi N_u \frac{\omega_r - \omega}{\omega_r}$$

The undulator relative homogeneous bandwidth can be approximately estimated as the spectral distance between the two dark fringes on the first harmonic and is expressed as:

$$\left[\frac{\Delta\lambda}{\lambda}\right]_n = \left[\frac{\Delta\omega}{\omega}\right]_n \approx \frac{1}{N_u} \tag{20}$$

where n index stands for the natural line width. For an undulator with 100 periods, the first harmonic natural line width is 1%. A real electron beam widens the undulator bandwidth due to the multi-electron contribution (emittance and energy spread) and reduces the radiated intensity.

3.1.2. Natural beam size and divergence

To examine the natural divergence of the radiation, Eq. (16) can be written in the form of:

$$\frac{\lambda - \lambda_r}{\lambda_r} = \frac{\lambda_u \theta^2}{2\lambda_r} \tag{21}$$

Setting Eq. (21) equal to the natural linewidth in RMS ($\approx \frac{1}{2N_u}$), one gets the natural divergence RMS of the photon beam in one plane σ_n':

$$\sigma_n' = \sqrt{\frac{\lambda_r}{L_u}} \tag{22}$$

where L_u is the undulator length. The photon beam natural divergence is 316 μrad for a resonant wavelength of 200 nm and an undulator length of 2 m.

The photon beam emittance ε_{nv} emitted by a single electron is often considered to be equal to the diffraction limit [207]:

$$\varepsilon_{nv} = \sigma_n' \sigma_n = \frac{\lambda_r}{4\pi} \tag{23}$$

Substituting the natural divergence in Eq. (23), the natural beam size RMS is found to be:

$$\sigma_n = \frac{1}{4\pi}\sqrt{\lambda L_u} \tag{24}$$

The photon beam natural size is ∼50 μm for a resonance wavelength of 200 nm and an undulator length of 2 m. Other expressions of the natural divergence and beam size can be found in [209–212].

3.1.3. In-homogeneous broadening

The multi-electron contribution, due to the emittance and energy spread, widens the undulator linewidth. The energy spread σ_ε widens the line symmetrically. By deriving Eq. (16) at $\theta = 0$, one gets:

$$d\lambda = -\frac{\lambda}{2\gamma^2}(1 + K_u^2/2)\left(\frac{2d\gamma}{\gamma}\right)$$

Thus

$$\left[\frac{\Delta\lambda}{\lambda}\right]_{\sigma_\varepsilon} = 2\frac{d\gamma}{\gamma} = 2\sigma_\varepsilon \tag{25}$$

For energy spread of 0.2% RMS, the contribution on the bandwidth is ∼0.94% FWHM close to the natural linewidth of the 100 period undulator case.

The divergence $\sigma_{x,z}'$ causes a red shift of the resonant wavelength and widens the bandwidth asymmetrically.

$$\lambda = \frac{\lambda_u}{2\gamma^2}(1 + K_u^2/2) + \frac{\lambda_u}{2}\theta^2$$

The deviation of the radiation wavelength with respect to the on-axis case ($\theta = 0$) is:

$$\lambda - \lambda_{res} = \Delta\lambda = \lambda\gamma^2\theta^2/(1 + K_u^2/2)$$

Therefore:

$$\left[\frac{\Delta\lambda}{\lambda}\right]_{\sigma_{x,y}'} = \frac{\gamma^2\sigma_{x,y}'^2}{1 + K_u^2/2} \tag{26}$$

A 0.2 mrad RMS divergence contribution on the bandwidth is ∼1.2% FWHM for an energy of 200 MeV and K_u of 2, slightly bigger than the natural line width of a 100 period undulator.

For short period undulators with small gaps, the field variation in the vertical axis broadens the bandwidth especially when the vertical beam size is quite large. For very small deviations in the vertical position, the undulator field can be expressed as $B_u \propto \cosh(k_u z) \approx 1 + \frac{k_u^2 z^2}{2}$

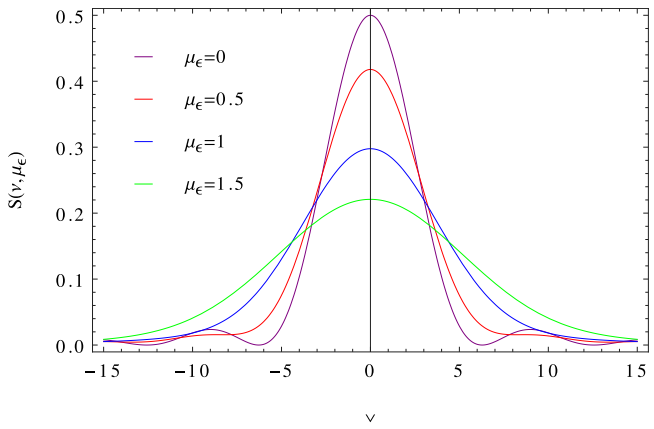

Fig. 4. Spontaneous emission profile vs. the inhomogeneous broadening parameter μ_ϵ.

Deriving Eq. (16) on-axis ($\theta = 0$), one gets:

$$\frac{\Delta\lambda}{\lambda} = \frac{K_u^2}{(1+K_u^2/2)}\frac{dK_u}{K_u}$$

and $\frac{dK_u}{K_u} = \frac{dB_u}{B_u} = \frac{k_u^2 y^2}{2}$ where $k_u = \frac{2\pi}{\lambda_u}$, hence:

$$\left[\frac{\Delta\lambda}{\lambda}\right]_{\sigma_y} = \frac{2\pi^2 K_u^2 \sigma_y^2}{\lambda_u^2(1+K_u^2/2)} \tag{27}$$

A vertical beam size of 0.2 mm RMS contribution on the bandwidth is ∼1.8% FWHM for a $K_u = 2$ and $\lambda_u = 18$ mm.

The homogeneous broadening (or natural linewidth) is associated with the difference of time flight between electrons and photons inside the undulator. Introducing the so-called inhomogeneous broadening induced by non-ideal beam qualities denoted by $\left[\frac{\Delta\omega}{\omega}\right]_i$, the ratio μ_i, called inhomogeneous broadening parameter, can be expressed as:

$$\mu_i = \left[\frac{\Delta\omega}{\omega}\right]_n^{-1}\left[\frac{\Delta\omega}{\omega}\right]_i \tag{28}$$

This quantity measures the effect of beam qualities on the spontaneous emission line, and as discussed later on the FEL performance. The line-width including these terms is thus expressed as:

$$\left[\frac{\Delta\omega}{\omega}\right] = \sqrt{1+\mu_\epsilon^2+\mu_y^2+\mu_{y'}^2}\left[\frac{\Delta\omega}{\omega}\right]_n \tag{29}$$

where μ_ϵ is the broadening ratio of the energy spread, μ_y and $\mu_{y'}$ are the broadening ratio of the beam size and divergence, respectively. The detrimental effect is twofold, determining the broadening and also the peak reduction. The understanding between homogeneous and inhomogeneous line broadening interplay can be followed using the procedure outlined in [213,214]. The integral representation of the homogeneous spontaneous emission line, described in Eq. (19), is:

$$S(\nu) = Re\int_0^1 (1-t)e^{-i\nu t}dt \tag{30}$$

which allows for a straightforward convolution with a Gaussian distribution, for example.

In the case of energy spread, one obtains:

$$S(\nu,\mu_\epsilon) = Re\int_0^1 (1-t)e^{-i\nu t-\frac{1}{2}(\pi\mu_\epsilon t)^2}dt \tag{31}$$

with $\mu_\epsilon = 4\sigma_\epsilon N_u$. Eq. (31) is displayed in Fig. 4 for different values of the energy spread inhomogeneous parameter. When μ_ϵ increases, the spontaneous emission profile $S(\nu,\mu_\epsilon)$) broadens and the peak decreases. It is evident that the condition $\mu_\epsilon < 1$ ($\sigma_\epsilon < \frac{1}{4N_u}$) ensures that these effects are not significant.

The usefulness of the inhomogeneous parameters stems from the fact that they are global. In other words they combine beam and undulator parameters and yield a quick idea of how they influence the spontaneous emission spectrum. Analogous quantities hold for the broadening induced by the emittance.

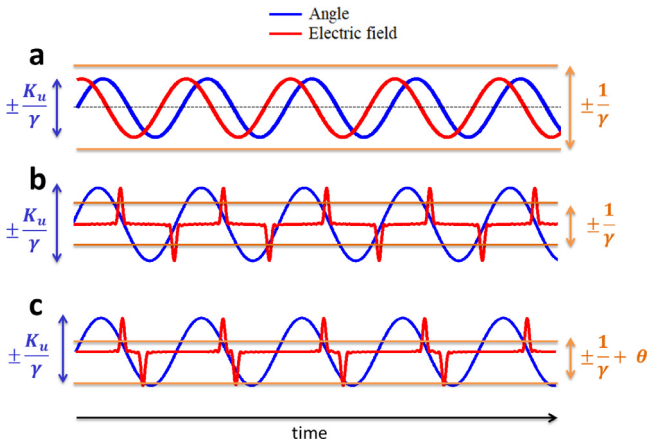

Fig. 5. Schematic view of the electron angle (blue) and the electric field produced (red) reaching the observer bounded by the (orange) lines. (a) $K_u < 1$, (b) $K_u > 1$, (c) observation off-axis.

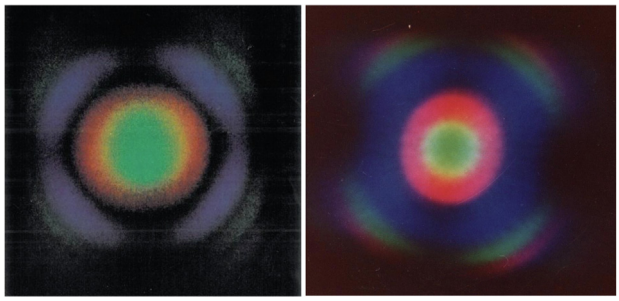

Fig. 6. ACO optical klystron spontaneous emission for different undulator gaps for a 536 MeV electron beam.

3.2. Harmonics

The radiation emitted by an individual electron adds up constructively from one period to another at the resonant frequency and its harmonics. In the on-axis direction where $\theta = 0$, only odd harmonics are observed. For $|\theta| > 0$, even harmonics are present but with a low intensity compared to the odd ones. A closer insight of the harmonics behavior, considering the angle of the electron and the electric field generated for three cases is illustrated in Fig. 5.

- For $K_u < 1$: the electrons maximum excursion angle is within the emitted synchrotron radiation cone $\sim 1/\gamma$, so all of the emitted radiation is seen by the observer and is thus a continuous sinusoidal electric field (see Fig. 5a). Using Fourier transformation, the electric field in the time domain is converted into the frequency domain and then the pure sinusoidal field is simply a single, odd, $(n = 1)$ harmonic.
- For $K_u > 1$, the angular excursion is larger than the cone angle and the observer only sees the electric field briefly as the electron wiggles through this radiation emission angle. The electric field peaks are equally spaced in time but of alternating polarity (see Fig. 5-b) thus the spectrum only contains odd harmonics.
- In the case where the observer is viewing the radiation from off-axis, he still sees only the electric field when the electron is within the cone angle of his observation angle, however since he is no longer on-axis, the electric field alternating pulses are not equally spaced in time with an asymmetry in the amplitude (see Fig. 5c). Hence even harmonics start to be visible on the spectrum.

Fig. 6 shows the angular flux distribution of undulator radiation in the visible light measured at ACO optical klystron [24]. The off-axis radiation is red shifted due to the term $\gamma^2\theta^2$ in (16).

Fig. 7 presents the computed undulator radiation, using the SRW code [203], of the 1st, 5th and 11th harmonics for a single electron (a, b, c) and a multi-electron beam (d, e, f). The formalism of inhomogeneous parameters holds for higher order harmonics too. The beam quality effect is more significant and its impact is proportional to the order of the harmonic. The relative bandwidth is increased by a factor of 1.3, 6.3 and 14 from the single electron emission to the multi-electron one at the harmonics 1, 5 and 11, respectively.

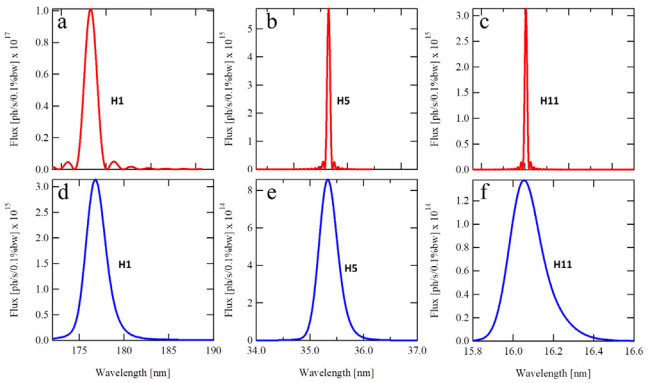

Fig. 7. Undulator radiation computation using a single electron (red) and a multi-electron beam (blue) at the first (a, d), fifth (b, e) and eleventh (c, f) harmonic. Observation window placed at 50 m from the undulator center with 1 mm × 1 mm dimensions. Electron beam parameters: I = 500 A, E = 200 MeV, σ_{ε} = 0.2% RMS, $\sigma'_{x,y}$ = 0.2 mrad, $\sigma_{x,y}$ = 0.2 mrad. Undulator parameters: N_u = 100, B_u = 1.2 T, λ_u = 18 mm, K_u = 2.

3.3. FEL configurations

FEL Oscillators, operating typically in the IR down to VUV, offer significant advantages with respect to their atomic counterparts in terms of laser pulse characteristics and power. They present a very high degree of coherence, both in transverse, due to the optical resonator, and in the longitudinal, close to the Fourier limit, due to the multi-passes. This configuration was used for the first FELs: 3.4 μm in 1977 at Stanford [215], visible in 1983 on the ACO storage ring [216], and 9 − 11 μm at Los Alamos with nine orders of magnitude of power growth [217]. The efficiency and output power were further improved with a tapered undulator [218–220] where the peak field is varied along the electron propagation direction to compensate for the electron beam energy loss. The UV and VUV range was reached on various electron storage ring-based FEL oscillators [35,221–233]. The wavelength limit is set by the gain value compared to the mirror losses [234,235] submitted to damaging irradiation [236]. Coherent harmonic generation was also achieved in the UV and VUV using a Nd–Yag laser since the early FEL times [237–243].

The first demonstration of SASE FEL lasing was first achieved at long wavelength during the mid eighties [244–246], then in the infra-red [247–255]. Thanks to the progress in photoinjector and linear accelerator performance, the beginning of the twenty-first century saw the advent of the saturated SASE in the visible and UV (530 and 385 nm) in 2000 at Argonne National Laboratory (USA) [256,257] on the Low-Energy Undulator Test Line (LEUTL) and in the VUV on Tesla Test Facility (Germany) presently called FLASH [258,259]. The GW level (close to 1 μJ energy) was reached in the 95 − 105 nm spectral range [260]. These results compared favorably with the shortest wavelength achieved using FEL oscillators, marking a turning point in the choice of the type of FEL accelerator driver and undulator configuration. The next decade saw the advent of FELs in the X-ray domain on SCSS Test Accelerator (Japan) (60 − 40 nm) [261,262], FLASH (4.1 nm) [263], LCLS (Stanford, USA) at 0.15 nm [264], SACLA (Japan) in 2011 down to 0.08 nm [265], PAL FEL (Korea) [266], SwissFEL (Switzerland) [267] and European XFEL (Germany) [268], with new projects being under development. SASE-based FELs (usually referred to as fourth generation synchrotron radiation sources) can cover the range from extreme ultraviolet up to hard X-rays, a spectral region where no mirrors are available to confine the optical field inside a resonator. They are regarded as a state of the art tool for probing matter under a variety of conditions with atomic resolution and ultrashort timescales [269].

SASE, resulting from radiation with uncorrelated electron bunchlets, typically presents spiky temporal distributions and thus limited longitudinal coherence. Apart from single spike operation in the low charge and short bunch regime [270–272] or chirped electron bunch associated with an undulator taper [273], the longitudinal coherence of a single pass FEL can be significantly improved by seeding with an external laser spectrally tuned at the undulator fundamental radiation, where intensity fluctuations are reduced and saturation is reached earlier. Non-linear harmonics can also be efficiently generated [274–276] in different configurations such as the High Gain Harmonic Generation layout [277–280]. High order harmonics generated in a gas can also be used as a seed [281–284]. Such a scheme can be put into a cascade for further wavelength reduction.

Seeded single pass FEL facilities are under operation for users : FERMI@ELETTRA in the 100–4 nm region [285–287] and Dalian FEL (Dalian, China) over 50–150 nm [288]. Seeding with the FEL itself [289,290] is of particular interest for the X-ray domain for improving the spectral purity [291–293]. Two successive electron–seed interactions in the Echo Enabled Harmonic Generation [294] (EEHG) scheme enables efficient up-frequency conversion [295–300].

3.4. High gain FEL scaling formulae

The FEL theory, started to be formulated during the second half of the 1970's. It was initially developed for low gain devices, operating in the oscillator configuration. Different formalisms were employed, such as the Boltzmann–Vlasov equation [301], single particle pictures employing the pendulum equation [302] and the Hamiltonian picture [303]. Starting from the early eighties a different point of view had been elaborated. The solution of the coupled Lorentz–Maxwell equations opened the possibility of understanding the so-called high gain regime [20,28,29,304–310], which paved the way for FEL operation without optical cavities and later to the realization of the fourth generation of synchrotron radiation.

The physical mechanism underlying the behavior of a high gain FEL is based on the delivery and amplification of radiation from an electron beam moving in an undulator magnet. The properties of the radiation reflect those characterizing the beam qualities, the accelerating and transport systems, and the undulator field distribution. An appropriate description of the entire system can be obtained by embedding these parameters to select a set of relevant quantities representative of the laser performance. This is achieved by inclusion of them in simple formulae (validated through analytical and numerical methods) which are able to provide a quick estimate of the dynamics and of pivotal quantities like the saturation intensity, growth rate and of the relevant interplay with the contributions due to inhomogeneous broadening, diffraction and so on.

The use of scaling relations for FEL devices has quite a long story. They were initially established [311] for the case of the oscillator, extended to the high gain regime [312,313] without the inclusion of diffraction effects, the crucial step in this direction was accomplished in [314]. The model was then completed in [315] adding the logistic saturation equation, non-linear harmonic generation, pulse propagation contributions [316] and included in the PARSIFEL code [317], providing a quick design of an FEL device be it an oscillator or a SASE device. The usefulness of the scaling formulae stems from the possibility of evaluating the FEL performance with a minimum computational effort.

3.4.1. High gain FEL growth

For a single electron of given energy E, the resonance condition for the wavelength of the emitted on-axis radiation, in a planar undulator, is

$$\lambda_r = \frac{\lambda_u}{2\gamma^2}\left(1+\frac{K_u^2}{2}\right) \tag{32}$$

Limiting oneself to the 1D FEL dynamics, it is well known that the so called pendulum equation is capable of modeling the FEL dynamics from small signal to saturation. The small signal regime encompasses the first part of the FEL evolution, including the exponential growth, is well described by the FEL integral equation obtained from the linearization of the pendulum equation [318]. The FEL dynamics, from small signal to non linear regime, is describe by the Colson pendulum equations [319]:

$$\begin{aligned} &\frac{d^2}{d\tilde{z}^2}\zeta = \mid a \mid \cos(\zeta+\phi), \qquad \mid a \mid = \left(\frac{1}{\gamma}\right)^2 \frac{K_u}{\sqrt{2}}\frac{L_g}{\sqrt{3}\rho} f_b e_s \\ &\frac{da}{d\tilde{z}} = -\frac{2}{\sqrt{3}}\langle e^{-i\zeta}\rangle, \qquad a = \mid a \mid e^{i\phi}, \qquad e_s = \frac{eE_s}{m_e c^2} \end{aligned} \tag{33}$$

where $\langle\rangle$ denotes the average on the initial electron-phase coordinate distribution, $\zeta = (k_u + k_s)z(t) - \omega t$ is the electron-phase coordinate, a the dimensionless field Colson's amplitude, E_s the wave electric field, ϕ the field phase and:

$$\frac{d}{d\tilde{z}}a(\tilde{z}) = \frac{i}{3\sqrt{3}}\int_0^{\tilde{z}} \tilde{z}' e^{-i\tilde{v}\tilde{z}'} a(\tilde{z}-\tilde{z}')d\tilde{z}' \tag{34}$$

where $\tilde{z} = \frac{z}{L_g}$,

$$L_g = \frac{\lambda_u}{4\pi\sqrt{3}\rho} \tag{35}$$

is the gain length and $\tilde{v} = \frac{1}{2\sqrt{3}\rho}\frac{\omega_r-\omega}{\omega_r}$ the detuning parameter.

The associated physical meaning is transparent: the electrons are captured in a pendulum-like bucket whose height increases with the increasing of the field amplitude, in turn determined by the electron-field interaction. The relevant dynamics is better understood in the phase space plot displayed in Fig. 8.

The pivotal quantity of the discussion is ρ, a quantity often referred to as the Pierce parameter given by:

$$\rho = \frac{1}{\gamma}\left[2\pi\frac{J}{I_A}(\lambda_u K_u f_b(\xi))\right]^{1/3} \tag{36}$$

where $f_b(\xi)$ is the gain Bessel factor correction (valid for linearly polarized undulators) and defined as $f_b(\xi) = J_0(\xi) - J_1(\xi)$, $\xi = \frac{K_u^2}{4}\left(1+\frac{K_u^2}{2}\right)^{-1}$ and J is the electron beam current density. The Pierce parameter regulates the power growth along z

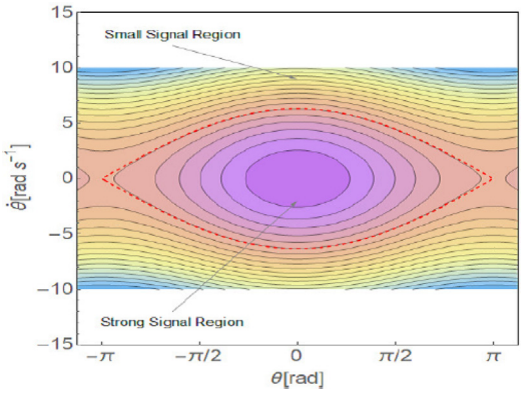

Fig. 8. Phase and associated dynamical regions. Dashed line defines the separatrix between small and strong signal regions. *Source:* E. Di Palma courtesy.

and is linked to the small signal gain coefficient g_0 by

$$\rho = \frac{(\pi g_0)^{\frac{1}{3}}}{(4\pi N_u)}. \tag{37}$$

Replacing the explicit value of the Alfven current $I_A = 1.7.10^4$A, one gets the Pierce parameter in the practical form as:

$$\rho = \frac{8.36.10^{-3}}{\gamma}\left[J[A/m^2](\lambda_u[m]K_u f_b(\xi))^2\right]^{(1/3)} \tag{38}$$

The current density is finally expressed as the RMS bunch peak current divided by transverse beam cross section. The peak current is in turn expressed in practical units as:

$$I[A] = \frac{Q_b[C]}{\sigma_\tau[s]\sqrt{2\pi}} \tag{39}$$

where Q_b is the bunch charge and σ_τ is the RMS bunch duration. Finally J is given by:

$$J\left[\frac{A}{m^2}\right] = \frac{Q_b[C]}{\sigma_\tau[s]\sigma_x[m]\sigma_y[m](2\pi)^{3/2}} \tag{40}$$

where $\sigma_{(x,y)}$ are the RMS transverse beam dimensions.

From the mathematical point of view, Eq. (34) is a Volterra integro-differential equation, with a memory kernel, which takes into account the wave–electron beam interaction at any previous position inside the undulator. The low gain condition $a(\tilde{z} - \tilde{z'}) \simeq a(\tilde{z})$ allows for a direct integration of Eq. (34), which under this assumption reads:

$$\begin{cases} \partial_{\tilde{z}} a(\tilde{z}) = g_1(\tilde{z}) a(\tilde{z}) \\ g_1(\tilde{z}) = i\pi g_0 \int_0^{\tilde{z}} d\tilde{z'} \int_0^{\tilde{z'}} e^{-i\tilde{\phi} z''} dz'' \end{cases} \tag{41}$$

with $g_1(\tilde{z})$ being the complex gain function in the low gain regime.

Equations of the type (34), even though called the FEL integral equation, are paradigmatic for the unsaturated behavior of all the free electron radiation devices (gyrotrons,…) as mentioned in the introductory section. The solution of Eq. (34) can be obtained using different techniques. A perturbative technique is useful if one is interested in understanding the deviation from the small gain regime. Regarding the maximum gain, the higher corrections yield:

$$G(z) = \frac{I(\tilde{z}) - I(0)}{I(0)} \simeq \frac{1}{\pi}\left(\frac{\tilde{z}}{\sqrt{3}}\right)^3 \left[0.85 + \frac{0.19}{\pi}\left(\frac{\tilde{z}}{\sqrt{3}}\right)^3 + \right.$$
$$\left. + \frac{4.23.10^{-3}}{\pi^2}\left(\frac{\tilde{z}}{\sqrt{3}}\right)^6\right] \tag{42}$$

where $I(\tilde{z}) =$ field - Intensity.

The FEL small signal gain coefficient can be expressed in terms of the Pierce parameter as $\rho = \frac{(\pi g_0)^{1/3}}{4\pi N_u}$ with $N_u = \frac{z}{\lambda_u}$, and thus:

$$g_0 = \frac{1}{\pi}\left(\frac{\tilde{z}}{\sqrt{3}}\right)^3 \tag{43}$$

In addition, one can derive from Eq. (42) the maximum small signal gain as a sum of successive powers of g_0 [320]. A general solution technique is that of transforming Eq. (34) into an ordinary differential equation of third order commonly known as the cubic equation. The procedure, reported in [214], consists in noting that, after the change of variable $\tau - \tau' = \sigma$, Eq. (34) can be written as:

$$e^{i\tilde{\nu}\tilde{z}}\frac{d}{d\tilde{z}}a(\tilde{z}) = \frac{i}{3\sqrt{3}}\int_0^{\tilde{z}}(\tilde{z}-\sigma)e^{i\tilde{\nu}\sigma}a(\sigma)d\sigma. \tag{44}$$

Using the following:

$$\int_0^{\tilde{z}}(\tilde{z}-\sigma)e^{i\tilde{\nu}\sigma}a(\sigma)d\sigma = \int_0^{\tilde{z}}d\tilde{z}'\int_0^{\tilde{z}'}e^{i\nu\tilde{z}''}a(\tilde{z}'')d\tilde{z}''$$

and keeping two successive derivatives of both sides of Eq. (44), one finds:

$$\left(\partial_{\tilde{z}}^3 + 2i\tilde{\nu}\partial_{\tilde{z}}^2 - \tilde{\nu}^2\partial_{\tilde{z}}\right)a(\tilde{z}) = \frac{i}{3\sqrt{3}}a(\tilde{z}) \tag{45}$$

whose initial conditions should be carefully chosen. If the signal grows from an initial seed, they write:

$$a|_{\tilde{z}=0} = 0, \quad \partial_{\tilde{z}}a|_{\tilde{z}=0} = 0, \quad \partial_{\tilde{z}}^2 a|_{\tilde{z}=0} = 0 \tag{46}$$

If the field grows from a bunched beam one gets:

$$a|_{\tilde{z}=0} = 0, \quad \partial_{\tilde{z}}a|_{\tilde{z}=0} = b, \quad \partial_{\tilde{z}}^2 a|_{\tilde{z}=0} = 0 \tag{47}$$

where b is the first order bunching coefficient. Assuming the set of initial conditions of Eq. (46), the field growth is specified by the Fang–Torre formula [319].

$$\begin{aligned} a(\tilde{z}) = {} & \frac{a_0}{3\left(\frac{\tilde{\nu}}{\sqrt{3}}+p+q\right)}e^{-\frac{2}{3}i\tilde{\nu}\tilde{z}}\left\{\left(-\frac{\tilde{\nu}}{\sqrt{3}}+p+q\right)\right. \\ & \cdot e^{-\frac{i}{\sqrt{3}}(p+q)\tilde{z}} + 2\left(2\frac{\tilde{\nu}}{\sqrt{3}}+p+q\right)\cdot e^{\frac{i}{2\sqrt{3}}(p+q)\tilde{z}} \\ & \left.\cdot\left[\cosh\left(\frac{1}{2}(p-q)\,\tilde{z}\right) + i\frac{\tilde{\nu}}{(p-q)}\sinh\left(\frac{1}{2}(p-q)\,\tilde{z}\right)\right]\right\} \end{aligned} \tag{48}$$

with

$$\begin{cases} p = \left[\frac{1}{2}\left(r+\sqrt{d}\right)\right]^{\frac{1}{3}} \quad , \quad q = \left[\frac{1}{2}\left(r-\sqrt{d}\right)\right]^{\frac{1}{3}} \\ r = \left[1-\frac{2}{3\sqrt{3}}\tilde{\nu}^3\right] \quad , \quad d = \left[1-\frac{4}{3\sqrt{3}}\tilde{\nu}^3\right] \end{cases} \tag{49}$$

The previous equation is useful to understand the transition from low to high gain regime. Being the laser intensity linked to the square modulus of the dimensionless amplitude $a(z)$, one can define the function

$$G(\tilde{z},\tilde{\nu}) = \frac{\left|a(\tilde{z})\right|^2 - |a(0)|^2}{|a(0)|^2} = \frac{\Delta\lambda}{\lambda} \approx \rho \tag{50}$$

yielding the gain "measured" at different positions inside the undulator as reported in Fig. 9. The gain function in Fig. 9a is the typical asymmetric curve, characterizing the low gain regime. The gain asymmetry is lost while the field growth progresses along the undulator as shown in Fig. 9b,c. For normalization reasons the detuning in the figure is

$$\nu = 4\pi\sqrt{3}\,N_u\rho\tilde{\nu}. \tag{51}$$

It is clear that with increasing gain, the peak of the function (50) is shifted towards zero detuning ($\tilde{\nu} = 0$). Thus if one is interested in the "very" high regime, a reduced form of Eq. (45) enables the evaluation of the square modulus of the field (hence the associated power density) in a fairly straightforward way, namely

$$\begin{aligned} P(z) = {} & \frac{P_0}{9}\left[3 + 2\cosh\left(\frac{z}{L_g}\right) + 4\cos\left(\frac{\sqrt{3}}{2}\frac{z}{L_g}\right)\cdot\right. \\ & \left.\cosh\left(\frac{z}{2L_g}\right)\right] \end{aligned} \tag{52}$$

with P_0 being the power associated with the input seed.

The relevant value can be specified in terms of initial field noise, as specified below. The small signal growth is characterized, by two phases:

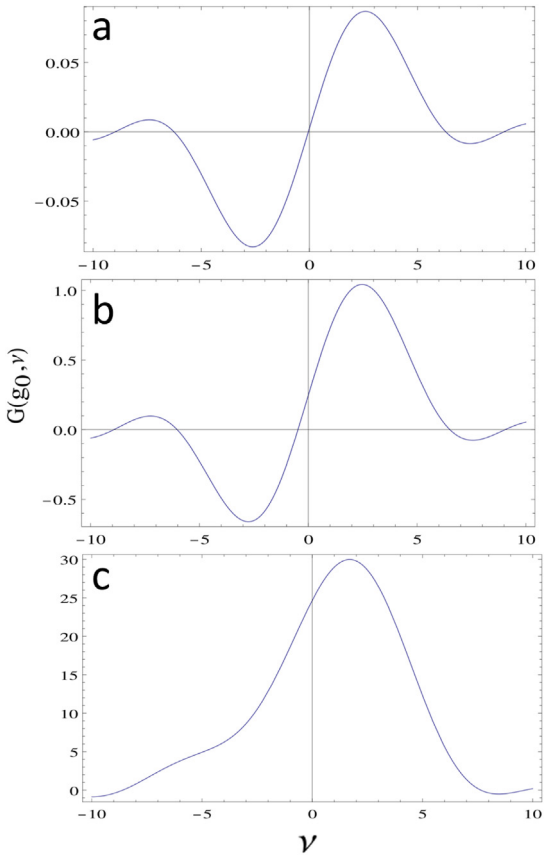

Fig. 9. Gain "measured" at different position inside the undulator in the case of an FEL operating with $\rho = 10^{-3}$. (a) $N_u = 54$, (b) $N_u = 116$, (c) $N_u = 251$. The colored snap shots, yield an idea of how the interplay between FEL intensity growth and electrons phase space distribution.

1. The lethargy region, where the field intensity grows quadratically.
2. The exponential region in which the power vs. z goes like

$$P(z) = \frac{P_0}{9} e^{\frac{z}{L_g}}. \tag{53}$$

This last identity clarifies the role of L_g, which is associated with intensity growth rate and is usually recognized as the gain length. The characteristic length of lethargy region, in which the field organizes its coherence, is almost one gain length. In Fig. 22, a complete view to the intensity growth is presented, where the lethargy, exponential and saturation regions are specified. The dotted curve yields the comparison with the purely exponential (see Eq. (53)) and the complete solution (Eq. (52)) which includes the lethargy region. The figure reports the energy spread induced by the FEL interaction on the electron beam, which will be touched on in the next subsection.

Fig. 10 should be complemented with the change of the bunching factor, which determines the FEL emission process itself and drives its evolution, presented in Fig. 11, where the power and the bunching coefficient of the first harmonic are reported. The example, reported in Fig. 11, refers to an FEL seeded operation, therefore the bunching at the beginning of the interaction still did not occur. The already mentioned lethargy region, represents the interaction length necessary to induce a bunching capable of triggering the exponential regime.

The full solution of Eq. (48) with the inclusion of the detuning parameter allows for the derivation of the gain line shape, which for large gain values can be approximated with a Gaussian (namely for small signal gain coefficients g_0, calculated through Eq. (43), larger than 10)

$$G(\tilde{\nu}) \propto e^{-\frac{\left[\tilde{\nu}-\frac{1}{(2\pi)}\right]^2}{2\left(\frac{2}{\pi^2}\right)^2}}. \tag{54}$$

Accordingly one finds for its RMS relative width

$$\delta\tilde{\nu} = \frac{2}{\pi^2} \rightarrow \frac{\delta\omega}{\omega} \simeq \frac{4\sqrt{3}}{\pi^2}\rho. \tag{55}$$

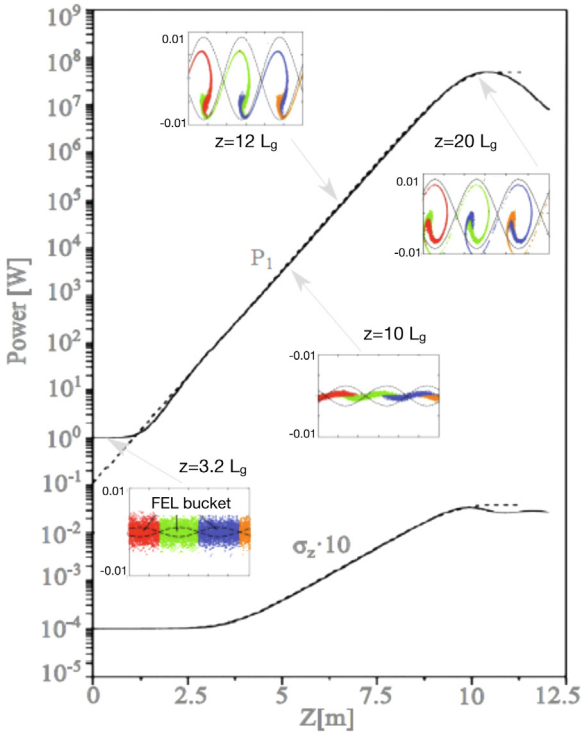

Fig. 10. Power growth evolution and induced energy spread. Upper curves: 1D Prometeo simulation (solid line) compared with the analytical solution of Eq. (53) (dashed line). Lower curves: induced energy spread multiplied by 10 (solid line) compared with the analytical formula (dashed line). Inserts : phase space. Parameters of simulation: $\rho = 2.64 \times 10^{-3}$, $K_u = 2.133$, $\lambda_u = 0.028$ m, $L_g = 0.5$ m.
Source: E. Di Palma courtesy.

The inclusion of the saturation phase in the evolution model is easily achieved with the assumption that the power growth satisfies a Ginzburg–Landau type equation, namely

$$\frac{dP}{dz} = \frac{A'}{A}\left(1 - \frac{P}{P_s}\right)P, \qquad P_s = \sqrt{2}\,\rho\,P_E \tag{56}$$

which assumes that the saturated power P_s is a fraction of the electron beam power $P_E = \gamma\, m_e c^2 \hat{I}$. The efficiency of the SASE FEL is therefore fixed by the Pierce parameter, as a consequence of Eq. (55).
Furthermore:

$$A(z) = \frac{1}{9}\left[3 + 2\cosh\left(\frac{z}{L_g}\right) + 4\cos\left(\frac{\sqrt{3}}{2}\frac{z}{L_g}\right)\cdot \cosh\left(\frac{z}{2L_g}\right)\right] \tag{57}$$

The solution of Eq. (56) writes

$$P(z) = P_0\frac{A(z)}{1 + \frac{P_0}{P_s}\left[A(z) - 1\right]}. \tag{58}$$

Its correctness has been accurately checked in the past and the agreement with numerical and experimental results has always been shown to be good. In Figs. 10–11 the curve Eq. (57) is used to reproduce the whole curve, from lethargy to saturation.

The saturation length, namely the length of the undulator necessary to reach the saturation is obtained by solving the equation

$$P_0\frac{A(L_s)}{1 + \frac{P_0}{P_s}\left[A(L_s) - 1\right]} = \sqrt{2}\rho P_E \tag{59}$$

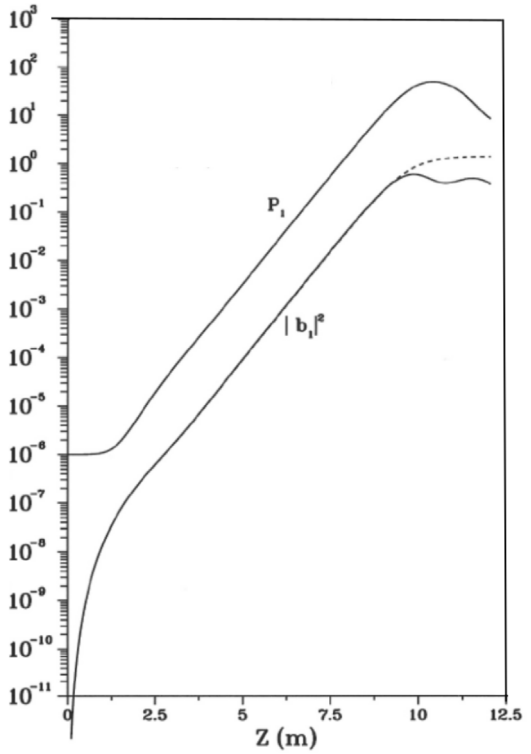

Fig. 11. Power and square modulus of the bunching coefficient vs. the longitudinal coordinate z. Parameters of Prometeo simulation: $\rho = 2.64 \times 10^{-3}$, $K_u = 2.133$, $\lambda_u = 0.028$ m for a planar undulator.

which yields

$$L_s \simeq 1.066\, L_g \ln\left(\frac{9\, P_s}{P_0}\right). \tag{60}$$

or in more practical terms

$$L_s \simeq 20\, L_g. \tag{61}$$

the growth of the power due to the fast growing root only is $P = \frac{P_0}{9} e^{4\pi\sqrt{3}\frac{z}{\lambda_u}}$, the number of undulator periods to reach saturation is $N_s \simeq \frac{1}{\rho}$, therefore $P \simeq 3.15 \cdot 10^8 P_0$. On the other side a quicker evaluation follows from the fact that $L_s = N_s \lambda_u = \frac{\lambda_u}{\rho} \simeq 4\pi\sqrt{3} L_g$.

For the laser signal growing from noise, the following equivalent seed power can be used:

$$P_n = c\rho^2 \frac{E}{\lambda} \tag{62}$$

where E is the electron beam energy. The saturation length is one of the pivotal design elements of FEL devices. Any effect which contributes to an increase of this value must be carefully evaluated.

3.5. High gain regime: Diffraction and beam quality effects

The performance of SASE FELs is limited by all those contributions which may dilute the bunching. Among these are the inhomogeneous broadening and the effect of the diffraction. Two major models have been developed, to include these effects within an analytical (or semi-analytical) context [313–315].

In the previous section it has been shown that the saturation length is approximately 20 gain lengths, the combined effects of energy spread, emittances and diffraction are all contributions diluting the gain, hence increasing the gain length and saturation length. The problem of including the beam quality effect within the framework of a 1D model is easily done by modifying the FEL integral equation as it follows in the simple case of a round beam with identical transverse

emittance

$$\frac{da}{d\tilde{z}} = \frac{i}{3\sqrt{3}}\int_0^{\tilde{z}} \tilde{z}' \frac{e^{-i\tilde{\nu}\tilde{z}' - \frac{1}{2}\left(\frac{\tilde{\mu}_\varepsilon \tilde{z}}{2\sqrt{3}}\right)^2}}{(1-i\tilde{\mu}_\sigma \tilde{z}')(1-i\tilde{\mu}_{\sigma'}\tilde{z}')} a(\tilde{z}-\tilde{z}')d\tilde{z}',$$
$$\tilde{\mu}_\varepsilon = \frac{2\sigma_\varepsilon}{\rho}, \qquad \tilde{\mu}_{\sigma'} = \frac{d}{2\pi\sqrt{3}\rho}\frac{\lambda_u}{\beta_T}, \tag{63}$$
$$\tilde{\mu}_\sigma = \frac{4\pi^2}{\sqrt{3}\rho(1+\alpha_T^2)}\left(\frac{\sigma}{\lambda_u}\right)^2, \qquad d \equiv \frac{4\pi\varepsilon}{\lambda},$$

with ε the electron beam emittance, σ_ε the electron beam relative energy spread, $\sigma = \sqrt{\beta_T \varepsilon}$ the electron beam transverse section, β_T, γ_T, α_T, the electron beam Twiss parameters. The coefficients $\tilde{\mu}_{\sigma'}$, $\tilde{\mu}_\sigma$ account respectively for the angular and transverse part of the electron beam transverse distribution. The 3D effects associated with the wave diffraction are included by writing the small signal FEL equation in more general terms, which results in an extension of the paraxial equation as indicated below

$$-\frac{i}{2}\nabla_T^2 a + \frac{da}{d\tilde{z}} = \\ = \frac{i}{3\sqrt{3}} f \int_0^{\tilde{z}} \tau' \frac{e^{-i\tilde{\nu}\tilde{z}' - \frac{1}{2}\left(\frac{\tilde{\mu}_\varepsilon \tilde{z}}{2\sqrt{3}}\right)^2}}{(1-i\tilde{\mu}_\sigma \tilde{z}')(1-i\tilde{\mu}_{\sigma'}\tilde{z}')} a(\tilde{z}-\tilde{z}')d\tilde{z}', \tag{64}$$

where f accounts for the transverse longitudinal distribution of the beam current and ∇_T^2 is the transverse Laplacian, defined as

$$\nabla_T^2 = \partial_\xi^2 + \partial_\eta^2, \quad D = \frac{\lambda L_g}{2\pi\sigma^2}. \tag{65}$$

where $\xi = \frac{x}{\sigma}$ and $\eta = \frac{y}{\sigma}$. An analytical solution of Eq. (63) or Eq. (64) equations are rather difficult and once obtained are written in terms of combinations of special functions [321] and turn out to not be transparent or useful from the physical point of view.

From the above equation, a set of key-parameters which can capture the effect of the gain reduction have emerged. Semi-analytical and/or analytical solutions have then be parameterized in terms of these parameters [314,315].

The starting point of this analysis is the understanding that their macroscopic effect is that of increasing the saturation length, in turn proportional to the gain length, which in the case of an actual device is a function dependent on energy spread and emittance, denoting by $L_g^{(3d)}$ the non-ideal gain length, using notations in [314], one writes:

$$\frac{L_g}{L_g^{(3d)}} = \frac{1}{1+\eta(\eta_d, \eta_\varepsilon, \eta_\gamma)} \tag{66}$$

where

$$\eta_d = \frac{D}{2}, \qquad \eta_\varepsilon = \frac{2}{\sqrt{3}}\tilde{\mu}_{\sigma'}, \qquad \eta_\gamma = \frac{1}{2\sqrt{3}}\tilde{\mu}_\varepsilon. \tag{67}$$

The function η is parameterized as follows:

$$\eta = a_1\eta_d^{a_2} + a_3\eta_\epsilon^{a4} + a_5\eta_\gamma^{a_6} + a_7\eta_\epsilon^{a_8}\eta_\gamma^{a_9} + a_{10}\eta_d^{a_{11}}\eta_\gamma^{a_{12}} \\ + a_{13}\eta_d^{a_{14}}\eta_\epsilon^{a_{15}} + a_{16}\eta_d^{a_{17}}\eta_\epsilon^{a_{18}}\eta_\gamma^{a_{19}} \tag{68}$$

with

$a_1 = 0.45$	$a_2 = 0.57$	$a_3 = 0.55$	$a_4 = 1.6$	$a_5 = 3$
$a_6 = 2$	$a_7 = 0.35$	$a_8 = 2.9$	$a_9 = 2.4$	$a_{10} = 51$
$a_{11} = 0.95$	$a_{12} = 3$	$a_{13} = 5.4$	$a_{14} = 0.7$	$a_{15} = 1.9$
$a_{16} = 1140$	$a_{17} = 2.2$	$a_{18} = 2.9$	$a_{19} = 3.2$	

The saturation power obtained from simulation is given by:

$$P_s = 1.6\rho\left(\frac{L_g}{L_g^{(3d)}}\right)P_E \tag{69}$$

The evaluation of the saturation length follows the same procedure exploited at the end of the previous subsection with the exception that instead of the seed power P_0, the initial noise P_n of Eq. (62) is used.

The procedure envisaged in [315] uses a slightly different approach. It assumes that, even in the presence of gain dilution, the evolution is still ruled by Eq. (58), by modifying the Pierce parameter as:

$$\rho^D = F(\mu^D)\rho, \quad F(\mu^D) = (1+\mu^D)^{-\frac{1}{3}}, \quad \mu_\eta^D = \frac{\sqrt{3}}{2}D. \tag{70}$$

The gain length as (note that the $\tilde{\mu}$ parameters are now defined in terms of the modified Pierce parameter, $\tilde{\mu}_\varepsilon = 2\frac{\sigma_\varepsilon}{\rho^D}$ and similarly for the others):

$$\begin{aligned} &L_{g,1} = \chi L_{g,1}, \qquad \chi = F_3^{-1}, \qquad F_3 = \frac{F_1}{F_2} e^{c\mu_\varepsilon^2}, \\ &F_1 = \frac{1 + 2a\left(\tilde{\mu}_\sigma^2 + \tilde{\mu}_{\sigma'}^2\right) + 2b\left(\tilde{\mu}_\sigma + \tilde{\mu}_{\sigma'}\right)}{\left(1 + \tilde{\mu}_\sigma^2\right)\left(1 + \tilde{\mu}_{\sigma'}^2\right)}, \\ &F_2 = 1 + dF_1\tilde{\mu}_\varepsilon^2, \\ &a = 0.159,\ b = -0.066,\ c = -0.034,\ d = 0.185\frac{\sqrt{3}}{2}. \end{aligned} \tag{71}$$

The saturated power is replaced by:

$$P_s = \frac{\sqrt{2}\rho}{(1 + \mu^D)^{\frac{2}{3}}} P_E. \tag{72}$$

Regarding the saturation length one eventually finds:

$$L_S \simeq 4\pi\sqrt{3}\chi L_g. \tag{73}$$

It is accordingly evident that, comparing (73) with the ones in [314], one infers:

$$\chi = 1 + \eta. \tag{74}$$

The predictions of the two approaches have been benchmarked against numerical codes and experiments.

Regarding the energy spread a condition to be satisfied to avoid gain problems is just given by $\sigma_\epsilon < \rho/2$ which becomes Eq. (75).

The space charge is a further physical mechanism opposing the effect of bunching, therefore contributing to the gain reduction and thus to the increase of the saturation length. The relevant contributions to the FEL dynamics have been considered at the beginning of the FEL theory by Shih and Yariv [322,323] and successively by other authors [324–329]. In more recent studies [330,331] they have been embedded in a more general treatment and the combined contribution with the other limiting factors has been accomplished by the use of an appropriate extension of the η/μ parameters.

Although the effect produced on the FEL gain by the space-charge de-bunching is not, strictly speaking, an inhomogeneous broadening, it has been observed that it produces a gain line broadening and a peak reduction similar to that induced by the energy spread [331]. The parameter useful to quantify the relevant gain deteriorating effect has been shown to be

$$\tilde{\mu}_Q = \frac{1}{\rho}\left(\frac{\Omega_p \lambda_u}{2c}\right), \quad \Omega_p^2 = \frac{e^2 \overline{N}_e}{\varepsilon_0 m_e \gamma^3} \tag{75}$$

where $\overline{N}_e$ is the electron number volumetric density and which can be cast in the more physically transparent form

$$\begin{aligned} &\tilde{\mu}_Q = \frac{1}{\gamma\rho}\left(\alpha\frac{E_f}{E_e}\frac{\lambda}{4\pi\varepsilon}\frac{\dot{N}_e\lambda_u^2}{c\beta_T}\right)^{\frac{1}{2}}, \quad \dot{N}_e = \frac{N_e}{\sqrt{2\pi}\sigma_\tau}, \\ &E_f = \hbar\omega, \qquad E_e = m_e\gamma c^2 \end{aligned} \tag{76}$$

where α is the fine structure constant.

The increase of the gain length can be derived from an appropriate fit of the numerical data. It results in a simple function of $\tilde{\mu}_Q$ according to the following identity:

$$L_G(\tilde{\mu}_Q) = L_g \exp\left(\frac{\tilde{\mu}_Q^2}{18} - 1.15 \cdot 10^{-4}\tilde{\mu}_Q^5\right) \tag{77}$$

It is evident that non-negligible effects occur in an FEL driven by extremely challenging electron beams such as those in [332], where $E_e \simeq 15$ GeV, $E_f \simeq 12.4$ keV, $\lambda_u = 0.04$ m, $\beta_T = 8$ m and $\hat{I} > 5$ kA. The use of the above values, along with the assumption that $\frac{\lambda}{4\pi\varepsilon} \approx 1$, the associate values of $\tilde{\mu}_Q$ are of the order of 3 and the associated effect may produce an increase of the gain length larger than 50% (for further comments see [331]).

The SASE FEL radiation from a planar undulator is linearly polarized in the plane of the electron wiggle motion. The transverse coherence is ensured by the so called phase and gain guiding. The natural diffraction is counter-acted by this effect and there is no gain dilution due to diffraction, provided that $L_g < \beta/2$.

In fact, although many transverse modes are excited at the beginning of the undulator, by the end of the exponential growth only the highest growth rate mode (generally the fundamental mode TEM_{00}) dominates. Regarding the longitudinal

coherence, it should be noted that it is regulated by three pivotal parameters, namely by the coherence length L_c, defined as:

$$L_c = \frac{\lambda}{4\pi\sqrt{3}\rho} \tag{78}$$

The number of associated slices can be expressed in terms of the longitudinal electron bunch length L_b:

$$M = \frac{L_b}{2\pi L_c}$$

Each slice yielding an independent laser spike [310,333]. Finally, the number of photons per pulse can be estimated by:

$$n_{ph} = \frac{P_s}{\hbar\omega}\sigma_{ph} \tag{79}$$

σ_{ph} being the time duration of the photon pulse.

3.6. FEL non-linear harmonics generation

Ultra-relativistic electrons moving in a magnetic undulator emit radiation with a spectrum characterized by a series of narrow peaks around the frequency

$$\omega_r = 2\frac{\gamma^2}{1+\frac{K_u^2}{2}}\omega_u, \qquad \omega_u = ck_u \tag{80}$$

and higher harmonics $\omega_n = n\omega_r$.

It has also been underscored that, in linearly polarized undulators, along with the fundamental harmonic $n = 1$, higher harmonics of odd order are radiated on-axis. An analogous emission pattern can be envisaged for the lasing process, which is ruled by a bunching process, which determines not only the lasing at the fundamental harmonics, but also coherent radiation at the fundamental.

The bunching mechanism underlying the FEL process is a complex interplay between density modulation and deterioration of the beam energy spread, induced by the field–electron interaction.

The FEL induced energy spread is, in some sense, a kind of self regulatory feedback leading the system to saturation. The evolution along the undulator axis of the high gain FEL induced energy spread can be parameterized as:

$$\begin{aligned}
&\sigma_i(z) \simeq 3C\sqrt{\frac{A(z)}{1+9B(A(z)-1)}},\\
&C = \frac{1}{2}\sqrt{\frac{\rho P_0}{P_E}}, \qquad B \simeq \frac{1.24}{9}\frac{P_0}{P_s}, \qquad \sigma_i \simeq \frac{C}{\sqrt{B}} \simeq 1.6\rho.\\
&\xi = \frac{1}{4}\frac{K_u^2}{1+K_u^2/2}
\end{aligned} \tag{81}$$

In correspondence with the end of the exponential growth region, the induced energy spread ($\sigma_{i,F}$) is simply proportional to the Pierce parameter (the extension to 3D effects is simply achieved by replacing ρ with ρ^D as in Eq. (81)).

Along with the effect of beam degradation, another ongoing mechanism is that of the higher order bunching. Although this is a somewhat naïve picture, since the two effects cannot be so easily disentangled, one understands that together with energy distortion the longitudinal electron phase space is modulated with a higher harmonic content, the mechanism which allows for the coherent emission at higher order harmonics.

The pendulum equation including the coupling with higher harmonics in a linearly polarized undulator is reported below [318]:

$$\begin{aligned}
&\frac{d^2}{d\tilde{z}^2}\zeta = \sum_{n=0}^{\infty} \mid a_n \mid \cos(\psi_n), \qquad \psi_n = n\zeta + \phi_n,\\
&\frac{d}{d\tilde{z}}a_n = -\frac{2}{\sqrt{3}}\langle e^{-in\zeta}\rangle, \qquad a_n = \mid a_n \mid e^{i\phi_n},\\
&\mid a_n \mid = \left(\frac{1}{\gamma}\right)^2 \frac{K_u}{\sqrt{2}}\frac{L_g}{\sqrt{3}\rho} f_{b,n} e_{s,n}, \qquad e_{s,n} = \frac{eE_{s,n}}{m_e c^2}
\end{aligned} \tag{82}$$

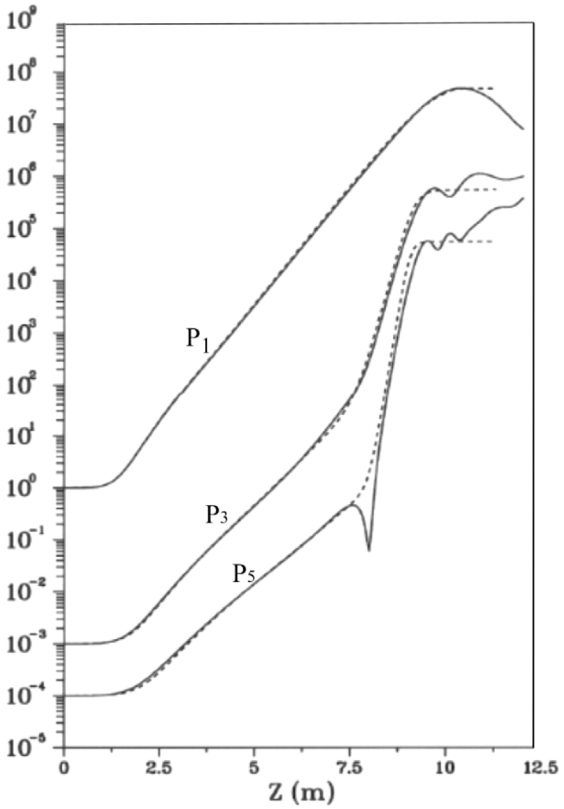

Fig. 12. Laser power P_1 (in Watt) vs. longitudinal coordinate z. Non-linearly coherent generated harmonics (3,5). Continuous line is the Perseo simulation, the dotted line is the semi-analytical formulas (Eqs. (59) and (87)). Parameters of simulation: $\rho = 2.64 \times 10^{-3}$, $K_u = 2.133$, $\lambda_u = 0.028$ m.

where n is the harmonic number, a_n the dimensionless amplitude, ϕ_n the field amplitude phase, $E_{s,n}$ the harmonic electric field and

$$\begin{aligned} \rho_n &= \rho \left(\frac{f_{b,n}}{f_{b,1}}\right)^{\frac{2}{3}}, \\ f_{b,n} &= f_{b,n}(\xi) = (-1)^{\frac{n-1}{2}} \left(J_{\frac{n-1}{2}}(n\xi) - J_{\frac{n+1}{2}}(n\xi)\right) \end{aligned} \tag{83}$$

with $n = 1$ representing the order of the fundamental harmonic and $f_{b,n}(\xi)$ the odd on-axis harmonic Bessel coupling factor. The integration of Eq. (82) yields the evolution of the fundamental harmonic and that of higher order odd harmonics $n = 3, 5$, as shown in Fig. 12.

It should be noted that ([275]:

(a) The linear part of the higher harmonic growth power behaves like that of the fundamental. The small signal regime is indeed ruled by an integral equation almost similar to that of the fundamental and characterized by a gain length

$$L^*_{g,n} = \frac{\lambda_u}{4\pi\sqrt{3}\rho^*_n}, \qquad \rho^*_n = \sqrt[3]{n}\rho_n \tag{84}$$

and by a growth (including lethargy)

$$\Lambda_n(z) = P_{0,n}A_n(z) \tag{85}$$

with $P_{0,n}$ being the power of the fundamental harmonic.

(b) When the power of the first harmonic becomes sufficiently large the nth order bunching coefficient

$$b_n = \langle e^{in\zeta} \rangle. \tag{86}$$

exhibits a non-linear increase which determines a substantive enhancement of the higher harmonic power emission (see Fig. 13) and the non-linear coherent growth at the nth harmonic is triggered.

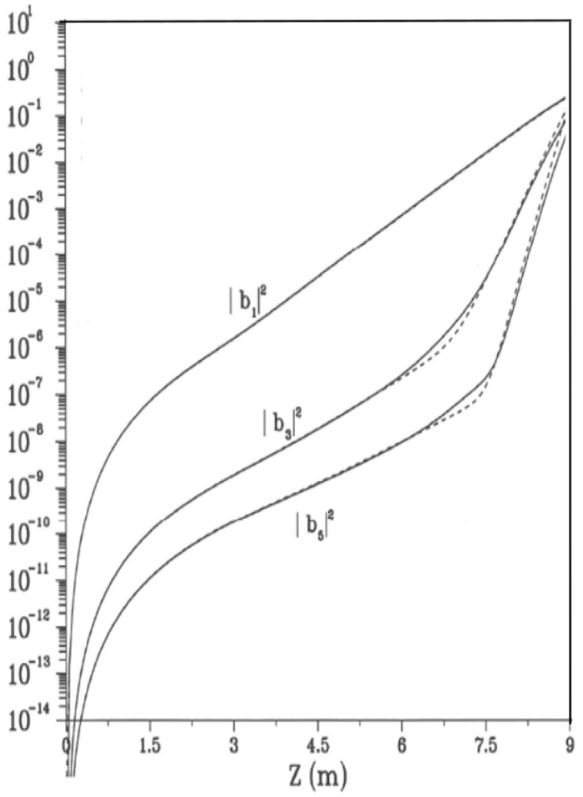

Fig. 13. Square modulus of Bunching coefficients vs. the longitudinal coordinate expressed in meters. Parameters of simulation: $\rho = 2.64 \times 10^{-3}$, $K_u = 2.133$, $\lambda_u = 0.028$ m.

The bunching coefficients depend on the power of the fundamental harmonic, their evaluation in analytical terms is be reported in [275]. Putting everything together, one can write the evolution of the nth harmonic power as:

$$\begin{aligned} &P_n(z) = \Lambda_n(z) + \Pi_n(z), \qquad n = 3, 5, 7, \ldots \\ &\Pi_n(z) = \Pi_{0,n} \frac{e^{\frac{nz}{L_g}}}{1 + \frac{\Pi_{0,n}}{\Pi_{s,n}} \left(e^{\frac{nz}{L_g}} - 1 \right)}, \\ &\Pi_{0,n} = c_n \left(\frac{P_0}{9 \rho P_E} \right)^n \Pi_{s,n}, \qquad c_3 = 8, \quad c_5 = 116, \\ &\Pi_{s,n} = \frac{1}{\sqrt{n}} \left(\frac{f_{b,n}}{n f_{b,1}} \right)^2 P_s \end{aligned} \tag{87}$$

where c_n are coefficients derived from numerical computation and $\Pi_{s,n}$ is the saturated power of the nth harmonic.

The number of photons emitted at the nth harmonics $\lambda_n = \lambda / n$ can be obtained from Eqs. (87)

$$\begin{aligned} &n_{ph,n} \simeq \frac{\Pi_{s,n}}{n \hbar \omega} \sigma_{ph,n} = \chi_n n_{ph} \\ &\chi_n = \frac{1}{n \sqrt{n}} \left(\frac{f_{b,n}}{n f_b} \right)^2 \frac{\sigma_{ph,n}}{\sigma_{ph}} \end{aligned} \tag{88}$$

where $\sigma_{ph,n}$ is the time duration of the harmonic photon pulse. The parameter χ_n represents the harmonic conversion efficiency (which for the third harmonic is around 0.1%). The non-linear higher harmonic generation is a by-product of the FEL mechanism itself. It is a consequence of the higher order bunching occurring when the level of the fundamental harmonics is substantively large. It occurs both in oscillator and SASE devices.

Several physical considerations on Eq. (87) can be given. First, they account for the growth of the FEL power at a given frequency and of the induced higher harmonic power in a linearly polarized undulator. Second, although bunching may occur at even harmonics, power transfer to harmonics is ensured only if an effective coupling does exist which makes

$\rho_{n>1} \neq 0$ (in the case of a helical undulator there is no on-axis coupling to higher harmonics therefore $\rho_{n>1} = 0$). Third, being the bunching generated at even and odd harmonics it is possible to define the so-called undulator segmented operation, consisting of e.g. two undulators, the first with period λ_u and the second with period such that

$$\lambda_u \left(1 + \frac{K_2^2}{2}\right) = \frac{\lambda_u}{n} \left(1 + \frac{K_1^2}{2}\right) \tag{89}$$

where $K_{1,2}$ denotes the strengths of the first and second undulator respectively. In such a device the field grows along the first undulator along with the bunching coefficient, when the beam is extracted from the first and inserted in the second, the acquired bunching coefficient allows the seedless growth at the wavelength λ/n.

4. Electron beam matching to the undulator

4.1. Electron beam brightness

In this subsection, we touch on the electron beam brightness $\mathfrak{B}$, a figure of merit of central importance in the theory of beam transport. From the physical point of view $\mathfrak{B}$ is understood as the charge density with respect to the six-dimensional phase-space and is an invariant under beam transport, if magnet non-linearities and intra-beam collective effects do not cause phase space distortions. The electron beam is the source of the FEL radiation and its brightness is the imprinting of that of the laser. A large beam brightness ensures, in principle, an adequately good FEL performances in terms of photon flux density per unit phase space, provided that no dilution occur during the transport of the e-beam inside the undulator. In SI units (C/m^3J), $\mathfrak{B}$ writes:

$$\mathfrak{B} = \frac{Q}{\varepsilon_{n,x}\varepsilon_{n,y}\varepsilon_{n,z}} \tag{90}$$

where Q is the beam charge, $\varepsilon_{n,\eta}$, $\eta = x, y$ denote the normalized transverse emittances, while $\varepsilon_{n,z}$ is the longitudinal emittance normalized to the beam energy as:

$$\begin{aligned} &\varepsilon_{n,x} = \gamma\varepsilon_x, \quad \varepsilon_{n,y} = \gamma\varepsilon_y \\ &\varepsilon_{n,z} = \gamma\varepsilon_z, \quad \varepsilon_z = m_e c^2 \sigma_\epsilon \sigma_z \end{aligned} \tag{91}$$

with $\sigma_\epsilon (= \Delta_E/(\gamma m_e c^2))$ and Δ_E being the fractional and uniform energy spread, respectively. The absence of the subscript n denotes the phase space area when the beam has been set to the energy $\gamma m_e c^2$. It is assumed here that no collective or non-linear contributions have degraded the beam qualities during the acceleration process. Accordingly, the brightness at the undulator entrance is the same as the output of the accelerating cell.

Using Eqs. (90)–(91) , the brightness can expressed as:

$$\mathfrak{B} = 1.22 \times 10^{13} \frac{Q}{\gamma^3 \varepsilon_x \varepsilon_y \sigma_z \sigma_\epsilon} \tag{92}$$

Recalling the peak current I and density current J expressions,

$$I = \frac{Qc}{\sqrt{2\pi}\sigma_z}, \quad J = \frac{I}{2\pi\sigma_x\sigma_y}, \quad \sigma_T = \sqrt{\beta_T \varepsilon_T} \tag{93}$$

and assuming equal transverse beam size and emittance, $\beta_x = \beta_y = \beta_T$, the beam brightness $\mathfrak{B}$ is:

$$\mathfrak{B} \simeq 6.4 \times 10^5 \frac{\beta_T}{\gamma^3 \varepsilon_T} \frac{J}{\sigma_\epsilon} \tag{94}$$

The FEL Pierce parameter is then expressed in terms of $\mathfrak{B}$ as:

$$\rho \simeq 9.7 \times 10^{-5} \left(\lambda_u[m] K_u f_B(K_u)\right)^{\frac{2}{3}} \left(\sigma_\epsilon \mathfrak{B} \frac{\varepsilon_T}{\beta_T}\right)^{\frac{1}{3}} \tag{95}$$

which simply states that the Pierce parameter increases as $\mathfrak{B}^{1/3}$. If we invert Eq. (95), using the energy spread inhomogeneous parameter ($\tilde{\mu}_\varepsilon = 2\frac{\sigma_\varepsilon}{\rho}$) and the electron-radiation phase space matching condition ($\varepsilon_T \approx \frac{\lambda}{4\pi}$), we can express the brightness as:

$$\mathfrak{B} \simeq 0.5 \times 10^{11} \frac{\beta_T}{\tilde{\mu}_\varepsilon \lambda} \left(L_g K_u f_B\right)^{-2} \tag{96}$$

where, the emittance dependence is replaced by imposing the phase space matching condition. Eq. (96) displays the expected feature that operating at shorter wavelengths requires a beam with increasingly larger brightness.

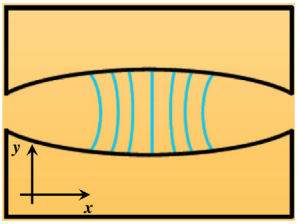

Fig. 14. Undulator with a parabolically-shaped pole face.

Fig. 15. FODO sketch: Focusing and defocusing quadrupoles placed in between the undulator segments.

Finally, solving Eq. (96) for the gain length, one finds:

$$L_g = \frac{R}{\sqrt{\mathfrak{B}}} \quad \text{with} \quad R = \frac{2.24 \times 10^5}{K_u f_b}\sqrt{\frac{\beta_T}{\tilde{\mu}_\varepsilon \lambda}} \tag{97}$$

which states that, for fixed R, L_g goes as the inverse of the square root of the brightness.

As already noted $\mathfrak{B}$ is an invariant in linear transport systems, the relevant control is therefore crucial for the success of the FEL operation itself. The following section is devoted to a general outline of the criteria underlying the design of electron beam transport lines in FEL dedicated undulators.

4.2. Electron beam transport along the FEL

The electron motion in a linearly polarized undulator (along the y direction) consists of two components: the fast part, induced in the z-x plane, by the on-axis field (depending on the longitudinal coordinate only) and the slow part (the y-betatron motion) associated with the off axis part, depending also on the transverse coordinates. The fast motion is characterized by a short wavelength, that is essentially the undulator period, the second by a significantly larger period.

The natural focusing of the undulator is a consequence of the higher order multi-polar magnetic field contributions, causing a restoring force along y which at the lowest order are specified by the harmonic oscillator equation

$$y'' = -\frac{1}{\beta_n^2} y, \quad \beta_n = \frac{\gamma \lambda_u}{\pi K_u} \tag{98}$$

where β_n is the natural Twiss beta value of the undulator. An electron beam having the same Twiss beta at the undulator entrance is automatically matched, at least for the vertical plane. Since a flat field distribution along x is assumed, one expects that along this direction a drift motion occurs, with a consequent defocusing and gain reduction due to the lack of overlap between laser and optical beam.

The problem can be solved by including additional focusing. Examples of tools exploited to constrain both transverse sizes are those reported in Figs. 14–15. In the first, the undulator is made focusing in radial and vertical directions, by suitably shaping the magnets. Regarding the other solution, focusing and defocusing quadrupoles are inserted between the undulator segments. The net effect is that of transporting an approximately round electron-beam, overlapping the laser beam along the whole undulator length. Before going further it is worth stressing that the necessity of overlapping electrons and photon beams, imposes further conditions on the electron transport conditions. We give a preliminary idea of the interplay occurring between laser and electron beam matching using a fairly simple example. We assume that the undulator is focusing in both transverse directions and that the natural undulator focusing is sufficient to confine the beam inside the undulator. If we keep a round diffraction limited beam with emittance defined by Eq. (96)), we obtain, according to the definition of the natural beta focusing given in Eq. (98):

$$\sigma_n \simeq \sqrt{\frac{\lambda}{4\pi}\beta_n} = \frac{1}{2\pi}\sqrt{\frac{\gamma \lambda_u \lambda}{K_u}} \tag{99}$$

In the absence of an optical cavity, the laser waist can be assumed to be provided by the electron transverse size, allowing the Rayleigh length Z_R to be estimated as

$$Z_R \simeq \pi \frac{\sigma_T^2}{\lambda} = \frac{\gamma \lambda_u}{4\pi K_u} \tag{100}$$

For future convenience one writes

$$Z_{R,n} \simeq qL_g, \qquad q = \sqrt{3}\frac{\gamma\rho}{K_u}, \tag{101}$$

The condition in Eq. (99) represents a geometrical overlapping, which does not take into account the effect of radiation focusing, notwithstanding the parameter q displays some features worth commenting upon.

If $q > 1$, the field section is not spreading appreciably along the undulator and the assumption that $q \simeq 1$ is consistent with the characteristics of short wavelength devices, one gets

$$\rho \simeq \frac{K_u}{\sqrt{3}\gamma} \tag{102}$$

which for a beam with an energy of 5 GeV and $K_u \simeq 1$ yields $\rho \simeq 10^{-4}$.

The assumption that the beam section is linked to the undulator matching parameter does not represent an optimal choice. We relax the condition of diffraction limited beam and write:

$$\sigma_T = \sqrt{r_T}\sigma_n, \qquad r_T = \frac{\beta_T}{\beta_n} \tag{103}$$

where the "natural" beam section writes $\sqrt{\beta_n \varepsilon}$ and β_T is the value of the beam Twiss parameter, to be chosen after an appropriate study (minimization of saturation length, maximization of the saturated power…). With this assumption, the current density can be written as $J = \frac{I}{2\pi r \sigma_n^2}$.

In order to maximize the Pierce parameter it is necessary to keep $r < 1$ and therefore $\beta_T < \beta_n$, which means that an additional focusing is necessary to transport the electron beam to guarantee a successful FEL operation.

Regarding the Rayleigh length one finds

$$Z_R \simeq qr_T L_s < Z_{R,n} \tag{104}$$

which demands an additional focusing for the radiation too, to preserve the overlapping with the electron beam along the whole undulator. It is evident that β_T cannot be reduced indefinitely without taking into account the other affects due to diffraction and to inhomogeneous broadening parameters.

The previous considerations suggest that it is necessary to reduce β_n in order to get a smaller transverse beam section and so a larger current density. It is therefore necessary to superimpose an additional focusing ensuring an effective parameter $\beta < \beta_n$.

Fig. 15 shows the typical *FODO* – focusing quadrupole, drift section defocusing quadrupole, drift – and is quite a reasonable solution for strong focusing of the undulator, namely if the betatron period is comparable with the length of the undulator section, consisting of N_u periods: $N_u \simeq \gamma/(\pi K_u)$. The unit cell consists of half a focusing quadrupole, a drift section, a full defocusing quadrupole, a drift section, and half a focusing quadrupole. The cells are understood to be repeated along the whole undulator section. The transport matrix for a single cell is

$$M_{FODO} = \begin{pmatrix} 1 - \frac{L^2}{2f^2} & 2L\left(1 + \frac{L}{2f}\right) \\ -\frac{L}{2f^2}\left(1 - \frac{L}{2f}\right) & 1 - \frac{L^2}{2f^2} \end{pmatrix} \tag{105}$$

The stability of the line is ensured if $f > L/2$ and the resulting identity for the Twiss β parameter:

$$\beta_{FODO} = \frac{1}{2}\frac{4f + L}{\sqrt{1 - \left(\frac{L}{2f}\right)^2}} \tag{106}$$

In case of short wavelength operations, an additional *FODO* structure should be superimposed along the undulator.

Without further entering the details of an actual *FODO* for SASE FEL operations, a criterion for the choice of a more convenient operating β is briefly discussed. The most convenient value of β can be obtained, for example, by minimizing the gain length or by maximizing the output power.

The "optimization" procedure is, in principle, straightforward. One notes that the Pierce parameter can be parameterized in terms of the beta Twiss as:

$$\rho(\beta) = \rho(\beta_n)\left(\frac{\beta_n}{\beta}\right)^{\frac{1}{3}} \tag{107}$$

Inclusion of diffraction corrections modifies ρ as:

$$\rho_D(\beta) = \rho(\beta)[1 + \mu_D(\beta)]^{-\frac{1}{3}}, \ \mu_D(\beta) = \frac{\lambda\lambda_u}{(4\pi\sigma_T)^2\rho} \tag{108}$$

thus finally getting the "global" dependence in terms of beta:

$$\rho_D(\beta) = \frac{\rho(\beta_n)r^{-1/3}}{\left[1 + \mu_D(\beta_n)r^{\frac{1}{3}}\right]^{\frac{1}{3}}} \tag{109}$$

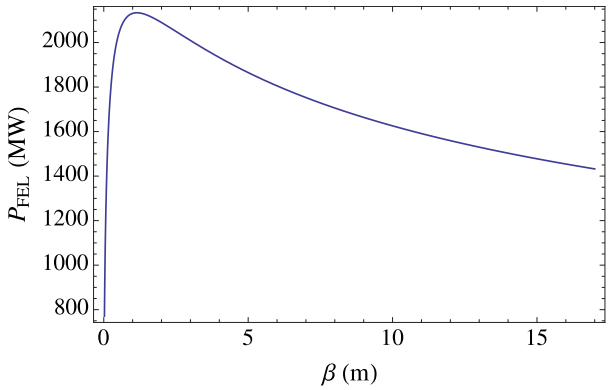

Fig. 16. FEL power as a function of the undulator matching β value.

which can be inserted in the definition of the inhomogeneous broadening effects to optimize to minimize L_g or in the derivation of the output power to determine an optimum value. Fig. 16 shows the FEL power as a function of β for $\gamma \simeq 2 \times 10^3$, $\lambda_u = 2$ cm and $\rho \simeq 1.57 \times 10^{-3}$.

A different way to estimate the optimum β value is provided by the following considerations. The inhomogeneous broadening associated with the emittance has a twofold origin. The first is due to the magnetic field dependence on the transverse dimensions and therefore linked to the transverse beam section. The other one is due to the beam divergence and is given by

$$\frac{\delta\omega}{\omega} \simeq \frac{\lambda_u \varepsilon}{\lambda \beta}(1+\alpha^2) \simeq \rho = \frac{\lambda_u}{4\pi\sqrt{3}L_g} \tag{110}$$

where α is the Twiss coefficient defined by $\alpha^2 = \gamma\beta - 1$. Furthermore, by introducing the radiation emittance ε_r, one finds

$$\varepsilon_r = \frac{\lambda}{4\pi}, \quad \beta \simeq \sqrt{3}\frac{\varepsilon_r}{\varepsilon}\frac{L_g}{1+\alpha^2} < \beta_n \tag{111}$$

representing a fairly good compromise between focusing and radiation and not in disagreement with the value obtained with analysis.

5. Undulator specifications and constraints

The characteristics and performance of every undulator are constrained by the requirements of the particular application that they are specifically designed for. The undulator interacts directly with the electron beam and can cause significant unwanted detrimental effects to the electron beam if due care is not taken by the undulator designer. In single pass FELs, including those driven by LPA, the physical and magnetic constraints for the undulators are quite different to those of storage rings and this can lead to some different and interesting design options. This subsection will discuss these differences in some detail.

5.1. Undulator minimum gap

The undulator gap is a parameter of noticeable importance, since it allows the tuning of the on axis magnetic field, whatever magnet technology is foreseen. Within this framework the definition of the minimum gap plays a role of paramount importance. The physical conditions to define the minimum gap are associated with the effect that it produces on the beam itself. A comparison between the undulator constraints on storage ring and FEL is reported in Table 1.

In storage ring dedicated to third generation Synchrotron Radiation sources, a small gap determines many conditions concurring to the reduction of the beam life time (as e.g. the local beta reduction and thus a decrease of the Touscheck beam life time). While in single pass driving FEL, the wake fields associated with the charged beam surface interaction induce a deterioration of the beam qualities, with a consequent dilution of the laser performance.

As the bunch travels through the undulator, the electrons induce image currents in the adjacent surface which then create electromagnetic fields, which act back on the bunch itself, and so changing the bunch characteristics via energy exchange. Since the image currents are traveling through the surface adjacent to the bunch, this surface is typically selected to be a high conductivity metal such as copper or aluminum to reduce the wakefield interaction. This metal surface can be the vacuum chamber itself, which sits inside the undulator magnet gap, or if the undulator itself is inside the machine vacuum, a metal foil can be attached to the undulator pole plane surfaces to ensure the electron beam

Table 1
Constraints on undulators for storage rings and single pass FELs and typical values for some of these parameters.

Constraint	Storage Ring	FEL
Vert. Aperture Limit	Lifetime	Wakefields
Vert. Aperture (mm)	∼4–5	∼3-5
Horiz. Aperture Limit	Injection	Wakefields
Horiz. Aperture (mm)	∼50	∼10
Vacuum (mbar)	10^{-9}–10^{-10}	10^{-7}–10^{-8}
Higher order fields	Sensitive	Relaxed
Phase error	Sensitive	Relaxed
Trajectory straightness	Relaxed	Sensitive
Synchrotron radiation heatload	Yes	No
Radiation damage concern	Yes	Yes
Total Magnetic Length (m)	2–5	30–100

interacts with a high conductivity material, rather than poor conductors such as steel poles or permanent magnet blocks. As might be expected, the physical distance between the electron bunch and this nearby surface affects the strength of the wakefield interaction. The closer the electrons travel parallel to this surface the stronger the interaction and the greater the impact on the bunch characteristics. The primary detrimental effect of the resistive wall wakefield is an increase in the energy spread of the bunch leading to gain degradation in the FEL amplifier. The electron bunches in a FEL have very large peak current, and extremely short electron bunches. Both quantities contribute to enhancing the strength of the wakefield. A criterion to fix the minimum gap is that of specifying the maximum tolerable reduction of the beam lifetime in SR or the maximum acceptable wakefield induced energy spread in single pass FEL. In both cases the size of the minimum tolerable gap can be recommended to be around 3 to 4 mm. For example, the Diamond storage ring currently operates in-vacuum undulators with a minimum vertical gap of 5 mm and the proposed Diamond-II lattice upgrade will then allow a minimum vertical gap of 4 mm [334]. Similarly, the NSLS-II storage ring has been designed to operate with a minimum in-vacuum undulator gap of 5 mm [335]. Since modern storage rings operate using top-up injection they can tolerate stored beam lifetimes as low as only a few hours. However, they are careful not to lower the lifetime too much as this increases the radiation levels and the frequency of injection which can impact on user beam quality temporarily. The LCLS-I FEL undulator section has a vertical gap of 5 mm, and the same for LCLS-II [336], and this has been calculated to induce an rms energy spread of 0.06% [337].

5.2. Undulator horizontal aperture

Another issue which affects the allowed physical shape of the magnet is the minimum gap in the other transverse plane.

In a storage ring, the minimum gap, discussed above, is always in the vertical plane because the storage ring itself is mounted in the horizontal plane. In this case the horizontal aperture within the undulator needs to be wider than the vertical primarily because of the electron beam injection process into the storage ring which causes the injected electrons to take an oscillatory trajectory in the horizontal plane, whilst they damp down. It is for this reason that vacuum chambers inside undulators are elliptical or racetrack in cross-section, with the horizontal aperture generally being several times larger than the vertical aperture. For example, the undulator horizontal aperture for the APS [338] and SOLEIL [339] are 50 mm and 46 mm respectively. Naturally, this means that the undulator magnet itself cannot impinge on this horizontal aperture requirement and so they are generally built as two separate arrays, one above and one below the beam axis. Recent on-axis injection schemes for low emittance rings can alleviate such a limitation.

In a single pass FEL there is no such injection process and the considerations for the horizontal plane are identical to those in the vertical. In other words, the aperture in both planes is set by the resistive wall wakefield interaction, and so, in an LPA FEL, the aperture cross-section can be circular, allowing the undulator magnet to impinge in the horizontal plane to an extent not allowed in a storage ring undulator. The undulator can even fully surround the circular aperture if required, which is highly desirable for some optimal helical undulator configurations. The undulator horizontal aperture for the LCLS-II FEL and European XFEL are 11.5 mm [336] and 15 mm [340] respectively.

5.3. Undulator field quality

5.3.1. Undulator good field region

The required undulator field quality also depends on the application. In a storage ring the electron bunch continuously passes through each undulator whereas in a single pass FEL the bunch only passes through once. The storage ring bunch is continuously sampling the magnetic fields of the undulator and is therefore much more sensitive to error terms or higher order field terms within the magnet which can drive unwanted resonance effects. Undulators must be carefully simulated and shimmed for use in storage rings to ensure these unwanted effects are sufficiently small so as not to limit the storage ring performance [341,342]. In an FEL these terms are of much less importance and magnetically the undulator tolerances

to higher order terms can be relatively relaxed. Consequently, considering the reduced horizontal aperture, the required good field region can be relatively small compared to a storage ring undulator and this would normally translate into narrower magnet arrays, reducing the total forces and magnetic material requirements.

The precision of the magnetic field and the absolute value of the undulator gap are quite crucial especially for an LPA based FEL due to the broad energy of the electron beam. For example, a gap error of 50 μm can shift the resonant wavelength by around 2 nm.

5.3.2. Undulator phase error and trajectory

Another difference between the two types of light source is that the storage ring undulators are utilized to very high orders by the beamline users (often to beyond the 15th harmonic of the fundamental), whereas the FEL process itself inhibits useful exploitation beyond the third, or sometimes the fifth, order of the fundamental. Consequently, the phase error [205,343] of the undulator, which determines the output quality of the higher orders especially, is more relaxed in an FEL undulator. For example, the LCLS-I undulator has a phase error tolerance of 10° [337] where as the NSLS-II has a target phase error of only 2° [335]. Conversely, the FEL instability process requires a continuous overlap between the emitted radiation and the electron bunch traveling through the undulator, and so trajectory straightness through the undulator is critical in an FEL when compared to a storage ring example [337].

5.3.3. Undulator length

The typical magnetic length of a storage ring undulator is a few meters whereas in an FEL the magnetic length can be many tens of meters. However, for the FEL, the complete undulator system is realized by breaking it down into a number of physically independent undulator modules which tend to be of similar length to storage ring examples (i.e. up to ∼5 m). This segmentation into discrete modules not only makes the assembly and handling of the undulators more practical but, more importantly, allows other essential accelerator elements to be installed readily along the full length of the FEL undulator section, in the space between undulator modules. These accelerator elements include quadrupoles to maintain optimal focussing of the electron beam and electron beam diagnostics, such as beam position monitors, to ensure the FEL operation can be set-up and maintained repeatably.

5.3.4. Undulator protection against radiation damage

In both types of light source facility, care is taken to ensure the undulators are not damaged by ionizing radiation from scattered electrons. Such damage, especially to permanent magnet based undulators, has been observed in both types of facility [344–346], in the past and machine protection systems, passive and active, are used to provide protection of the magnets.

One extra issue in a storage ring is that synchrotron radiation generated by the upstream dipole bending magnet must be carefully managed as well to prevent unwanted heating of vulnerable surfaces, especially in the case of in-vacuum magnets. Such heating within the undulator section is typically minimized through the careful implementation of a photon collimator system which is designed to intersect the synchrotron radiation before it reaches the undulator [334].

In summary, although undulators for storage rings and single pass FELs appear to be very similar, they do in fact have different constraints placed upon them which affects the absolute performance characteristics that they can achieve. Table 1 summarizes the various constraints for the two types of light source and gives typical values for parameters where possible. The different undulator technologies that can be used for an LPA based FEL are now discussed.

6. Cryogenic permanent magnet undulators

6.1. Permanent magnet undulators

6.1.1. Halbach design of permanent magnet undulators

Permanent Magnet Undulators (PMUs) [347] are able to function at room temperature and attain a large magnetic field. PMUs are typically in-air devices with comparably large undulator gaps, which limits the on-axis magnetic field. Most Pure PMUs use the Halbach geometric design [348,349], as displayed in Fig. 17a. The vertically magnetized magnets can be replaced with poles in the hybrid type, as shown in Fig. 17b, leading to an enhanced peak field [350], as shown in Fig. 18, in which Radia software [351] is used to compute the field.

6.1.2. A step towards short period high field undulators with in-vacuum ones

Achieving short period undulators with sufficient magnetic field sets requirements for the magnetic material. Shortening of the period requires reducing magnet size that results in a lower magnetic field. Increasing the magnetic remanence of a magnet is at the expense of its coercivity (i.e. resistance against demagnetization). So in-vacuum undulators [352–355], which avoid the beam pipe undulator gap limitation, were adopted to reach a small gap with a sufficient magnetic field in placing the magnetic arrays in vacuum. The mechanical design has then to be modified, for the carriage to handle the magnetic forces due to larger fields. The carriage typically consists of a metallic base and a frame in which two external girders are fixed on it. A system of rods and flanges enables to connect the internal girders where the magnet arrays are installed to external girders fixed to the carriage, which is designed to handle the magnetic forces. The carriage is equipped

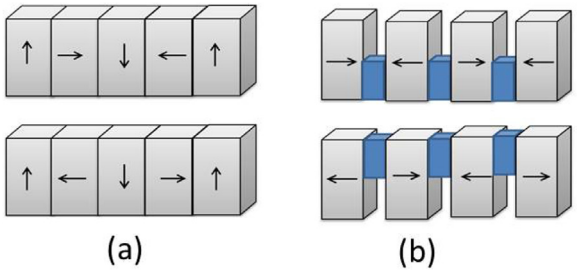

Fig. 17. Permanent magnet base undulator sketch: (a) Halbach geometry, (b) Hybrid undulator.

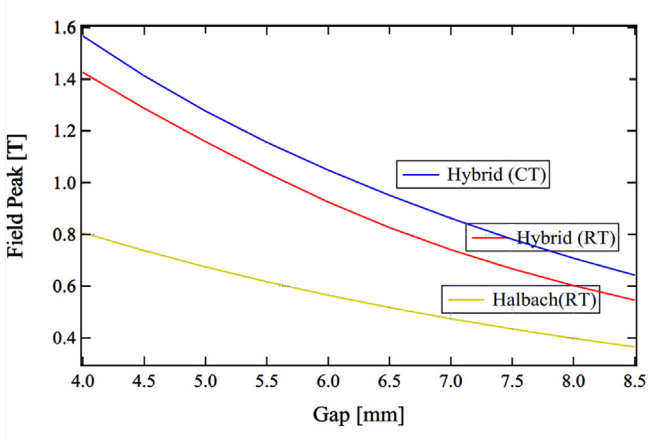

Fig. 18. Radia model comparing a pure permanent magnet, a hybrid and a cryogenic permanent magnet undulator of period 18 mm at room (RT) and cryogenic (CT) temperature. Used magnets: NdFeB: $B_r = 1.3$ T at RT, $B_r = 1.6$ T at CT. Vanadium Permendur poles are used for the hybrid design.

with motors for the movement of the gap and also sometimes for movement of the offset in order to adjust vertically the magnetic axis of the undulator to the electron beam axis. Linear and rotating encoders are currently used to read the absolute gap. In addition, a vacuum chamber and pumping system should be able to provide a good vacuum. Usually, the in-vacuum undulators are baked, so the magnet grade must cope with being heated; tests with unbaked in-vacuum undulators showed that beam conditioning can improve rapidly the vacuum [356]. The undulator vacuum chamber is connected to the standard chamber with specific RF tapers [357] for preserving a proper value of the impedance with or without water cooling. A liner (generally in Ni-Cu) is laid on the magnet arrays to evacuate the power deposition from upstream synchrotron radiation due to its high thermal conductivity and to reduce the wakefield interaction due to image current.

6.1.3. Magnet choice

Permanent magnets are characterized by their remanence B_r (strength of the magnetic field), coercivity H_c, energy product BH_{max} (density of magnetic energy) and Curie temperature T_c (temperature at which the material loses its magnetism). Permanent magnets [358], used for undulators combine Rare Earth (RE) ferromagnetic elements with incomplete f-shells and transition metals with d-shells such as Iron, Nickel and Cobalt. The RE magnets present a crystalline structure with a very high magnetic anisotropy (stable alignment of the atoms), enabling an easy magnetization along one direction, and a high resistance along the other. High magnetic moments at the atomic level combined with the high anisotropy results in a high magnetic field strength. Typical performance of $SmCo_5$ [359], $Nd_2Fe_{14}B$ [360,361], and $Pr_2Fe_{14}B$ magnets are presented in Table 2.

Magnets resistance to demagnetization [362,363], and heat budget are an issue, in particular for in-vacuum undulators, for which intermediate grades of $Nd_2Fe_{14}B$ ($B_r \leq 1.26$ T; $H_c = 1900$ kA/m) could be used. A choice of $Nd_2Fe_{14}B$ with high coercivity avoids demagnetization at Ultra-High-Vacuum (UHV) baking and radiation damage. A small inclusion of Dysprosium also allows for a larger coercivity. Typically, one should consider a coercivity larger than 1000 kA/m to avoid demagnetization at room temperature and larger than 2000 kA/m to prevent it at 120 °C (393 K), i.e. in baking conditions. Nevertheless, a magnet grade with a very large coercivity hinders the magnets remanent field and thus deteriorates the achieved magnetic field. So a balance has to be done between these two parameters to ensure the best performance possible for a given application.

Table 2
Typical characteristics of permanent magnets (at room temperature) used for undulators.

Magnet unit	B_r T	H_c kA/m	T_c K	(BH) kJ/m^3
$SmCo_5$	0.85	1400	720	150
Sm_2Co_{17}	1.1	2200	825	230
$Nd_2Fe_{14}B$	1.2	2300	585	370
$Pr_2Fe_{14}B$	1.2	1150	320	320

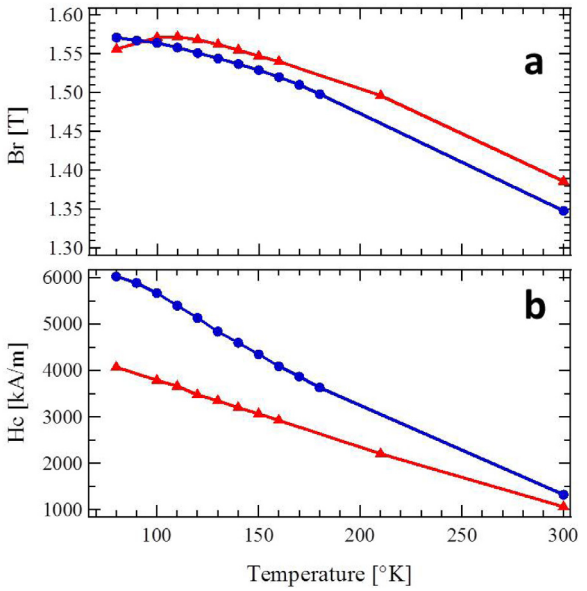

Fig. 19. (a) Remanent field and (b) coercivity measured for two magnets $Pr_2Fe_{14}B$ (●) and $Nd_2Fe_{14}B$ (▲).

6.1.4. New short period permanent undulators

The success of in-vacuum undulators has motivated the community to explore a novel method to fabricate undulator magnets with a very short period length, in the millimeter range. The usual permanent magnet based undulator technology employs accurately shaped magnet blocks, mounted on the non-magnetic holders, to be assembled and adjusted longitudinally on the rigid girders. For undulator periods below 1 cm, it becomes difficult to fabricate sufficiently accurate magnet blocks, poles and holders for ensuring the quality of the device. A first approach can consist of removing the magnet holder by introducing slots into the girder for the insertion of the magnets and poles. A more aggressive solution relies on the suppression of the magnet blocks themselves, in developing a plate-type undulator magnet made of Nd-Fe-B type magnetic material, thanks to an applied multipole magnetization method with a direction perpendicular to the plate surface, similarly to what is currently used for magnetic tape recording method in recording media [364,365]. A 4 mm period length field has thus being achieved so far, with a 0.4 T peak magnetic field at 1.6 mm gap [365] with reasonable field quality.

6.2. Cryogenic permanent magnet undulators

The idea of cooling down $RE_2Fe_{14}B$ magnets, which increases the remanent field and coercivity, was proposed [366], leading to the concept of cryogenic undulators. This undulator technology is highly suitable with compact accelerator based light sources such as LPA based FEL [367]. The maintaining of a high magnetic field while reducing the undulator period enhances the FEL performance by reducing the saturation length. In addition, it is highly robust especially when the shot-to-shot fluctuations of the electron beam is quite large.

6.2.1. Magnet behavior at cryogenic temperature

Typically, when the temperature of $RE_2Fe_{14}B$ is decreased by a factor of two, the remanent field increases by 10% and the coercivity by more than 50%. As the increase of coercivity is larger than the one of remanent field, one can even take a magnet grade that is less resistant at room temperature but presents a higher remanent field. Measurements [366,368–370] of the remanent field and coercivity for $Nd_2Fe_{14}B$ and $Pr_2Fe_{14}B$ versus temperature were performed, as shown in Fig. 19. For Neodymium grades at low temperature (130-140 K), the remanent field starts to decrease due to the so-called

Spin Re-orientation Transition (SRT) phenomenon [371–373], which exhibits a negative dependence of remanent fields against temperature due to a change in the preferred direction of the magnetization with respect to the easy axis of magnetization. In contrast for the Praseodymium grades, the remanent field continues to increase at low temperatures down to 77 K. These magnets can be cooled down further to lower temperatures and attain a higher remanence [374,375]. The coercivity of the two magnets continues to increase with lower temperature [376]. For the magnetic design for a given spectral range, because of the field enhancement, a shorter period than for an equivalent room temperature in-vacuum system can be considered, enabling to enhance the flux and the total number of periods.

6.2.2. Cryogenic permanent magnet undulator issues

With respect to standard in-vacuum undulators, there are several issues that appear in building Cryogenic Permanent Magnet Undulators (CPMUs) [377]. CPMUs are usually assembled and tuned at room temperature. Then, they are cooled to low temperature and further magnetic measurements are performed.

CPMU mechanical and thermal issues

From a mechanical point of view, the inner components inside the vacuum chamber should be modified so that liquid nitrogen can be introduced for cooling down the magnets at the targeted temperature. The operating temperature depends on the rare earth element that is used. Indeed, because of the SRT, $Nb_2Fe_{14}B$ cannot be directly operated at 77 K and thermal resistances have to be implemented. A $Pr_2Fe_{14}B$ based CPMU makes the cryogenic system simpler since the CPMU directly operates at the liquid nitrogen temperature. The liquid nitrogen can directly circulate inside the inner girders.

The thermal budget (i.e. heat load to be received by the undulator) has to be estimated before performing the thermal design of the CPMU. The thermal behavior of the inner girder can then be deduced. The eventual residual thermal gradient can be assimilated in a first approximation to a small taper. Between room and low temperature operation, the mechanical components are submitted to different thermo-mechanical changes, depending on the material thermal coefficients. By cooling down the system, the gap opens, because of the contraction of the supporting rods, and the period shortens, resulting from the inner girder contraction. Such a phenomenon has to be anticipated during the CPMU assembly at room temperature. Then, the phase error has generally to be slightly re-adjusted at low temperature, for example, by rod shimming. Because of larger magnetic forces related to the strongest magnetic field, an outer spring system can efficiently compensate for the deformation of support inner girders [378]. The majority of the CPMUs are not baked, hence once can exploit the advantage of a high remanent field grade. Usually, the liquid nitrogen performs a natural cryo-pumping when the CPMU is cooled down, and it can be then suitable for operation. The situation can be different if the temperature rises. Special care should be taken on the cleanness of the individual components [356].

Issues with CPMU optimization and measurements

A crucial step in the success of the realization of a CPMU results from the measurement of the magnetic field produced by the device at cryogenic temperature. It requires a specific measurement bench. While standard benches usually consist of a Hall probe system for the local field measurement and a bodyless coil (or a stretched wire) for the measurement of the field integrals, implemented on a stiff granite block enabling a precise position of the sensors and a sufficient reproducibility of the measurements, the CPMU Hall probe including the linear motion system has to be installed inside the vacuum chamber. It thus implies the development of an embedded measurement bench compatible with ultra-high vacuum, cryogenic environment and small available volume.

Dedicated benches have been developed. The first one has been developed at SPring-8 [379] with a Hall probe fixed at the extremity of a moving tube inside the undulator prototype using bellows. Then, ESRF [380] has built a full cryogenic measurement bench, including Hall probe with its linear motion in the chamber and stretched wire, with its motorized stages fixed on the extremities of a specific vacuum chamber. The chamber is divided in two adjacent parts: the bigger containing the girders and the magnetic assembly, and the smaller containing the linear guide rail and carriage for the Hall probe. The SOLEIL [381] bench is equipped with stretched wire motorized stages fixed on the undulator carriage and the Hall probe guide rail fixed on the floor through the lateral flanges of the vacuum chamber. The SAFALI concept, developed at SPring-8, consists in compensating the poor stiffness of the guide rail due to the absence of granite, by an active feedback of the transverse position of the probe while moving inside the undulator. Two laser beams that pass through two irises and illuminate Position Sensitive Detectors (PSD) measure the horizontal and vertical positions of the probe and its angle with respect to the undulator axis. The longitudinal position of the probe is acquired by an interferometer [379,382,383]. In the second version, the whole guide rail is displaced vertically and horizontally by motorized stages to compensate the measured variations of transverse position. A Hall probe bench for CPMU measurement was also designed by HZB, taking up the feedback concept and extending it to the angle active correction [384]. In addition to the system of laser beams, irises and PSD, the interferometer is a 3D one, returning information on the two other angles. The displacement is performed by six piezo motors embedded on the moving carriage.

6.2.3. Cryogenic permanent magnet undulator prototypes

Several CPMU prototypes were built at different locations, as indicated in Table 3.

SPring-8 [382] has built and optimized a 40 × 15 mm period $Nd_2Fe_{14}B$ based system, with RMS phase errors of 3.3° and 3.2° at 300 K and 130 K respectively. The temperature control at 140 K was enabled thanks to sheath heaters.

It then became attractive to use $Pr_2Fe_{14}B$ magnets for being able to operate at lower temperature, thus with a larger magnetic field and coercivity. A first prototype of 8 × 14.5 mm period NSLS [385], using $Pr_2Fe_{14}B$ magnets (NEOMAX 53CR)

Table 3
Characteristics of CPMU prototypes developed.

Unit	λ_u mm	N_u	B_r T	Gap mm	B_{peak} T
SPring-8	15	40	1.56	5	0.92
NSLS II	14.5	8	1.64	4.85	0.92
NSLS II n°2	16.8	8	1.4	5	1.12
SOLEIL n°1	20	4	1.58	10	0.57
SOLEIL n°2	18	4	1.58	10	0.5
SOLEIL n°3	15	5	1.55	10	0.43
HZB n°1	9	20	1.62	2.5	1.12
HZB n°2	9	11		2.5	1.28
RadiabBeam n°1	7	42		1.87	1.11

Table 4
Characteristics of full-scale developed CPMUs.

Location Unit	λ_u mm	N	B_r T	Gap mm	B_{peak} T	Status
SLS n°1	14	120	>1.5	3.8	1.186	Installed
SLS n°2–5	17					Planned
ESRF n°1	18	107	1.16	6	0.88	Installed
ESRF n°2	18	107	1.37	6	0.99	Installed
ESRF n°3	14	140	1.62	5	1	Installed
ESRF n°4	18					Construction
ESRF n°5	20					Construction
ESRF n°6	18					Construction
ESRF n°7–9	16					Construction
Diamond n°0	17.7	113	1.32	5 (4)	1.04 (1.263)	Installed
Diamond n°1–3	17.6	113	1.62	4.6		Construction
Diamond n°4	16.7	125	1.62	4.6		Construction
Diamond n°5–6	15.6	128	1.62	4.6		Planned
SOLEIL n°1	18	107	1.58	5.5	1.15	Installed
SOLEIL n°2	18	107	1.57	5/5.5	1.12	Installed
SOLEIL n°3	18	107	1.57	5/5.5	1.12	Installed
SOLEIL n°4	15	200	1.57	3		Construction
IHEP	13.5	140		5	1	Test
TPS	15	133	1.7	4	1.3	Built
SPring-8	15	93	1.48	3	1.64	Built
HZB n°1	17	88	1.62	5.5	1.12	Installed
HZB n°2	15	175	1.6	2	2.08	Construction
SSRF n°1	20	80	1.53	6	1.07	Test
SSRF n°2	20	80		6	0.91	Test
SSRF n°3						Construction

and Vanadium Permendur poles, has been measured in the Vertical Test Facility at liquid nitrogen and He temperatures with a slight increase of the RMS phase error at lower temperature (3.1° at room temperature and 3.5° at 77 K). A second system [386] developed at NSLS-II, using a grade of $Pr_2Fe_{14}B$ magnet that can be baked (NEOMAX CR47) led to a higher field than the previously employed grade (at 80 K : 1.12 T for the CR47 and 1.22 T for the CR53).

Three CPMU prototypes were built at SOLEIL. The first one [369], a 4 × 20 mm period hybrid $Nd_2Fe_{14}B$ system shows a 11.5% increase of the magnetic field between room temperature and cryogenic temperature of 140 K the operation temperature. The second one (4x18 mm period) [387] and the third one (4 × 15 mm period) $Pr_2Fe_{14}B$ hybrid type (NEOMAX CR53) [388] takes advantage of the absence of SRT phenomena. The magnetic field grows by 13% between room temperature and cryogenic temperature of 77 K.

A 20 × 9 mm period $(Pr,Nd)_2Fe_{14}B$ (Vacuumschmelze Vacoflu × 50) cryogenic undulator [389] with $Co_{49}Fe_{49}V_2$ poles with saturation magnetization of 2.35 T, built jointly by Helmholtz-Zentrum Berlin and Ludwig-Maximilian-University München (LMU), shows a increase of the remanence by 20% and of the peak field at the fixed gap of 2.5 mm by 11% with partial saturation of the pole pieces from 300 K to 30 K. The second prototype with modified poles exhibits a larger field [390] and it enabled to observe synchrotron radiation [391] using the MAMI-B beam line with 855 MeV beam. RadiaBeam Technologies has also developed a 42 × 7 mm period cryogenic prototype using $Pr_2Fe_{14}B$ and Vanadium Permendur poles (this design also considered the use of textured dysprosium poles) [392]. A remaining thermal gradient was observed [393].

6.2.4. Full-scale cryogenic permanent magnet undulators

The construction of full scale devices (see Table 4) to be installed on synchrotron light source beamlines has started at ESRF (France) [380,394–396], with a 2 m long full scale 18 mm period $Nd_2Fe_{14}B$ magnet (NEOREM 595t) hybrid CPMU.

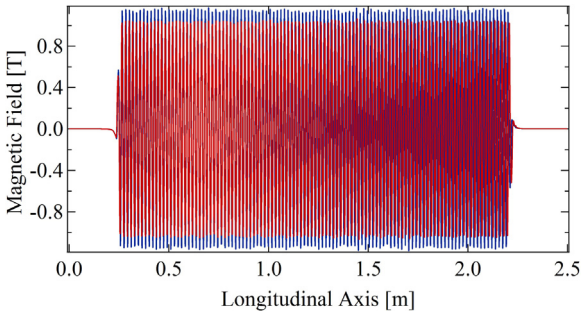

Fig. 20. Magnetic field measured along the undulator axis with a Hall probe at both room temperature (red) and cryogenic temperature (blue).

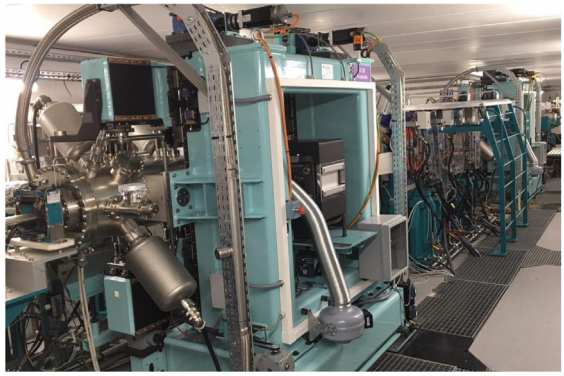

Fig. 21. The two CPMUs (U18 n° 1 and U18 n° 3) installed at SOLEIL nanoscopium beamline.

The peak field is increased by 6% when cooled down from 273 K to 150 K at gap 6 mm. The RMS phase error slightly increases from room temperature (4.8°) to 150 K (5.7°), because of a residual longitudinal temperature gradient. It is the first full scale (2 m length) CPMU to be built and installed for operation with an electron beam and a liquid nitrogen closed loop for cooling. A second CPMU has been built and installed at ESRF with two additional $Pr_2Fe_{14}B$ based hybrid undulators being under construction. New CPMUs [397] are now under development for the ESRF upgrade.

At the Paul Scherrer Institute (Switzerland) [383,398,399], a full scale 1.7 m long 14 mm period CPMU using $Nd_2Fe_{14}B$ (Hitachi NMXS45SH) magnets and Vanadium permendur poles, cooled with LN2, had been measured with SAFALI. The measured phase error of 1.1° is similar to the one measured at room temperature, thanks to an in-situ correction method. With SLS-II upgrade, it is planned to replace 4 in-vacuum U19 undulators by CPMU.

SOLEIL (France) [381,388,400–404] has built and measured the first $Pr_2Fe_{14}B$ (CR53) based full scale hybrid cryogenic undulator (2 m long, 18 mm period) cooled down to 77K with LN2. The phase error at 5.5 mm gap at room temperature of 2.8° RMS increases up to 9° at 77 K, but has been corrected down to 3° by shimming the rods. It is the first $Pr_2Fe_{14}B$ full scale cryogenic undulator installed on a synchrotron radiation facility, and is in use on the Nanoscopium beamline as shown in Fig. 21. SOLEIL built three more cryo-ready devices using a different $Pr_2Fe_{14}B$ grade with an enhanced coercivity (1912 kA/m): two 2 m long CPMU (U18) have been successfully built and optimized, one is used for the COXINEL project [405–407] and one is again installed on the Nanoscopium beamline as shown in Fig. 21, and a 3 m long U15 providing a high peak field of 1.65 T at 77 K for 3 mm gap. Fig. 20 presents a magnetic measurement using a Hall probe for the CPMU n° 1 for an undulator gap of 5.5 mm. The field is enhanced by a $\sim$ 10.6% from room to cryogenic temperature which is consistent with the RADIA model simulations.

At DIAMOND (UK) [408], a 17.7 mm period full scale $Nd_2Fe_{14}B$ (Vacodym 776TP) based hybrid CPMU has been built by Danfysik [409]. As the temperature is decreased from 300 K to 157 K, the field is increased by 7.03% at 4 mm gap while for 10 mm gap the increase in field is 8.69%. At 157 K, the RMS phase error is measured to be 3.5° at 4 mm gap. New $(Pr,Nd)_2Fe_{14}B$ CPMUs are presently under construction (three for DIAMOND II) and three additional for DIAMOND upgrade.

Based on earlier prototypes, HZB (Germany) [410–412] have developed two full scale CPMUs of 88 $\times$ 17 mm and 15 mm period length, and gap sizes of 5 mm and 2 mm, investigating two cooling concepts based on liquid nitrogen and single-staged cold heads, respectively. $(Pr,Nd)_2Fe_{14}B$ magnets (from Vacuumschmelze) treated with a grain boundary diffusion process for an enhanced stability, and Co-Fe poles were used. The gap size is measured using an optical micrometer. A phase error of 4.6° has been measured for CPMU17 [413], which is now installed at BESSY. CPMU15 is developed for a plasma-driven FEL experiment in close cooperation with Hamburg University.

Table 5
Width of magnets and poles for different periods, as well as the coefficients of the fitting curves.

Period	Magnet width	Pole Width	a	b	c
18 mm	6.5 mm	1.25 mm	3.743	−4.053	0.69459
15 mm	5 mm	1.25 mm	3.895	−4.022	0.52895
12 mm	4 mm	1 mm	3.986	−4.087	0.67293
10 mm	3.5 mm	0.75 mm	3.531	−3.647	0.40497

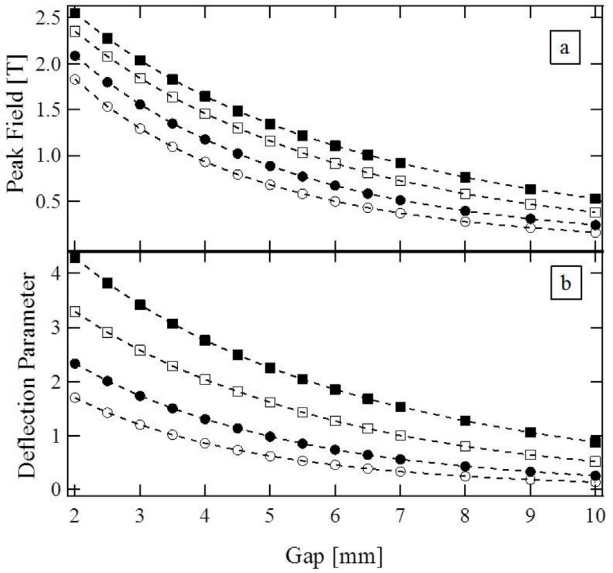

Fig. 22. (a) Peak field and (b) deflection parameter versus the magnetic gap for different periods : 18 (■), 15 (□), 12 (●), 10 (○) mm..

National Synchrotron Radiation Research Center (NSRRC) on TPS (Taiwan), in collaboration with Neomax EngineeringCo [414–416] has built a 2 m long 15 mm period CPMU. It contains a force compensating spring module to handle the strong magnetic forces, enabling the demonstration of a phase error lower than 2° in the 4–10 mm gap range. A CPMU magnetic measurement bench has been developed and tested, with a carriage and optical components being redesigned to improve the reproducibility. Further devices are foreseen.

IHEP (Beijing, China) is building a 2 m long 13.5 mm period CPMU using $Pr_2Fe_{14}B$ [417,418].

A 2 m long cryogenic undulator with 140 periods of length 13.5 mm is to be built for the High Energy Photon Source Test Facility (HEPS-TF) in Korea [419]. This undulator consists of $Pr_2Fe_{14}B$ magnets (NMX 68C) to operate at 4 mm gap with a magnetic field of 1.3 T and will be cooled down to liquid nitrogen temperature (80 K), reaching a magnetic field of 1 T at a gap of 5 mm.

Two CPMU have been built and measured at Shanghai Synchrotron Radiation Facility (SRRF, China) [420] in order to equip the ring with three devices. A first one (80 × 200 mm period) uses $Nd_2Fe_{14}B$ magnets (N48H grade), and reaches a peak field of 1.07 T at 6 mm gap at cryogenic temperature. The second one uses $Pr_2Fe_{14}B$ magnets (P46H grade), and reaches a peak field of 0.91 T with a phase error of 4.4° at 6 mm gap at cryogenic temperature.

6.2.5. CPMU scaling

A scaling of the CPMU field for different periods can be performed. Fig. 22 displays the peak fields versus gap of different period length undulators, computed with RADIA software, using a newly introduced $Pr_2Fe_{14}B$ grade with field remanence of 1.7 T. The magnetic field can be fitted with the equation:

$$B_{peak} = a.exp[b.\frac{g}{\lambda_u} + c.(\frac{g}{\lambda_u})^2] \tag{112}$$

where g is the magnetic gap, and a, b, c are the fitting coefficients, given in Table 5.

6.2.6. CPMU prospects

It should be possible to increase further the magnetic field, then reduce the period, and enhance the number of periods for a given CPMU length by combining a CPMU with high temperature superconducting coils [421]. For example, the field for a CPMU of period 15 undulator at 5.5 mm could be enhanced by 7% with coils at 77 K and 22% with coils at 40 K.

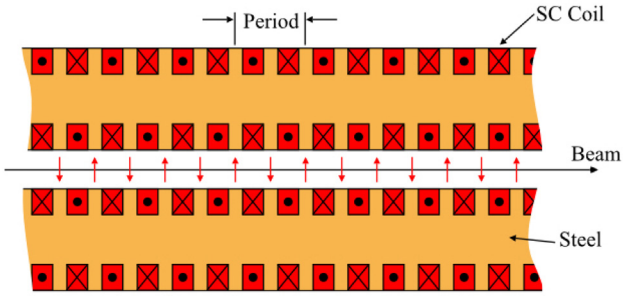

Fig. 23. Schematic side view of a planar SCU showing how the SC wire is wound around two independent steel formers to generate the periodic magnetic field.

Another idea is to adapt the gap to the shape of the electron beam envelope, in the so-called adaptive gap undulator concept [422]. It enables to satisfy the stay-clear and impedance constraints with segments of different periods. The flux enhancement is typically of 10%.

For variable polarization, one could refer to the crossed undulator concept [423–425] with two separate segments, with a phase sifter in between. In the past, in-vacuum permanent magnet based Elliptically Polarized Undulators (EPU) have been built, but without a full flexibility [426,427]. Nowadays, DELTA type EPU [428] or in-vacuum APPLE II [429] undulators are under development. A cryogenic option could be considered.

7. Superconducting undulators

Superconducting technology is routinely applied to the development of high field strength magnets for applications such as Magnetic Resonance Imaging and particle physics accelerators and detectors. It is perhaps surprising then that short period superconducting undulators (SCUs) are still not a mainstream solution for accelerator based light sources, with just a few examples being in use today. The reason for this rather slow uptake is in large part due to the extremely successful application and ongoing improvements in permanent magnet undulator technology rather than any specific shortcomings in superconducting technologies. Despite the undoubted success of permanent magnet systems, there is still a clear margin in performance advantage to be gained through the application of superconducting materials and it is for this reason that a number of groups around the world have been actively pursuing the detailed development of short period, high field SCUs for light source applications over the past ten years or more [430]. This research and development effort has led to the construction of a few SCUs which are now installed and in daily use on storage ring light sources in Germany [431] and USA [432,433]. These particular examples have exhibited very good operational performance in terms of reliability, stability, and user experience and this has increased confidence within the accelerator community such that national FEL light source facilities, such as LCLS-II, have carefully assessed employing SCUs rather than permanent magnet alternatives in their baseline configurations [434].

The specific advantages of SCUs over PMUs highlighted by the LCLS-II team are; the higher magnetic fields allowing superior FEL performance or reduced undulator length, the radiation hardness compared to PMUs offering long lifetime and smaller magnet gaps, the anticipated reduction in resistive wakefields due to the cold bore, the much lower vacuum pressure due to cryo-pumping reducing gas scattering, the smaller footprint and simpler magnet field control compared with the massive adjustable-gap PMU, and the easy re-orientation for vertical polarization, if desired. The project team estimated that the LCLS-II hard X-ray undulator could be shortened by up to 70 m using an SCU in place of the baseline 145 m long PMU designed to operate at up to 5 keV in SASE mode [434].

7.1. Superconducting undulator magnetic design

The magnetic design of planar SCUs is very straightforward, with a similar approach being adopted by all of the research groups working in this area. The typical arrangement is shown in Fig. 23. Two independent sets of superconducting windings on steel formers are arranged such that the current flows transversely orthogonal to the electron beam and so generates the periodic magnetic field required [435,436]. The two sets of windings are held apart by a non-magnetic mechanical arrangement, which is not shown in the figure. The former is made of a high quality magnet steel and the superconducting wire employed is either NbTi or Nb_3Sn. The SCU typically operates at close to 4 K. NbTi is more commonly used, even though Nb_3Sn has far superior properties on paper with even greater fields within reach, as it is much easier to work with, in terms of winding, insulation, and stability. Nb_3Sn has to be heat treated after winding to create the superconducting alloy and afterwards is rather fragile. Nb_3Sn also suffers from instability issues at the field levels required by SCUs (below 5T) as it is primarily targeted at far stronger magnetic field applications [437]. Research on the use of special grades of Nb_3Sn better suited to SCU applications has been carried out primarily at LBNL [438].

7.2. Superconducting undulator mechanical design

Although the magnetic design of SCUs is straightforward, the engineering challenges are severe and this is the area which has held back SCUs from widespread adoption so far. The mechanical tolerances are very tight and these must be maintained as the magnet is cooled down from room temperature to ∼4 K. The gap separation between the two sets of windings is typically between 5 to 10 mm. The coils are at ∼4 K and any heat transfer from the electron beam to the coils, due to wakefields or synchrotron radiation, must be very low to prevent the magnet quenching. This is generally resolved through the insertion of a vacuum chamber isolating the beam from the magnet arrays. This vacuum chamber is physically and thermally separated from the magnet and cooled to an intermediate temperature of ∼20 K, to intercept and absorb any emitted power from the electron beam, by whatever physical process. A further issue is that the magnetic field quality is not just determined by the steel pole shape and location but is also strongly dependent upon the superconducting wire placement. The accurate placement of individual wires, to a tolerance of a few tens of microns, is a painstaking process and difficult to maintain over a length of more than a few tens of cm. For this reason, and also to achieve the required machining tolerances, the complete SCU magnet is sometimes made up of shorter sections which couple together to form a longer device [439]. Post-assembly magnet shimming, which is a standard technique for permanent magnet undulators, is not easy to implement in an SCU. Many schemes have been proposed but they add an extra layer of complexity which teams try to avoid if at all possible [440]. In addition, the proposed schemes often require additional windings or use valuable space within the magnet gap and so also serve to lower the maximum possible peak field that the SCU can achieve. For these reasons several groups aim to construct SCUs that have excellent field quality on first assembly and so need no shimming capability. This is only possible by working to very tight tolerances at all stages of manufacture and assembly but has been demonstrated to be a practical approach.

7.3. Examples of superconducting undulators

An example of an SCU installed in a storage ring is the SCU15 in the KIT synchrotron in Germany [441], where SCU15 has been in operation with beam since the beginning of 2015. The SCU15 has a period length of 15 mm and 100 full periods. Since at the KIT synchrotron a vertical beam stay clear of 15 mm is needed during electron beam injection and energy ramping, and at the full energy of 2.5 GeV a minimum gap of 7 mm is allowed, the beam vacuum chamber is adjustable, as the magnet gap is closed, from 7 mm to 15 mm vacuum gap. The magnetic peak field measured at the maximum coil current of 150 A is 0.73 T. The undulator coils are wound from NbTi and are cooled using cryocoolers only, with no liquid cryogens being required. The use of cryocoolers, which require only electricity and water to operate, is particularly convenient for facilities without the infrastructure or expertise required for handling liquid helium. During one year of testing in the storage ring the SCU15 operated reliably without quenches in the normal operating mode at 2.5 GeV. Two quenches were observed at 1.3 GeV due to poor orbit control when setting up a special low-alpha operating mode. The undulator recovered quickly from the quenches and was ready for operation again within 15 min.

The same storage ring has recently installed a second SCU, called SCU20 [442], with lessons learnt from SCU15 being applied to the design and manufacture of this second device. The thin rectangular NbTi wire, having an insulated cross-section of 0.54 x 0.34 mm has been replaced by a thicker round wire with 0.76 mm insulated diameter, which is claimed to be more robust and with superior electrical insulation [443]. Also, the cobalt–iron yoke, previously used on SCU15 has been replaced by a low-carbon steel which, although it has inferior magnetic performance, is easier to procure and machine. The SCU20 has a period length of 20 mm, a peak field of 1.18 T, and 74 full periods, giving it the same physical length as SCU15. SCU20 has been operating with beam in KARA since January 2018 without any quenches.

Another example of an SCU installed and successfully operating in a storage ring is SCU18-1 [444] in the Advanced Photon Source in the USA, which built upon the experience gained from the 30 cm long SCU0 device which was their first SCU to be installed [445]. SCU18-1 has an 18 mm period and a fixed magnet gap of 9.5 mm, achieving a peak field of 0.97 T. The magnetic length is 1.1 m. The magnet is wound using round NbTi wire with a diameter of only 0.6 mm. Nevertheless, the SCU comfortably operates at a current of 450 A, well within the maximum current achieved of 520 A. The SCU18-1 has been in operation since May 2015, and a second identical example, replacing SCU0 in the storage ring, called SCU18-2 was installed in September 2016. A new mechanical arrangement that allows for the magnetic gap to be compensated during the final assembly and measurement process was implemented between the development of the two SCU18 devices. This resulted in the phase error of the second device being as low as 2° RMS, whereas the first device, which did not have this gap compensation system, has a phase error of more than 5° RMS, which is still impressive without the use of any shimming.

The same team have recently fabricated a helical SCU for the APS by winding a pair of coils in a continuous spiral along a round former [446]. It should be noted that whilst such a magnet will generate circular polarization, the helicity of the polarization is fixed by the coil geometry and cannot be changed by reversing the direction of current in the coils, as is sometimes assumed. Also, for this SCU the magnet bore diameter is relatively large at 31 mm as, although narrow vertical gaps can be tolerated, a wide horizontal gap is required in the storage ring for the reasons discussed earlier in this paper. A narrow bore helical SCU of very similar design has been fabricated previously by Daresbury and Rutherford Appleton Laboratories in the UK for a different application [447]. A summary of the principle SCUs that have successfully operated on storage ring light source facilities is given in Table 6.

Table 6
Parameters of storage ring SCUs which have been installed and operated successfully. Gap is the beam chamber vertical aperture.

Facility	λ_u [mm]	N	Gap [mm]	B_{peak}
KIT synchrotron	14	100	8	0.3
KIT synchrotron	15	100.5	7	0.73
KIT synchrotron	20	74.5	7	1.18
APS	16	20.5	7.2	0.8
APS	18	59.5	7.2	0.97
APS	31.5	38.5	8	0.4

7.4. Prospects with superconducting undulators

There are no operating single pass FELs that utilize SCUs currently although they are being considered now by new facilities and the LCLS-II project implemented an active R&D programme that resulted in prototypes being constructed based upon both NbTi and Nb_3Sn [434]. A UK collaboration, led by Daresbury Laboratory, has recently been working on the development of SCUs specifically designed for FELs, by taking on board the different constraints that were discussed in Section 5. This has led to the proposal that the internal vacuum chamber between the two SCU coil arrays can be removed in the FEL case. The internal vacuum chamber enables a suitable UHV environment for adequate beam lifetime and also absorbs any stray synchrotron radiation and power deposited due to resistive wall wakefields. Since the vacuum levels are far more relaxed in a FEL and any long wavelength, low power, stray synchrotron radiation can be absorbed with collimators, the only real concern for the FEL is the management of the wakefields. It is proposed that the impact on the electron beam is minimized by attaching a very thin copper foil to the SCU arrays, presenting a high conducting surface to the electron beam, and that any power deposited is simply absorbed by the magnets directly at 4 K. In the standard SCU the internal vacuum chamber is not in direct contact with the magnets, and so the magnet arrays are thermally isolated from the chamber, which is typically operated at around 20 K.

This simple change of removing the internal vacuum chamber transforms the SCU performance in an analogous manner to the way that permanent magnet undulators were transformed when in-vacuum permanent magnet undulators were first developed. Significant engineering efforts are required to make the internal vacuum vessel have as little impact on the SCU magnet gap as possible but even with wall thicknesses of ∼0.5 mm and similar thermal insulating spacing between this surface and the SCU coils and poles the magnet gap is increased by typically ∼2.0 mm compared to the aperture needs of the electron beam itself, although one group has managed to reduce the gap increase down to only 1.0 mm whilst maintaining good thermal decoupling between the vessel and coils [443]. Reducing an undulator magnet gap from ∼7 mm to ∼5 mm simply by the removal of a vacuum chamber makes a tremendous difference to the achievable peak magnetic fields. The UK group state that an SCU cooled with a cryo-cooler system can comfortably continuously absorb 0.1 W per meter length of undulator at 4 K [448]. They calculate that the power deposited due to resistive wall wakefields, which depends linearly on the bunch repetition rate, is below this value for low repetition rate FELs (<500 Hz) even with extreme combinations of bunch charge and length. Furthermore, the long undulator sections required by FELs, of order 100 m, will be more cost effectively cooled using a centralized cryoplant coupled to a cryogenic distribution system, rather than by a very large number of independent cryocoolers [446]. The cooling power of liquid helium refrigerators is very impressive and they would easily enable several Watts per meter at 4 K to be handled. This then should mean, with careful thermal design and implementation, that SCUs without the internal vacuum chamber ('in-vacuum' SCUs) are also compatible with the high repetition rate FELs (MHz bunch rates) if a centralized cryoplant is implemented [446]. It is worth noting that storage ring electron beams also typically deposit up to a few Watts per meter at 4 K so they are again compatible with this type of in-vacuum SCU if cooled by a central cryoplant infrastructure.

7.5. Superconducting undulator scaling

To compare the two types of SCU, one with the internal vacuum vessel and one with only a thin copper liner the UK group have modeled the peak magnetic field in the undulator as a function of electron beam aperture and period using Opera 3D for over sixty separately optimized cases. The magnetic modeling assumes commercially available rectangular cross-section NbTi superconductor with a safety margin of 20%, operating at 4 K. Each model has been individually optimized for the number of discrete windings per layer and for the number of layers. For the case with the internal vacuum vessel the magnet pole gap is assumed to be 2 mm larger than the electron beam aperture (2 × 0.5 mm vacuum wall thickness plus 2 × 0.5 mm thermal separation between the 20 K vessel and the 4 K magnet steel former and windings) and for the alternative case (in-vacuum SCU) the magnet pole gap is only 0.2 mm larger than the electron beam aperture (2 × 0.1 mm copper liner mounted directly on the pole surface). A summary of the modeling results is given in Fig. 24. An empirical equation has been fitted to these modeling results [449] as follows:

$$B_u = (0.33 + 0.068\lambda_u - 1.05 \times 10^{-3}\lambda_u^2 + 5.9 \times 10^{-6}\lambda_u^3) \times e^{-\pi(g/\lambda_u - 0.5)} \quad (113)$$

where B_u is the peak field on-axis, and g is the magnet gap between the steel poles. The actual electron beam gap will be less than this depending upon whether an in-vacuum or out of vacuum scheme is used.

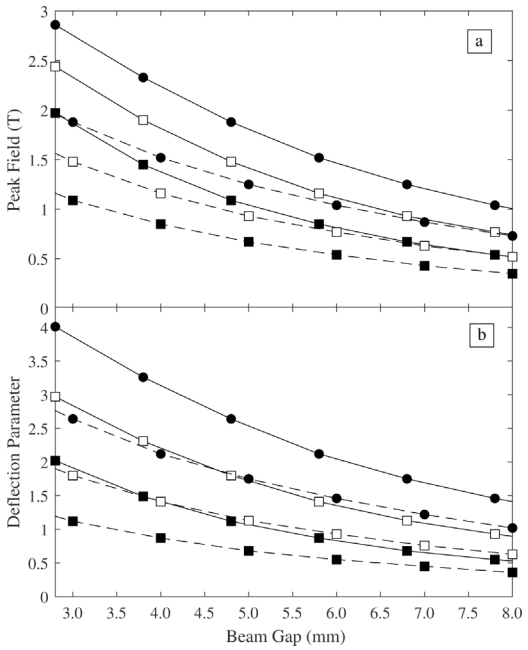

Fig. 24. Results of detailed 3D magnet modeling of planar SCUs showing (a) peak field and (b) deflection parameter versus magnetic gap. Solid lines are in-vacuum SCU and dashed lines are standard SCUs with (•) period 15 mm, (□) period 13 mm, and (■) period 11 mm.

8. Transverse gradient undulators

Transverse gradient undulators (TGUs) are considered to be a promising solution for FELs which aim at utilizing electron beams with a large energy spread such as beams generated by laser plasma accelerators.

The basic idea of TGUs is to make both the electron energy γ and the undulator deflection parameter K_u a function of the transverse position, either x or y, and to match these such that:

$$\lambda = \frac{\lambda_\mathrm{u}}{2\gamma(x|y)}\left(1+\frac{K_\mathrm{u}^2(x|y)}{2}\right) = \text{const.} \tag{114}$$

That is achieved by spectrally dispersing the beam and introducing a transverse undulator field amplitude gradient. By applying this concept to FELs with an adequate choice of dispersion and field gradient, the effect of the energy spread on the FEL resonance condition can be minimized and the gain thereby be strongly increased.

The original concept [90] aimed at relaxing the requirements on the electron beam quality for an effective FEL amplification and thereby particularly improving the performance of storage ring-driven low-gain FELs. It was later also considered for optical klystrons in storage rings and has recently been re-considered for storage ring based X-ray FEL oscillators [450] and High-Gain-Harmonic-Generation (HGHG) X-ray FEL schemes [451].

The TGU concept has been adopted for LPA-driven high-gain FELs [89] and showed its potential to achieve short gain lengths, high saturation power and a narrow bandwidth in the FEL using electron beams with a relative energy spread at the level of a few percent. There is a trade-off between the steepness of the transverse field gradient on the one hand and the increase of the transverse beam size due to the dispersion on the other hand: while the former generates an additional effective energy spread for finite-emittance electron beams, the latter leads to a reduced transverse coherence of the FEL radiation [452] as well as a reduction in the brilliance and the gain [69]. Optimum dispersion values turn out to be in the range a few centimeters. In turn, transverse deflection parameter gradients $\alpha_{K_u} = \frac{\mathrm{d}K_u}{\mathrm{d}x}$ of 50 m^{-1} to 300 m^{-1} are required.

The modified TGU-FEL theory proposed in [89,452] is based on simplifying assumptions regarding the TGU itself. The question how higher order terms of the transverse field profile as well as higher-order dispersion terms in realistic beam transport set-ups affect the FEL gain in TGUs, an important issue (as first underscored in [453]) and still is a matter of an onging debate [69,454].

8.1. TGU design concepts

The typical conceptual view of a TGU is that of a transversely tapered planar insertion device as depicted in Fig. 25(a), in which the transverse field gradient is achieved by a linear transverse variation of the magnetic gap. The transverse field

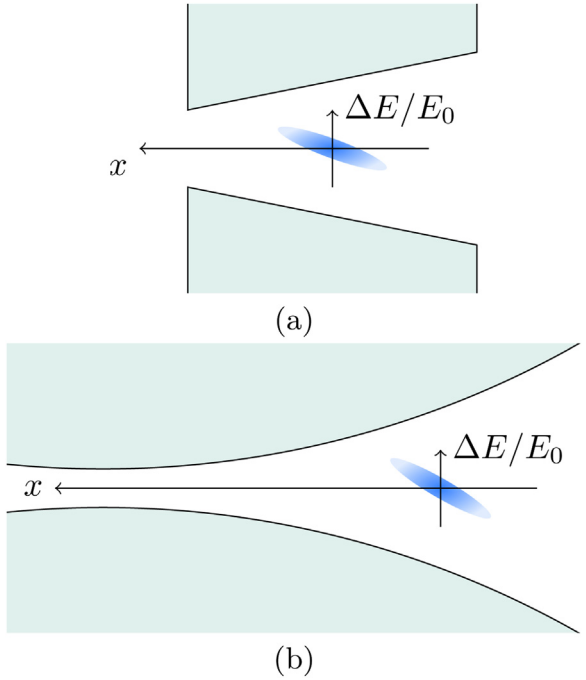

Fig. 25. Possible TGU realizations using specifically designed pole shapes: (a) transverse taper, (b) convex (in this case circular) pole shape.

profile of a transversely tapered undulator can be calculated analytically. This calculation yields a weakly exponential dependence of the field amplitude on the transverse coordinate [455,456]. Achievable transverse gradients for realistic short-period devices ($\lambda_u \leq 20\,\text{mm}$) are limited to the order of $\alpha_{K_u} \lesssim 100\,\text{m}^{-1}$. Alternative analytically treatable x-dependent gap designs with curved, more precisely convex (e.g. hyperbolic or circular) pole shapes were investigated [457]. Convex pole shapes imply a faster than linear growth of the gap width and therefore larger transverse gradients than achievable with a linear transverse taper. Moreover, by appropriately shaping the poles, in principle a transverse field profile can be achieved that is linear in a sufficiently wide range of the transverse coordinate. A particularly simple TGU design with circular poles [456,458] provides large transverse field gradients and a moderately large region with approximately linear transverse field shape.

A transverse variation of the magnetic gap is not the only possible way of realizing a TGU. Two alternative approaches have been proposed recently. In fixed-gap APPLE-type undulators, where the K_u-value is adjusted via longitudinal movements of the neighboring magnet arrays, a transverse K_u-gradient is necessarily present [459]. A design concept for a superconducting APPLE-X-type TGU has recently been proposed [460]: Depending on gap width and K_u-value, this K_u-gradient can be in the order of 50 m^{-1} to 150 m^{-1} for a permanent-magnet APPLE-X undulator with 40 mm period length and up to 380 m^{-1} for a superconducting APPLE-X undulator with 26 mm period length.

A further approach to realizing a TGU [461] utilizes the natural field amplitude gradient in the non-deflection direction y which is present in planar undulators for $y \neq 0$. That is achieved by both offsetting the beam from the undulator's symmetry axis and spectrally dispersing it in the y-direction, i.e. perpendicular to the deflection in the undulator. The K_u-value in a planar undulator depends on y as

$$K_u(y) = K_{u,\text{axis}} \cosh(k_u y), \tag{115}$$

which means that for a chosen beam axis $y_0 \neq 0$ the K-gradient is

$$\alpha_{K_u} = K_u(y_0) k_u \tanh(k_u y_0), \tag{116}$$

For $\lambda_u \sim 20$ mm this K_u-gradient takes values of a few 10 m^{-1} to 100 m^{-1}. The intriguing simplicity of this approach comes at the cost of a highly non-linear dependence of the field amplitude on the transverse coordinate which limits the usable y-range and thereby the energy acceptance of this type of TGU.

All these TGU designs have in common that the transverse field gradient affects the beam dynamics inside the undulator in a potentially undesirable way, if corrective measures are not taken. In designs where the directions of spectral dispersion and oscillatory motion of the particles are parallel to each other, as is the case for tapered or convex poles, a ponderomotive particle drift in the direction of the field amplitude gradient occurs. This effect can be suppressed by superimposing a weak correction field constant in z [457]. The required horizontal profile of the correction field depends on the horizontal profile of the TGUs main field. For the cylindrical TGU an approximately parabolic correction field shape is required, which can be generated by long racetrack correction coils placed inside the undulator coil formers [458].

Table 7
Comparison of TGU parameters for different concepts and realizations.

Type	Place	Status	λ_u mm	h_g mm	K_u	α_K m^{-1}
transv. tapered PMU	SIOM/	Built	20		1.15	50
transv. tapered PMU	SINAP				1	
transv. tapered SCU	KIT	Simul.	20	7	2	100
cylindric SCU	KIT	Built	10.5	2.4	1.07	149.5
APPLE-X PMU	PSI	Built	40	3	1	150
APPLE-X SCU	PAL	Simul.	26	9.5	1.97	160
				0.8	380	

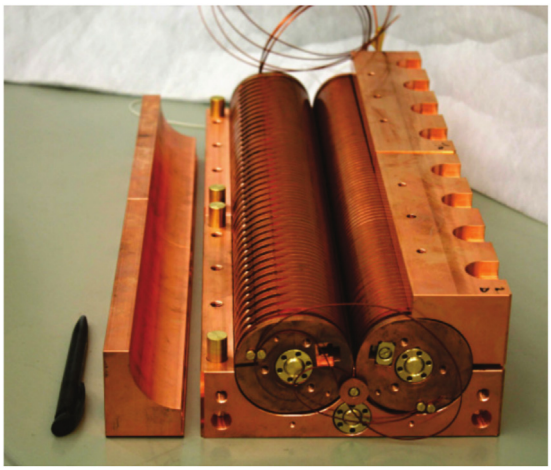

Fig. 26. Photograph of the superconducting 40-period TGU manufactured at KIT, Karlsruhe, Germany.

In the case of the approach utilizing the natural field amplitude gradient in the *y* direction, the spectral dispersion and the oscillatory motion of the particles are perpendicular to each other and the ponderomotive effect is absent. Instead of that, the particle trajectories are bent towards the undulator's symmetry plane due to the natural focusing present in planar insertion devices [461]. The compensation of this effect is achieved by additional focussing.

8.2. TGU realizations

Although the concept of TGUs has been considered for nearly forty years, no such device has so far been experimentally tested. Two prototypes or prototype series, respectively, have been built and are currently awaiting a detailed magnetic characterization and experimental application (see Table 7).

At the Shanghai Institutes of Optics and Fine Mechanics (SIOM) and of Applied Physics (SINAP), Shanghai, China, four fixed-gap TGU modules with $\lambda_u = 20$ mm and 75 periods each have been constructed [453,462]. These TGUs are hybrid permanent magnet devices of the linear transverse taper type with a canting angle of 7.5°, yielding a transverse gradient of $\alpha_{K_u} = 50\,m^{-1}$ at a K_u-value of 1.15. These undulators are intended to be used in a TGU-FEL demonstration experiment at the LPA setup at the SIOM 200 TW laser facility [138,463].

The second device, shown in Fig. 26 is a superconducting cylindrical TGU manufactured at KIT, Karlsruhe, Germany [456,464] and foreseen for a TGU demonstration experiment at the JETI laser facility located at the Friedrich-Schiller-University Jena, Germany. This TGU is a 40-period prototype with $\lambda_u = 0.5$ mm and a transverse gradient of $\alpha_{K_u} = 149.5 m^{-1}$ at a *K*-value of 1.07. A quench test as well as a Hall-probe measurement of the magnetic field at one longitudinal and seven transverse positions as a function of operation current have been performed on this superconducting TGU, showing an excellent agreement with the theoretical expectation [465]. The undulator has recently been installed in its own cryostat and a detailed magnetic characterization is under preparation.

9. Exotic undulators

Exotic undulators could also be considered.

9.1. Bi-harmonic undulators

In order to enhance generation of high order harmonics in high gain FEL devices, non-conventional undulator schemes are considered in which the on-axis field oscillates either in both transverse directions or in the same direction with

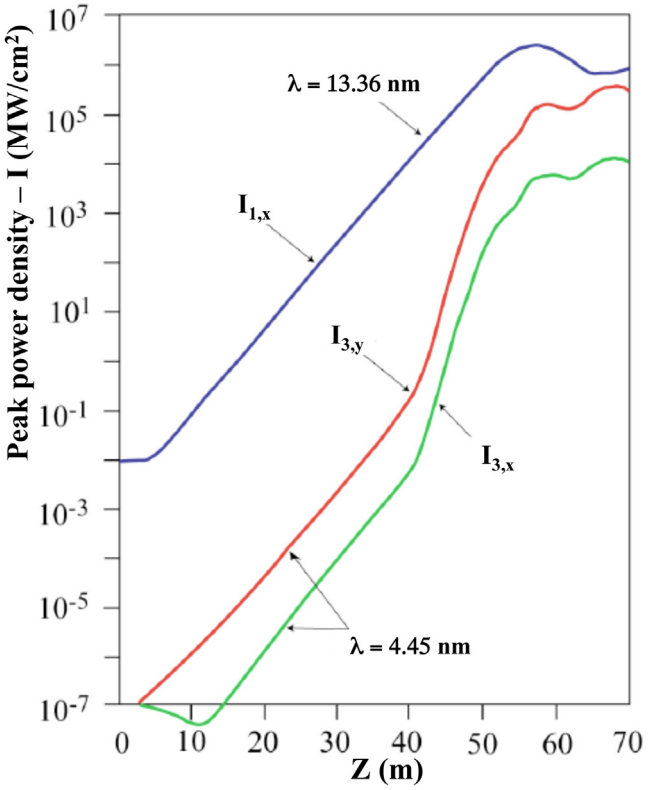

Fig. 27. Power growth of main and third harmonics for a bi-harmonic undulator with $d = h = 3$, $E = 1078$ MeV, $\lambda_u = 6$ cm, $K_u = 0.99$, $\rho = 1.258 \times 10^{-3}$.

different periods. These types of undulators are called bi-harmonic [466–469]. As a first example, one considers the undulator configuration where the on-axis field oscillates with different orthogonal polarizations:

$$\vec{B_u} = (d\,B_u \sin(h\,k_u z), B_u \sin(k_u z), 0) \tag{117}$$

where h is an integer number and $k_u = 2\pi/\lambda_u$. The particular case with $d = h = 3$ ensures that the K_u magnetic strengths associated with the horizontal and vertical electron motions are the same. In this particular device, the fundamental harmonic is polarized along the horizontal direction, while the third vertically polarized harmonic is associated with the magnetic field oscillating at $\lambda_u/3$. This harmonic can be considered as a fundamental one for this undulator component, with maximum power compatible with the fundamental harmonic associated with the period λ_u, as shown in Fig. 27.

For completeness, one also mentions the bi-harmonic configuration with parallel rather than orthogonal B_u and $B_h = d\,B_u$ magnetic components, namely with the on-axis magnetic field given by:

$$\vec{B_u} = (0, B_u \sin(k_u z) + d\,B_u \sin(h\,k_u z), 0) \tag{118}$$

In this case, the resonant wavelength is given by :

$$\lambda_R = \frac{\lambda_u}{2\gamma^2}\left[1 + \frac{K_u^2}{2}\left(1 + \frac{d^2}{h^2}\right)\right] \tag{119}$$

Undulators of the bi-harmonic type have been proposed and built in the past, they raised interest to extend to tunability of Synchrotron Radiation sources [470] and not yet explored for FEL operation. The relevant spectral properties have been studied in detail [471] and the associated FEL performances have been discussed in [214,471] under a variety of possible configuration. The advantages of these devices to enhance the radiation are evident, in particular if they are exploited in the last sections where the effect of bunching is more substantive. The main problems are associated with a not straightforward engineering structure and a field which is hard to characterize using standard tools, however these drawbacks can be overcome by an appropriate design of the magnets, using e.g. quarter-foils configurations.

9.2. Plasma undulators

Plasmas can generate and sustain very high static fields, and give rise to the strong collective phenomena such as plasma waves. The idea of plasma applications for manipulation and, in particularly, undulation of relativistic electrons

dates back to 1980–90s. At that time, a few concepts were proposed involving the oscillations of electrons guided in the ion channels [472], or imposing the wiggling motion by coupling electron beams to the plasma waves [473]. In these schemes, the laser plasmas produced in gas targets with the densities 10^{15} – 10^{17} cm^{-3} were considered, which defines the undulator periods of $\lambda_u \sim 10^2 - 10^3$ μm, and for the to-date laser intensities ($I_L \sim 10^{14}$ W/cm^2), the undulator strength could reach $K_u \sim 0.1 - 1$. Potentially, with such parameters X-rays can be produced even using relatively low energy electron beams with limited collimation quality. On the other hand, a low number of oscillations, which could be produced in the accessible experimental conditions, and requirement of high laser energy and stability has hindered these developments for a long time.

In recent years the concept of underdense plasma undulators have been revised for the state-of-the-art experimental conditions. The plasma wave undulator has been studied in coupling with LPA, and the possibility of keV photon generation along a few tens of wiggler periods with $\lambda_u \sim 10$ μm and $K_u \lesssim 1$ has been demonstrated with an advanced numerical approach [474]. Another approach, derived from the "channel" scheme, consists of applying to electrons the wakefields of a laser pulse injected off-axis into a plasma channel in such a way that the laser centroid oscillates transversely [475]. This scheme can potentially provide few tens of $\lambda_u \sim 1 - 2$ mm wiggler periods with the strength of $K_u \sim 1$ and be coupled to LPA. Further numerical studies revealed the potential tunability of such sources in terms of wavelength and polarization of the produced radiation [476]. An alternative to the gas-based plasma schemes utilizing an undulator based on the overdense plasma was proposed recently [477]. In this approach the laser driver from the LPA ionizes a series of nanowires arranged in a chessboard fashion, which generates electrostatic fields to deviate the accelerated LPA electrons. Such a plasma undulator can provide strengths of $K_u \sim 1$, and its period does not rely on plasma density, but is defined by the target design, and could be as small as $\lambda_u \sim 10^1 - 10^2$ μm.

The main interest of plasma undulators is related to their potential to produce strong undulating fields with sub-millimetric periods. In the present state these schemes remain mainly theoretical concepts, and in the short term their experimental validations for the synchrotron light production are required.

9.3. Microwave undulator

The idea of causing electrons to oscillate transversely, for the purpose of synchrotron radiation emission, by using electromagnetic waves instead of static magnetic fields was first raised in 1968 [478]. These devices are generally referred to as RF or microwave undulators because the frequency of the electromagnetic wave that has been considered falls in this part of the spectrum as this is where there is considerable expertise in suitable cavity or waveguide design and also sources of very high power RF are available. The transverse electric and magnetic fields in the wave contribute to the electron oscillation amplitude. A key advantage of the microwave undulator is that very short periods can be generated (i.e. 5 to 15 mm), using high frequency RF, with reasonable K_u parameters of 0.5 to 1.0, whilst maintaining a relatively large aperture for the electron beam (examples given below have beam apertures from 8 to 39 mm). This combination of short period, large gap, reasonable K_u is not feasible in a static magnetic field undulator. An additional potential advantage is the ability to change the parameters dynamically, shot to shot, and so alter the photon output characteristics rapidly to suit the experiment. Rapid switching of polarization has been suggested as a useful characteristic to lower signal to noise levels in some experiments. The first demonstration of a microwave undulator was in the mid eighties [479] when a device with an equivalent period of 55 mm (2.9 GHz) and K_u parameter of 0.24 was built and shown to generate light from an electron beam as expected. Following this demonstration the idea seemed to lose favor, probably because conventional undulators improved rapidly and because the high power RF systems required were either very expensive or not available. However, in the past few years a number of groups have taken up the idea again, especially in the light of advances in high frequency RF power sources and cavity and waveguide design expertise. A device with an equivalent period of 13.9 mm (11.4 GHz), aperture of 39 mm, and K_u parameter of 0.7 was built and successfully tested with beam in 2014 [480] followed by a detailed theoretical analysis of the radiation emission from microwave undulators [481]. Other groups are now looking at the design of optimized corrugated waveguide based solutions using even higher frequencies [482,483] of 30.3 GHz (5 mm period, K_u of 0.14) and 36 GHz (4.3 mm period, K_u of 0.5). Two options for the waveguide design operating at 36 GHz assuming a challenging yet feasible input power of 50 MW have been generated. They both achieve similar K_u parameter of 0.5 (equivalent B_u field of 1.25T) with one solution having a beam aperture of 8 mm and the other 18 mm. Achieving equivalent parameters in a state of the art static magnetic undulator at the same period would require a beam aperture of around 1 mm. This clearly demonstrates the future potential and advantage of the microwave undulator.

9.4. Optical undulator

Similar to the microwave undulator, an intense optical laser can be used to achieve an undulator period several order-of-magnitude shorter than previously mentioned [484–486]. This method can realize the X-ray FEL with a multi-MeV electron bunch within a centimeter long interaction length, making them suitable for LPA based X-ray FEL emission. The drawback of such undulator is the low magnetic field, which translates to a lower value of the FEL Pierce parameter and thus a lower power gain.

Table 8
Undulator radiation measured from an LPA electron beam for a wavelength λ, a relative wavelength $\Delta\lambda/\lambda$.

Laboratory	λ nm	$\Delta\lambda/\lambda$ %	λ stability nm (%)
Institut Fur Optik [74]	740	7.4	∼93 (12.5)
MPQ [75]	18	30	∼1.5 (8)
LOA [77]	230–440	18	–
Strathclyde [76]	160–220	16	∼23 (13)
COXINEL [79]	200–300	7	5 (2.6)

10. Examples of the use of state-of-the-art undulators for LPA based spontaneous emission and FEL

The path towards LPA based FEL presents different alternatives. The first direction consists in exploiting the present LPA performance and adapting the transport line towards the undulator to manipulate the electron beam properties, to then adopt the different steps of an FEL experiment with a proper observation of the undulator spontaneous emission, followed by the measurement of FEL gain at rather large wavelength, and then a decrease towards shorter wavelengths. The second approach consists in searching the LPA configuration space to optimize it so that it directly fulfills the electron beam requirements for a straightforward FEL amplification. In this section are first reviewed the challenges for LPA based FELs, the observations of LPA based undulator radiation, the progress on test LPA based FEL experiments with state-of-the-art performance, and the prospects with specifically designed LPA for the FEL application, as developed in the frame of EuPRAXIA [487]. Of course, because of the small size of laser plasma accelerators, compact high field short period undulators are considered here.

10.1. Challenges of LPA based FELs

The advent of present X-ray FELs came along with the spectacular development of conventional accelerator technology, aimed at future linear colliders. Typical $\sim$ GeV beams exhibit 1 mm transverse size,1 μrad divergence with 1 mm longitudinal size and 0.01% energy spread. In contrast, LPA still usually present larger divergence and energy spreads, that can lead to significant emittance growth [84–86]. Collective effects and coherent synchrotron radiation can also play a role [87]. The present LPA electron beam properties are not directly suited for enabling FEL amplification, and electron beam manipulation is likely to be required.

10.1.1. Handling of the divergence

The LPA process creates a beam with a divergence significantly larger than that from conventional linear accelerators. The plasma medium by itself enables symmetrical focusing with the plasma lens [158–160,488]. In addition, quadrupoles, as used in conventional accelerator technology, can be employed. Because of the required quadrupole strength, permanent magnet based ones are often be preferred to electromagnetic ones. There have recently been several developments of high gradient variable strength permanent magnet quadrupoles [489–494,494–496]. The two focussing approaches have been compared [497] while conventional accelerator technology remains more robust, the option remains for them to be combined if required.

10.1.2. Handling of energy spread

Electron beam energy spread can be very critical for an FEL applications. A large energy spread and the associated inhomogeneous broadening counteracts the energy modulation, thus washing out the bunching along the undulator line. In order to be on the safe side, the Pierce parameter and the energy spread are required to satisfy the condition in Eq. (75). LPA based electron beams are characterized by short bunches and large energy spread.

Therefore, in contrast to what happens in ordinary linear accelerators, a decompressor chicane is foreseen to increase the bunch length and reduce the energy spread even by a factor 10 [73,88,498]. Taking advantage of the introduced correlation between the energy and the position, the slices can be focused in synchronization with the optical wave advance, in the so-called supermatching scheme [499]. The chicane scheme also enables to lengthen the electron bunch, to avoid the slippage effects, namely the poor overlapping between electron and radiation inducing additional gain reduction. As mentioned earlier, it was proposed in the early FEL studies, when energy spreads were of the order of 0.1%, to use a TGU [90,500]. The concept is to impose an electron optics solution which introduces a transverse displacement as a function of beam energy at the entrance to a TGU [89,455,501] enabling to selectively fulfill the undulator resonance condition for all electrons at a particular TGU gradient.

10.2. First observations of LPA based undulator radiation

The feasibility of achieving spontaneous undulator radiation with an LPA source has been demonstrated at different laboratories. Table 8 summarizes some of the undulator radiation characteristics observed so far using an LPA source.

The measured radiation bandwidth is still quite wide with a rather poor wavelength stability. The undulator radiation quality achieved so far does not yet reach what is currently achieved on storage ring accelerator based light sources.

10.2.1. Institute fur optik und quantenelektronik

A high-intensity Titanium:Sapphire laser of 5×10^{18} W cm^{-2} and pulse duration of 80 fs was used to produce the relativistic electron beams [74]. The laser pulse was focused by an off-axis parabolic mirror into a supersonic helium gas jet where it accelerated electrons to several tens of MeV energy. The electrons propagated through an undulator, producing synchrotron radiation, and into a magnetic electron spectrometer. Radiation was collected by a lens and analyzed in an optical spectrometer. The electron spectrum peaked at 64 MeV with a width of 3.4 MeV (FWHM), i.e. RMS energy spread of ∼2.3%, and contained a charge of 28 pC. The normalized emittance of the beam was estimated to be $\varepsilon_n \approx 1.3\pi$ mm.mrad, derived from beam optics simulations and the beam divergence measured from the beam size. The undulator radiation was measured using a spectrometer. The spectra was peaked at 740 nm with a bandwidth of 55 nm and contained 284,000 photons. Another peak was observed at a wavelength of 900 nm produced by a 58 MeV, 14 pC and 5% energy spread in another shot.

10.2.2. Max–Planck-institut fur quantenoptik Germany

The beamline was customized to generate soft-X-ray undulator radiation from an LPA electron beam [75]. Driven by the Atlas Titanium:Sapphire laser, the plasma–cell creates electron beams of up to 210 MeV peak energy. The beam was captured and focused using miniature permanent magnet quadrupole lenses. The quadrupoles provided a field gradient of level 500 T/m and were adjustable in longitudinal position to tune the electron transport to different beam energies. Focused into a miniature undulator ($\lambda_u = 5$ mm, 60 periods), the LPA electron beam generated spontaneous undulator radiation, which was detected using a custom transmission-grating-based photon spectrometer. The first harmonic was measured at 18 nm and the second harmonic at 9 nm.

In a later extension of the experiment [502] a variable-length plasma–cell target delivered electron energies in excess of 400 MeV and generated undulator radiation extending into the water window at 4 nm wavelength (first harmonic). Tuning the plasma target to provide different electron energies and tuning the electron beam transport, the setup could show octave-spanning wavelength tunability in the range from 4 nm to 13 nm.

10.2.3. Laboratoire d'Optique Appliquée

At Laboratoire d'Optique Appliquée, the beamline is designed for the generation of UV undulator radiation with LPA electron beams [77]. A Titanium:Sapphire laser delivering a linearly polarized pulse at 800 nm with more than 1 J energy, about 30 fs duration was focused on a helium gas jet leading to an electron density of 5×10^{18} cm^{-3}. The generated relativistic electrons pass through a triplet of permanent magnet quadrupoles placed 15 cm from the source providing 15.4 T/m, −25 T/m and 15 T/m gradients, followed by a 0.6 m long undulator of period 18.2 mm and a deflection parameter of 1. The photon beam transverse size was measured with a CCD camera, which imaged a position corresponding to 60 cm after the end of the undulator and for an electron energy of 120 MeV energy. The vertical FWHM divergence of the radiation is about 3 mrad.

10.2.4. Strathclyde university UK

An Advanced Laser-Plasma High-energy Accelerator towards X-rays (ALPHA-X) accelerator beam line has been commissioned [76]. A Titanium:Sapphire laser pulse centered at a wavelength of 800 nm with full-width at half-maximum duration of 36 fs and peak intensity of 2×10^{18} W cm^{-2} was focused to a 20 μm waist at the leading edge of a 2 mm diameter helium gas jet to form a relativistic self-guided plasma channel. The electron beams produced were initially collimated using a triplet of miniature permanent magnet quadrupoles of fixed gradients of 500 T/m. A triplet of electromagnetic quadrupoles then focused the beam through the undulator with gradient ∼2.4 T/m. Undulator output radiation was detected using a vacuum scanning monochromator and a CCD camera. The energy distribution measured had a mean central energy of 104 MeV, with a 5% relative energy spread, and contained a mean charge of 1.1 ± 0.8 pC. The mean spectral bandwidth of the radiation was 69 ± 11 nm corresponding to a relative band width of 32 ± 7%, decreasing to as low as 16%.

10.2.5. COXINEL, SOLEIL, LOA, PhLAM, France

COXINEL (Coherent X-ray source inferred from electrons accelerated by laser) is aiming at demonstrating FEL amplification with the help of a dedicated transport line to handle and manipulate the beam properties, in the frame of the LUNEX5 project of advanced compact FEL demonstrator [72,503,504]. The key concept relies on an innovative electron beam longitudinal and transverse manipulation along the transport line towards the undulator. The line, designed and built at Synchrotron SOLEIL [406], is installed at Laboratoire d'Optique Appliquée (LOA), where LPA development is carried out using a Ti:Sapphire laser system delivering 1.5 J, 30 fs FWHM pulses. The divergence is rapidly mitigated (5 cm away from the source) via strong focusing provided by a triplet of permanent magnet quadrupoles. These so-called QUAPEVA high gradient permanent magnet quadrupoles present a variable strength (via rotating cylindrical permanent magnets surrounding a central Halbach ring quadrupole [505]) and an adjustable magnetic center position (via translation tables) [157,494]. A magnetic chicane then longitudinally stretches the beam, sorts electrons in energy and selects the energy range of interest via a removable and adjustable slit mounted in the middle of the chicane [506]. A second set of quadrupoles matches the beam inside an undulator. Undulator radiation covers the UV range with a 180 MeV electron beam and a U18 undulator (107 periods of 18.16 mm, variable gap between 4.55–30 mm, reaching 1.2 T peak field at

minimum gap) [370,400,402] and the VUV domain at 400 MeV electrons with a U15 undulator) [388,401]. The electron beam can be monitored with current transformers and cavity beam position monitors or by inserting scintillator screens along the line [507]. The electron optics, a source to image optics, refocuses the beam inside the undulator thanks to the strong gradient QUAPEVA quadrupoles [87,499,508]. The LPA is operated in the robust ionization injection regime [110] with a supersonic jet of He-N_2 gas mixture, providing electrons with energies up to 250 MeV, 0.5 pC/MeV charge density, and few mrad divergence (1.2–5 mrad RMS). The electron beam can be properly transported along the line [78,508–511], using a Beam Position Alignment Compensation strategy to mitigate alignment residual errors and electron beam pointing drifts, enabling to independently adjust the position and the dispersion. The undulator radiation transverse distribution has been measured using a CCD camera installed 3 m away [78] and is in agreement with models. The total estimated number of photons per beam charge N_{ph} is $\approx 3.10^7$ pC^{-1}. The large energy spread (typically 30% RMS at the undulator position after filtering along the line) is reduced to a few percent by introducing a slit to select a small portion of the energy distribution [511]. A UV spectrometer, equipped with two collimating mirrors, a 600 gr/mm grating and a CCD camera, installed 3 m from the undulator exit, images the spatio-spectral flux of the produced radiation using a CaF_2 lens that focuses the radiation into the spectrometer entrance slit [79]. The measured radiation exhibits the typical moon shape pattern (quadratic dependence of the resonant wavelength versus the observation angle), characteristic of undulator radiation [512–514]. The chromatic effects of the lens, however, introduce a distortion of the moon shape to a more triangular one [79]. The radiation linewidth can be controlled using the electron beam energy selection via the slit in the chicane [79,508]. The achieved undulator radiation wavelength stability reaches 2.6% [79].

10.2.6. Lux

The Lux laser-plasma accelerator [515], operated by Hamburg University and DESY, has the mission to combine laser-plasma concepts with the state-of-the-art in modern accelerator technology. It is driven by the 100 TW-class Angus Ti:Sapphire-based CPA laser system. The whole laser is integrated into the accelerator controls system to monitor and stabilize its performance. The accelerator supports day-long operation at 1 Hz repetition rate with energies on the order of 400 MeV and bunch charges of several 10 pC. The large number of events provides exceptional statistics to correlate laser and electron parameters and enables tuning of the electron bunch properties.

The electron beam is captured and focused through a miniature undulator (Beast II, $N_u = 60$, $\lambda_u = 5$ mm) using an electromagnetic quadrupole doublet of up to 150 T/m gradient. The generated radiation is detected using a transmission-grating based spectrometer. First experiments have shown undulator radiation tunable in the range of 11 nm to 4 nm [516]. The generation of spontaneous undulator radiation is mainly considered a benchmark for the quality of beam transport and diagnostics.

10.3. Examples of LPA based FEL test experiments with present electron beam performance

The COXINEL line has been designed with baseline reference parameters at source using a 6D Gaussian bunch without any correlation having a 1 π.mm.mrad total normalized RMS emittance, a 1 mrad RMS divergence, a 1% RMS relative energy spread with a 1 μm RMS bunch length, 34 pC charge and 4 kA peak current for electron beam energies ranging from 180 MeV to 400 MeV. The seeded configuration is adopted. For a SASE evaluation, the beam is transported from source to image, which is at the undulator center, and the slice beam parameters are used to calculate the power achieved for different beamline characteristics. A maximum power of 70 MW is attainable with a magnification factor of 10 and chicane strength of 0.2 mm. Extensive simulations were carried out [499], and included a number of FEL sensitivity studies [517], using the production code GENESIS [518] and the unaveraged spectral code CHIMERA [519]. The chromatic matching enables the gain of one order of magnitude growth on the FEL intensity compared to a strong focusing of the electron beam [499]. Different regimes can be considered, depending on the electron beam parameters and the operating wavelength. In the seeded configuration, the chirp introduced in the chicane, induces a red shift of the FEL radiation wavelength with respect to the seed. It can lead to an interference fringe pattern, that can allow for a full temporal reconstruction of the FEL pulse temporal amplitude and phase distributions [520]. An FEL test experiment is underway, and the main limitation so far comes from the measured electron beam parameters that do not match the baseline ones. Improvements of the LPA performance are in progress.

The Lux beamline is currently being upgraded to enable the demonstration of FEL gain using LPA beams. The new beamline layout closely follows the decompression concept as described in [521]. The beam will be captured using a quadrupole doublet and stretched in a decompression chicane, thereby reducing the slice energy spread. Undulator radiation is generated in a cryogenically cooled [410] CPMU ($N_u = 130$, $\lambda_u = 15$ mm, K_u: 1–3). The goal of this experiment is not to achieve saturation, but to show the onset of gain. Simulations indicate that a bunch charge of order 20 pC and a relative energy spread of 1% at 300 MeV beam energy would be sufficient for a first experiment. Those parameters are close to the current performance of the Lux plasma accelerator.

The aim of the Lawrence Berkeley National Laboratory test experiment at Berkeley, USA, is to demonstrate a tunable FEL in the UV down to soft X-ray range using an LPA source [522]. The 4 J laser is focused onto the target (2.5 J) with a pulse duration of 36 fs (FWHM) generating electron beams of tunable energy between 100 MeV and 300 MeV. The electron beam is first handled by either a triplet of quadrupoles or an active plasma lens, followed by a chicane, another set of quadrupoles and finally a 4 m long undulator of period 18 mm with a deflection parameter varying between 0.89 - 1.26.

The operating FEL will thus be around 55 nm–400 nm. Transport simulations, using Elegant [523], and FEL simulations, using GENESIS [518], show a gain of 10^4 and 10^3 at the wavelengths 420 nm and 55 nm, respectively [524,525]. Much effort has been expended on the electron beam optimization to produce high quality bunches to satisfy the FEL condition [526].

A collaboration of KIT and the Friedrich-Schiller Universität (FSU) Jena aims at experimentally demonstrating, investigating and advancing the concepts involved in compact TGU-based LPA-driven FELs. That encompasses developing and demonstrating an efficient beam transport with a large momentum acceptance and TGU matching as well as demonstrating the feasibility of a high-gradient, short period (superconducting) TGU and experimentally proving the TGU concept with spontaneous emission of undulator radiation. The demonstration experiments were originally designed for the LPA installed at the JETI40 laser system at the FSU, assuming an electron energy of 120 MeV, an average relative energy spread of 4% (including shot-to-shot variation) and an average initial beam divergence of 2.5 mrad, including pointing jitter. For the proof-of-principle experiment using spontaneous undulator radiation, a 40-period superconducting TGU has been built (see Section 8 above), the commissioning and magnetic characterization of which is currently ongoing. A linear dogleg chicane matching the LPA-generated electron bunches to the dynamical acceptance of the TGU was realized and successfully experimentally tested [465,527,528]. The experiment design is currently under revision and the components of the setup are being upgraded for an upcoming experimental campaign at the new laser system JETI200. This campaign together with complementary experiments will provide a basis for empirically founded conclusions on the expected FEL performance as well as on advanced TGU designs.

The Shanghai Institutes of Optics and Fine Mechanics (SIOM) and of Applied Physics (SINAP), Shanghai, China, in collaboration with the SLAC National Accelerator Laboratory are setting up a TGU beam line at the SIOM 200 TW laser facility [462,463]. The LPA installed at this laser facility provides an electron beam with energies tunable in the range 200–600 MeV with $\sim$ 1% energy spread and a relative shot to shot energy variance in the order of 5%. Bunch charges up to 80 pC and an initial beam divergence of 0.3 mrad are reported [138]. The experimental setup is foreseen to consist of the permanent magnet TGUs described above in Section 8 and a compact beam line using a single dipole for creating the required spectral dispersion of the beam. The beam line is designed for a central beam energy of 380 MeV, corresponding to a resonant radiation wavelength of 30 nm. GENESIS [518] simulations show that a significant FEL gain within the 6 m TGU line can be expected with this setup.

10.4. Future prospects with optimized LPA for FEL application

The path towards LPA based FEL in the X-ray domain requires an extensive optimization of the electron beam generation, of the transport line while selecting a compact undulator. Great efforts have been carried out in the frame of the EuPRAXIA collaboration [487].

10.4.1. Electron beam transport

The most promising LPA schemes in terms of electron beam quality and subsequent efficient light production [487,529] are the following ones.

Laser plasma injector and acceleration. This scheme includes two plasma stages: the laser plasma injector to produce electrons with beam energy of 150 MeV and a laser plasma acceleration stage to have particles with the final energy of 5 GeV. In particular, the beam distribution under study and denoted hereafter as **LPIA** is injected with the resonant multi-pulse ionization technique [530–532] and accelerated through a single stage in the quasi-linear regime [533,534].

Radio frequency injector and laser plasma acceleration stage. In this scheme [535], a 500 MeV electron beam is injected through a conventional radio frequency (RF) section [536] into the plasma acceleration stage which in turn accelerates the electrons up to either a beam distribution with 1 GeV [537] energy, denoted hereafter as **RILPA1**, or a beam distribution with 5 GeV energy, denoted hereafter as **RILPA5**.

These beam distributions are analyzed in terms of the main parameters driving the FEL performance. More in detail, the electron distribution slice with the highest current density [487] is identified and values of emittance, energy spread and peak current are calculated over the width of this slice in order to have reasonable performance predictions. For a quantitative comparison among the beams before any undulator matching consideration, Table 9 shows the parameter values at the plasma exit, where $\epsilon_{n,x(y)}$, $\sigma_{x(y)}$, I_{peak} and σ_ε are values of the normalized emittance in $x(y)$, the RMS beam size in $x(y)$, the peak current and the RMS energy spread calculated over the specified length of the phase space longitudinal sampling ℓ_s, reasonably chosen on the basis of the electron RMS bunch length σ_z: it results in larger than the expected SASE spike length, in each beam case. One can note that the current profile is not described with a Gaussian distribution, in any of the electron beams presented here: the width of the beam current pulse is typically shorter than σ_z.

The transfer line from the plasma exit stage, where the bunch leaves the strong focusing fields to drift into free space, is designed [538,539] such that each electron beam is properly matched to the undulator configurations to be discussed in the following section. A sketch of the transfer line from the plasma stage to the undulator entrance is shown in Fig. 28. The transfer line can be divided into three sections: a capture section, a C-chicane, and a matching section.

The capture section is made of permanent magnet quadrupoles and is designed to capture the electron beam at the plasma exit and to focus it. Most of the emittance growth occurs in this section. Careful optimization must then be performed to minimize this emittance growth. An Integrated Current Transformer (ICT) is inserted behind the capture section to measure the beam current.

Table 9
Highest current density slice values of the relevant parameters at plasma exit.

Name Unit	E [GeV]	I_{peak} [kA]	σ_ε [%]	$\epsilon_{n,x}$ [μm]	$\epsilon_{n,y}$ [μm]	σ_x [μm]	σ_y [μm]	ℓ_s [μm]
LPIA	4.98	2.93	0.11	0.53	0.59	0.87	0.92	0.11
RILPA5	5.41	2.85	0.05	0.38	0.32	1.06	0.98	1.3
RILPA1	1.09	1.88	0.92	0.4	0.41	2.2	2.2	1.2

Table 10
Matching parameters at the entrance of the undulator (undulator period: $\lambda_u = 30$ mm, module length: $L_u = 2.1$ m, distance between modules: 360 mm).

Scheme	$\langle\beta_{x,y}\rangle$ [m]	β_x [m]	β_y [m]	α_x	α_y
LPIA	5	3.07	7.45	−0.670	1.559
RILPA5	5	3.07	7.45	−0.670	1.559
RILPA1	4	2.69	5.35	−0.382	0.627

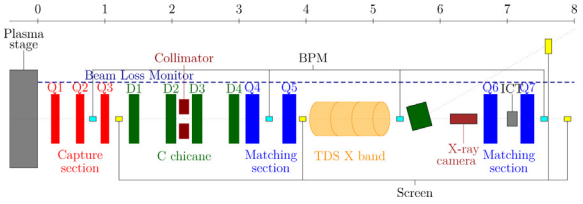

Fig. 28. Layout of the high energy beam transfer line (in red: permanent quadrupoles, in blue: electromagnet quadrupoles, in green: dipoles, in cyan: BPMs, in gray: ICT, in yellow: screens.

The C-chicane is made of 4 rectangular dipoles and is designed to separate the witness beam from the laser beam (laser plasma acceleration), or from the electron drive beam (plasma wakefield acceleration). A collimator will be used for the laser or beam driver removal in these cases. The chicane's other main purpose is to protect the undulators from possible failures at the plasma exit like too large misalignment errors or energy fluctuations (in which case the beam will then be dumped into the collimator). However, simulations are yet to be performed to validate this concept.

Finally, two doublets are used to match the beam to the undulator entrance. The two magnet pairs are separated by a distance greater than 2 meters to enable the insertion of different diagnostics: a Beam Position Monitor (BPM) to measure the beam position, an X-band Transverse Deflecting Structure (TDS) to measure the time structure [540] and a dipole to measure the energy spectrum, when needed.

One of the main features for the transport line is to retain the beam quality (and more specifically the emittance) [538]. Towards this aim, a python script has been written to match the beam to the undulator and to minimize the emittance growth along the machine (to minimize the Montague function at the undulator entrance). The matching constraints at the entrance of the undulator for the different schemes are given in Table 10. The optimization is firstly based on Particle Swarm Optimization (PSO) [541] to find initial conditions near a global minimum, secondly on conjugate gradient method [542] to speed up the convergence near a minimum, and finally with a tracking code, like TraceWin [543], elegant [523] or ASTRA [544]. The variables are the quadrupole gradients and the position of the different elements. The constraints are the total length of the machine (8 m in our case), minimum and maximum gradients (500 T/m for permanent quadrupoles and 50 T/m for electromagnet quadrupoles), the minimum distance between elements (30 mm between permanent quadrupoles, and 300 mm between electromagnet quadrupoles of the same doublet to insert BPMs and correctors in between, 2 m between permanent quadrupoles and electromagnet quadrupoles to insert a C-chicane in between, and 2.5 m between both doublets to insert long diagnostics like the TDS or a spectrometer). Finally, the beam transfer line is optimized with the tracking code TraceWin [543] to match the beam to the undulator entrance and to minimize the emittance growth. This optimization takes into account the entire beam distribution with no assumptions on the initial conditions.

As an example, the evolution of the beam distribution along the transport line is shown in Fig. 29 for the case **A**. The evolution of the slice properties along the longitudinal beam distribution are shown in Fig. 30. Beam properties are well preserved along the transfer line. The parameters of the quadrupoles are summarized in Table 11 and the final beam characteristics are presented in Table 10. The associated results assume values for both magnetic field and K_u deflection parameter that are feasible with the technologies presented in the previous Sections: namely either a cryogenic permanent magnet undulator (CPMU) or a superconducting undulator (SCU), assuming any beam stay clear gap larger than 6 mm. For example, from recent CPMU parameterizations, a beam stay clear gap of about 8 mm together with a period of 20 mm allow the values shown in Table 11.

Table 11
Parameters of the focusing elements in the transport line to the undulator for the case **LPIA**.

Quadrupole		Q1	Q2	Q3	Q4	Q5	Q6	Q7
Length	[mm]	100			200			
Gradient	[T/m]	−347	471	−297	1.18	22.7	−39.5	−25.4

Table 12
Undulator configurations used for the FEL environment.

E [GeV]	λ_R [nm]	λ_u [mm]	K_u	B_u [T]
5	0.22	20	1.5	0.81
5	1.65	30	4.36	1.56
1	5.5	20	1.5	0.81
1	41	30	4.36	1.56

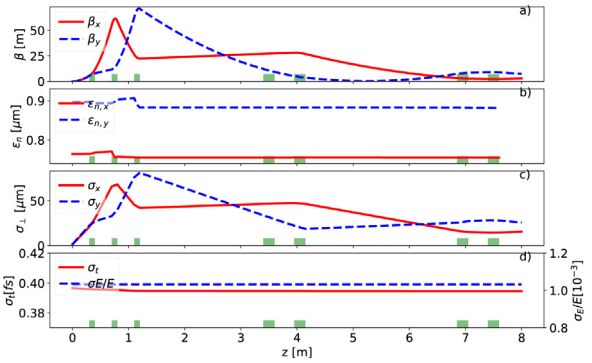

Fig. 29. Beam beta function (a), normalized emittance (b), transverse size (c), bunch duration and energy spread (d) of the core beam along the transport line for the case **LPIA**. Calculations were performed with the tracking code TraceWin.

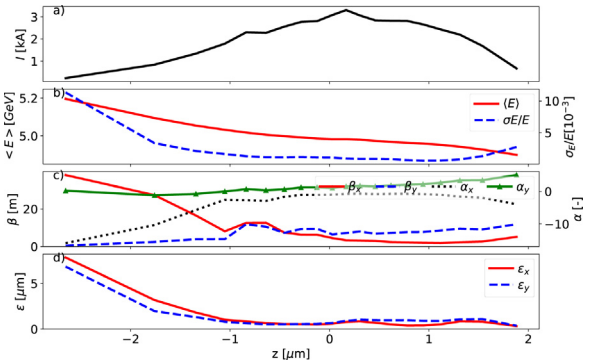

Fig. 30. Profile of the slice current (a), mean slice energy and slice energy spread (b), slice Twiss parameters (c) and normalized slice emittance (d) along the beam length at the entrance of the undulator for the case **LPIA**. Calculations were performed with the tracking code ASTRA. The slice length is 0.1 μm.

10.4.2. Undulator line characteristics

Each previously discussed beam distribution is analyzed and matched to two different undulator configurations [545, 546], in order to probe the beam phase space features with two different cooperation lengths: one targeting $\lambda_R \simeq 0.2$ nm with 5 GeV beam energy, and within present and near future undulator technology [449,547] and the other such that $L_c/\sigma_z \sim 1\%$ at $E = 5$ GeV and $L_c/\sigma_z \sim 10\%$ at $E = 1$ GeV.

Table 12 shows the features of the chosen undulator configurations. These parameters are within the capabilities of both superconducting and cryogenic permanent magnet devices, with no need to shrink the undulator gap to 6 mm or less, so that the FEL dynamics in these devices is less affected by wakefield effects. These effects have been neglected in the following calculations. Room temperature undulators provide weaker B_u and K_u values with undulator gap larger than 6 mm, so they are not considered.

Table 13
Best slice values of the relevant parameters at undulator entrance and of the expected cooperation lengths, at the specified undulator configurations.

Name		LPIA	RILPA5	RILPA1
E	[GeV]	4.96	5.41	1.09
I_{peak}	[kA]	2.63	2.74	1.75
σ_ε	[%]	0.052	0.052	0.103
$\langle\epsilon_n\rangle$	[μm]	0.58	0.34	0.44
$\langle\beta\rangle$	[m]	5	5	4
L_c^{U2}	[nm]	20	14	140
L_c^{U3}	[nm]	61	42	430

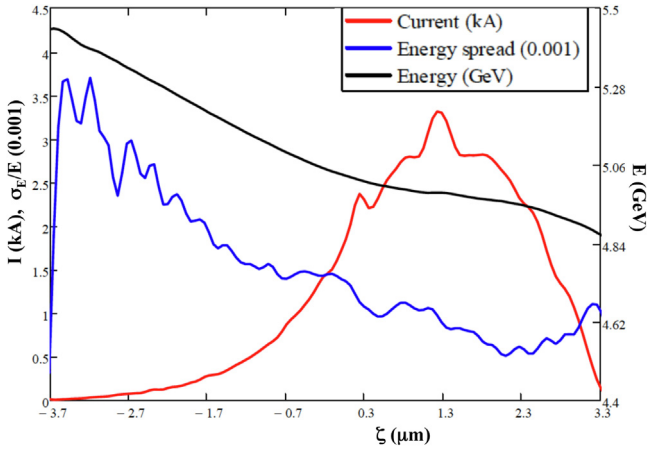

Fig. 31. Energy, current and energy spread slice profiles as a function of the intrabunch ζ coordinate, for the case **B** beam distribution at the undulator entrance.

At both 1 GeV and 5 GeV energies, the natural focusing of the undulator is rather weak. In order to maintain a small transverse size of the electron beam, the periodic magnetic cell has to include alternate gradient quadrupoles in between undulator modules.

The strategy to match the beams is based on minimizing the difference between average Twiss β values, $\left|\langle\beta_x\rangle - \langle\beta_y\rangle\right|$, also featuring reasonable magnetic gradients, for both the short and the long λ_u configurations. The undulator period and strength clearly define the Twiss α and β parameter values that the electron beams should have at the undulator entrance, in order to be correctly matched.

10.4.3. FEL results

After proper transport of the beams through the undulator entrance, the distribution slice with the lowest $(\sigma_\varepsilon)/\rho$ ratio is identified as the best slice in terms of FEL performance. Table 13 shows the main parameters associated to this slice, within a sampling interval ℓ_s along the bunch, as previously defined and shown on the last row of Table 9, for each beam. In particular, $\langle\beta\rangle$ refers to a nominal average Twiss β value along the full undulator section and $\langle\epsilon_n\rangle$ is the normalized emittance, averaged along the bunch. For every beam distribution, the best slice has an emittance value smaller than $\langle\epsilon_n\rangle$: for a more conservative estimate, the average emittance is considered. Symmetry in x and y coordinates is assumed for both $\langle\beta\rangle$ and $\langle\epsilon_n\rangle$.

Compared to the parameters presented in Table 9, these values refer to a different phase space region, optimized also taking energy spread into account. Moreover, space charge effects induce a non-negligible coupling between longitudinal and transverse planes, resulting in a net bunch decompression for each beam distribution.

Table 13 also shows the cooperation length values expected when matching the electron beams either to the short, L_c^{U2} with $\lambda_u = 2$ cm, or to the long, L_c^{U3} with $\lambda_u = 3$ cm, undulator period configuration.

The SASE FEL performance is evaluated with the PERSEO simulation code [548], that allows to perform a full time-dependent simulation of the FEL dynamics taking account of the given longitudinal current, energy and energy spread profiles and of their interplay along the bunch. The transverse plane dynamic effects are accounted for via a 3D coupling factor derived from the Ming–Xie relations [314]. Moreover, the time-dependent analysis allows a reliable estimate of the FEL pulse duration and spectral line width.

Fig. 31 shows the longitudinal slice profiles of energy, current, energy spread and normalized emittance of the case **RILPA5** beam distribution, as an example.

Table 14
Short and long undulator period results of the time-dependent simulations with longitudinal dynamics description, obtained with PERSEO.

Name		LPIA	RILPA5	RILPA1
Short undulator period				
Saturation length	[m]	126	38	28
Linewidth	[%]	0.18	0.23	0.25
Pulse duration	[fs]	0.4	2	2.4
Photons per pulse	[10^{10}]	0.19	3.2	2.3
Long undulator period				
Saturation length	[m]	26	20	16
Linewidth	[%]	0.3	0.3	0.54
Pulse duration	[fs]	0.71	2.2	7.8
Photons per pulse	[10^{10}]	4.2	72	31

The results of the time-dependent simulations obtained accounting for the proper longitudinal dynamics of each beam distribution are shown in Table 14 for the short and the long undulator period configuration. Comparing the two cases **LPIA** and **RILPA5**, the different values of the energy spread distributions explain the differences in saturation length and in the number of photons per pulse. Larger undulator period and strength yield a significantly larger Pierce ρ parameter in each beam distribution. The effective result is a significantly better FEL performance in saturation length and photons per pulse, but at the same time the resulting longer cooperation length affects the results in terms of spectral and temporal behavior. Within this configuration, cases **LPIA** and **RILPA5** have comparable saturation lengths, but the different beam quality results in a different performance in terms of photons per pulse, at saturation.

11. Conclusion

We have underscored that high brightness is the beam quality of crucial interest to realize a successful FEL. Technologies based on "ordinary" accelerating cavities have provided beams with extremely good qualities, namely small six dimensional phase space and large charge that have delivered high brightness X-ray beams with tailor-suited properties to explore nano-ultra fast world. These light sources can be viewed as "a gigantic flash camera" allowing to peek inside matter as never done [269]. The limit of new materials with large breakdown threshold (say 1 GeV/m) are therefore the natural candidate for a revolution bringing X-ray FEL to a more reasonable dimension.

Albeit this material has not yet been discovered, the development of high power laser thanks to the chirped pulse amplification, recognized by a Nobel Prize in 2018 [549], enabled the laser plasma acceleration to significantly progress all around the world in terms of electron beam characteristics. This mechanism offers the hope for reaching high electron energies within a small acceleration length with intrinsic focusing, and some hopes on this arising new concept are conveyed for future colliders. Although significant improvements are necessary to get an LPA FEL suited beam (in terms of energy, brightness, repetition rate and stability), it is worth to provide a first example of LPA produced light in order to define an operational protocol. Still, not all the interesting features are being produced simultaneously and not yet in a very regular basis, and different LPA configuration suit better for improving one particular feature. Overall, some of the performance do not reach the ones currently achieved by up to date state-of-the-art conventional accelerators, and it appears reasonable to target the Free Electron Laser application as being more within reach than the collider one. One of the attracting features of the these electron beam is for instance, the shot electron bunch duration, that would lead to single spike FEL. With the new paradigm of LPA electron beam characteristics, we have examined here what FEL gain configuration should be used in terms of undulator choice, especially in view of the short bunches that should not make the slippage dominant.

After recalling the process, performance and scaling laws of LPA and FELs, issues on electron beam matching to the undulator, we have analyzed the recent development on undulator technology that could be of interest of the LPA based FEL application. Aiming at minimizing also the gain section of the LPA based FEL, we have found that, with respect to [95], the recent progresses of short period high field undulators with cryogenic or superconducting technology are well adapted in such a case, and analytic scaling have also being provided. In addition, the developments of transverse gradient undulators are also very attractive, for being able to insure a proper strategy to mitigate the relatively large energy spread of LPA. In the last sections, the present expectations of LPA based FEL results are reviewed, both for present test experiments using available electron beam performance, and with optimized ones as studied in the frame of the EuPRAXIA collaboration. A first very recent demonstration of the LPA based FEL using high quality electron beam [94], with a two orders of magnitude amplification, is a major step towards the achievement of these new single spike compact FELs. Further progress will result from jointed effort of the LPA development for improved electron beam features and FEL and undulator design, including the transport manipulation line to the undulator. It will pave the way of multi-color, short pulses, broad bandwidth FELs of a new type.

CRediT authorship contribution statement

A. Ghaith: Conceptualization, Data curation, Formal analysis, Methodology, Supervision, Validation, Visualization, Roles/Writing – original draft, Writing – review & editing, Software. **M.-E. Couprie:** Conceptualization, Data curation, Funding acquisition, Project administration, Supervision, Validation, Roles/Writing – original draft, Writing – review & editing. **D. Oumbarek-Espinos:** Resources. **I.A. Andriyash:** Formal analysis, Methodology, Supervision, Roles/Writing – original draft, Writing – review & editing. **F. Massimo:** Formal analysis, Resources, Roles/Writing – original draft, Investigation, Visualization, Software. **J.A. Clarke:** Resources, Roles/Writing – original draft, Visualization. **M. Courthold:** Roles/Writing – original draft, Visualization. **V. Bayliss:** Roles/Writing – original draft, Visualization. **A. Bernhard:** Roles/Writing – original draft, Visualization. **M. Trunk:** Roles/Writing – original draft. **M. Valléau:** Formal analysis, Resources. **O. Marcouillé:** Formal analysis, Resources. **A. Chancé:** Roles/Writing – original draft, Resources. **S. Licciardi:** Roles/Writing – original draft, Visualization. **V. Malka:** Validation. **F. Nguyen:** Roles/Writing – original draft, Visualization, Software. **G. Dattoli:** Conceptualization, Data curation, Formal analysis, Investigation, Methodology, Supervision, Validation, Roles/Writing – original draft, Writing – review & editing, Software.

Declaration of competing interest

The authors declare that they have no known competing financial interests or personal relationships that could have appeared to influence the work reported in this paper.

Acknowledgments

The authors acknowledge the support by the European Unions Horizon 2020 research and innovation program under grant agreement EuPRAXIA No. 653782 led by R. Assman, COXINEL ERC project, contract 340015 and X-Five ERC project, contract No. 339128. The authors also thank A. Curcio for fruitful discussions.

Numerical simulations in the LPA section were performed using HPC resources from GENCI-TGCC (Grand Équipement National De Calcul Intensif, France) (Grant No. 2020-A0090510062) with the IRENE supercomputer.

This work was granted access to the HPC resources of TGCC under the allocation 2017 - A0010510062 made by GENCI, France.

Appendix. List of notation

A.1. Physical constants

$m_e = 9.109382 \times 10^{-31}$ kg
$c = 2.99792458 \times 10^{8}$ m/s
$e = 1.60217646 \times 10^{-19}$ C
1 eV $= 1.60217646 \times 10^{-19}$ J
$m_e c^2 = 0.5109989$ MeV
Z_0 (free space impedance) $= \mu_0 c = 376.73\ \Omega$
$I_A = \frac{4\pi}{Z_0 c}\frac{m_e c^3}{e} = 1.704509 \times 10^4$ A Alfvén current
$\epsilon_0 = 8.85418782 \times 10^{-12}$ m^{-3} kg^{-1} s^4 A^2

A.2. Undulator parameters

λ_u: Undulator period
$k_u = \frac{2\pi}{\lambda_u}$: Undulator wave number
B_u: Undulator magnetic peak field
N_u: Number of undulator periods
$L_u = N_u \lambda_u$: Undulator length
$K_u = \frac{eB_u\lambda_u}{2\pi m_e c^2} = 93.4\lambda_u$ [m] B_u [T]: Deflection parameter
$f_b = J_0(\zeta) - J_1(\zeta)$: Linear undulator ($J_{0,1}$ cylindrical Bessel function)
$\zeta = \frac{1}{4}\frac{K_u^2}{1+K^2/2}$
$B_u = 2B_r \frac{\sin(\pi/M)}{\pi/M}\left[(1 - \exp(-2\pi h/\lambda_u))\exp(-\pi g/\lambda_u)\right]$: Halbach configuration undulator peak field
M: Number of blocks per period
h: Magnet height
g: Undulator gap
B_r: Remanent field
λ_r: Resonant wavelength
ω_r: Resonant frequency
$[\Delta_\omega]_n$: Natural linewidth
$[\Delta_\omega]_i$: Inhomogeneous broadening

A.3. Electron beam parameters

E: Energy
$\gamma = \frac{E}{m_e c^2}$: Relativistic factor
$\Phi(\epsilon) = \frac{1}{\sqrt{2\pi}\sigma_\epsilon} \exp\left(-\frac{\epsilon^2}{2\sigma_\epsilon^2}\right)$: Relative energy distribution
$\sigma_\epsilon = \frac{\gamma - \gamma_0}{\gamma_0}$: Energy spread
$\mu_\epsilon = 4N_u\sigma_\epsilon$: Energy distribution inhomogeneous broadening parameter
$F(x, x', y, y') = W(x, x')W(y, y')$: Distribution function
$\eta \equiv x, y$: Transverse Coordinates
$W(\eta, \eta') = \frac{1}{2\pi\epsilon_n} \exp\left[-\frac{1}{2\epsilon_n}\left(\beta_n\eta'^2 + 2\alpha_n\eta\eta' + \gamma_n\eta^2\right)\right]$
ϵ_n: Emittance in the (η, η') plane
$\alpha_n, \beta_n, \gamma_n$: Twiss coefficients with $\beta_n\gamma_n - \alpha_n^2 = 1$
$\mu_{\eta'} = \frac{4N_u\gamma^2\epsilon_n}{(1+K*^2)\beta_n}$
$\mu_\eta = \frac{4N_u\gamma^2\epsilon_n}{(1+K*^2)\gamma_n}k_\beta^2$
$k_\beta = \frac{K_u k_u}{2\gamma}$: Betatron motion wave number
$\mu_\eta, \mu_{\eta'}$: Emittance inhomogeneous parameters
$\sigma_\eta = \sqrt{\beta_n\epsilon_n}$: Beam section
$\sigma_{\eta'} = \sqrt{\gamma_n\epsilon_n}$: Beam divergence
σ_τ: Bunch time duration
Q_b: Bunch charge
$I = \frac{Q_b}{\sqrt{2\pi}\sigma_\tau}$: Peak current
$J = \frac{I}{2\pi\sigma_x\sigma_y}$: Current density

A.4. FEL parameters

P_E: Electron beam power
L_g: Gain length
L_s: Saturation length
ρ: Pierce parameter
ζ: Electron field variable
$f_b(\zeta)$: gain Bessel factor corrections
g_0: Growth power
G: Gain
P_s: Saturation power

A.5. LPA parameters

r_e: Classical electron radius
p_e: Electron fluid momentum
$\mathbf{j}$: Current density
v_{ph}: Phase velocity
v_g: Group velocity
$\mathbf{F}_p$: Pondermotive force
F_r: Transverse force acting on the particles in the bubble
a_l: vector potential
n_e: Electron density
n_p: Plasma density
n_i: Ion density
ω_p: Plasma frequency
k_p: wavenumber of the relativistic plasma wave
ϕ: Electrostatic potential
Φ: scalar pseudo-potential
τ_l: Laser pulse duration
ω_0: Laser waist
a_0: Pulse amplitude
P: Power
P_r: relativistic power
n_c: Critical plasma density

W_e: Energy gained by electrons
L_{deph}: Length depletion
R: Radius of the bubble

References

[1] A.L. Schawlow, C.H. Townes, Infrared and optical masers, Phys. Rev. 112 (6) (1958) 1940.
[2] J. van Vleck, The absorption of radiation by multiply periodic orbits, and its relation to the correspondence principle and the Rayleigh-jeans law. Part i. some extensions of the correspondence principle, Phys. Rev. 24 (1924) 330–346, http://dx.doi.org/10.1103/PhysRev.24.330, URL http://link.aps.org/doi/10.1103/PhysRev.24.330.
[3] J. Van Vleck, D. Huber, Absorption, emission, and linebreadths: A semihistorical perspective, Rev. Modern Phys. 49 (1977) 939–959, http://dx.doi.org/10.1103/RevModPhys.49.939, URL http://link.aps.org/doi/10.1103/RevModPhys.49.939.
[4] R.G. Gould, The LASER, light amplification by stimulated emission of radiation, in: The Ann Arbor Conference on Optical Pumping, the University of Michigan, vol. 15, 1959, pp. 128.
[5] M. Planck, über eine verbesserung der wienschen spektralgleichung, in: Von Kirchhoff Bis Planck, Springer, 1978, pp. 175–178.
[6] M.K.E.L. Planck, Zur theorie des gesetzes der energieverteilung im normalspectrum, Verhandl. Dtsc. Phys. Ges. 2 (1900) 237.
[7] M. Planck, On an improvement of wien's equation for the spectrum, Verh. Deut. Phys. Ges 2 (1900) 202–204.
[8] M. Planck, On the theory of the energy distribution law of the normal spectrum, Verh. Deut. Phys. Ges 2 (1900) 237–245.
[9] A. Einstein, Zur quantentheorie der strahlung, Phys. Z. 18 (1917) 124.
[10] J.P. Gordon, H.J. Zeiger, C.H. Townes, Molecular microwave oscillator and new hyperfine structure in the microwave spectrum of NH_3, Phys. Rev. 95 (1) (1954) 282.
[11] T. Maimain, Stimulated optical radiation in ruby, Nature 187 (1960) 493–494.
[12] T.H. Maiman, R. Hoskins, I. d'Haenens, C.K. Asawa, V. Evtuhov, Stimulated optical emission in fluorescent solids. II. Spectroscopy and stimulated emission in ruby, Phys. Rev. 123 (4) (1961) 1151.
[13] A. Javan, J. Bennett, R. William, D.R. Herriott, Population inversion and continuous optical maser oscillation in a gas discharge containing a he-ne mixture, Phys. Rev. Lett. 6 (3) (1961) 106.
[14] R.N. Hall, G.E. Fenner, J. Kingsley, T. Soltys, R. Carlson, Coherent light emission from GaAs junctions, Phys. Rev. Lett. 9 (9) (1962) 366.
[15] R. Keyes, T. Quist, Recombination radiation emitted by gallium arsenide, Proc. Inst. Electron. Radio Eng. 50 (8) (1962) 1822.
[16] J.M. Madey, Stimulated emission of bremsstrahlung in a periodic magnetic field, J. Appl. Phys. 42 (5) (1971) 1906–1913.
[17] T. Tajima, J. Dawson, Laser electron accelerator, Phys. Rev. Lett. 43 (1979) 267–270, http://dx.doi.org/10.1103/PhysRevLett.43.267, URL http://link.aps.org/doi/10.1103/PhysRevLett.43.267.
[18] G. Dattoli, E. Di Palma, S. Pagnutti, E. Sabia, Free electron coherent sources: From microwave to X-rays, Phys. Rep. 739 (2018) 1–51.
[19] R.H. Varian, S.F. Varian, A high frequency oscillator and amplifier, J. Appl. Phys. 10 (5) (1939) 321–327.
[20] W. Colson, Theory of a free electron laser, Phys. Lett. A 59 (3) (1976) 187–190.
[21] Z. Huang, K.-J. Kim, Review of X-ray free-electron laser theory, Phys. Rev. Special Topics Accelerators Beams 10 (3) (2007) 034801.
[22] C. Pellegrini, A. Marinelli, S. Reiche, The physics of X-ray free-electron lasers, Rev. Modern Phys. 88 (1) (2016) 015006.
[23] G. Dattoli, M. Del Franco, M. Labat, P. Ottaviani, S. Pagnutti, Introduction to the physics of free electron laser and comparison with conventional laser sources, Free Electron Lasers (2012) 1.
[24] M.-E. Couprie, Historical survey of free electron lasers, CERN Yellow Rep. Sch. Proc. 1 (2018) 195.
[25] M. Couprie, Panorama of new generation of accelerator based short wavelength coherent light sources, Nucl. Instrum. Methods Phys. Res. B 364 (2015) 4–15.
[26] A. Kondratenko, Sou phys. Dokl, Part. Accelerators 24 (1979) 12.
[27] A. Kondratenko, E. Saldin, Generation of coherent radiation by a relativistic-electron beam in an undulator, in: Particle Accelerator Conference, vol. 10, 1980, pp. 207–216.
[28] H. Haus, Noise in free-electron laser amplifier, IEEE J. Quantum Electron. 17 (8) (1981) 1427–1435.
[29] G. Dattoli, A. Marino, A. Renieri, F. Romanelli, Progress in the Hamiltonian picture of the free-electron laser, IEEE J. Quantum Electron. 17 (1981) 1371–1387.
[30] R. Bonifacio, C. Pellegrini, L. Narducci, Collective instabilities and high-gain regime in a free electron laser, Opt. Commun. 50 (6) (1984) 373–378.
[31] K.-J. Kim, An analysis of self-amplified spontaneous emission, Nucl. Instrum. Methods Phys. Res. A 250 (1–2) (1986) 396–403.
[32] H.N. Chapman, A. Barty, M.J. Bogan, S. Boutet, M. Frank, S.P. Hau-Riege, S. Marchesini, B.W. Woods, S. Bajt, W.H. Benner, et al., Femtosecond diffractive imaging with a soft-X-ray free-electron laser, Nat. Phys. 2 (12) (2006) 839.
[33] R. Mitzner, J. Rehanek, J. Kern, S. Gul, J. Hattne, T. Taguchi, R. Alonso-Mori, R. Tran, C. Weniger, H. Schröder, et al., L-edge X-ray absorption spectroscopy of dilute systems relevant to metalloproteins using an X-ray free-electron laser, J. Phys. Chem. Lett. 4 (21) (2013) 3641–3647.
[34] M.E. Couprie, New generation of light sources: present and future, J. Electron Spectrosc. Relat. Phenom. 196 (2014) 3–13.
[35] M. Couprie, M. Velghe, R. Prazeres, D. Jaroszynski, M. Billardon, Results and analysis of free-electron-laser oscillation in a high-energy storage ring, Phys. Rev. A 44 (2) (1991) 1301.
[36] E.B. Szarmes, A.D. Madden, J.M. Madey, Observation and characterization of frequency-chirped optical pulses on the mark III free-electron laser, Nucl. Instrum. Methods Phys. Res. A 358 (1) (1995) 220–223.
[37] T. Hara, M. Couprie, M. Billardon, Temporal and spectral evolution of a storage ring FEL source: experimental results on super-ACO and new theoretical approach, Nucl. Instrum. Methods Phys. Res. A 375 (1) (1996) 67–70.
[38] F. Glotin, R. Chaput, D. Jaroszynski, R. Prazeres, J.-M. Ortega, Infrared subpicosecond laser pulses with a free-electron laser, Phys. Rev. Lett. 71 (16) (1993) 2587.
[39] E. Prat, S. Reiche, Simple method to generate terawatt-attosecond X-ray free-electron-laser pulses, Phys. Rev. Lett. 114 (24) (2015) 244801.
[40] A. Lutman, R. Coffee, Y. Ding, Z. Huang, J. Krzywinski, T. Maxwell, M. Messerschmidt, H.-D. Nuhn, Experimental demonstration of femtosecond two-color X-ray free-electron lasers, Phys. Rev. Lett. 110 (13) (2013) 134801.
[41] A. Marinelli, A. Lutman, J. Wu, Y. Ding, J. Krzywinski, H.-D. Nuhn, Y. Feng, R. Coffee, C. Pellegrini, Multicolor operation and spectral control in a gain-modulated X-ray free-electron laser, Phys. Rev. Lett. 111 (13) (2013) 134801.
[42] T. Hara, Y. Inubushi, T. Katayama, T. Sato, H. Tanaka, T. Tanaka, T. Togashi, K. Togawa, K. Tono, M. Yabashi, et al., Two-colour hard X-ray free-electron laser with wide tunability, Nature Commun. 4 (2013) ncomms3919.
[43] A. Marinelli, D. Ratner, A. Lutman, J. Turner, J. Welch, F.-J. Decker, H. Loos, C. Behrens, S. Gilevich, A. Miahnahri, et al., High-intensity double-pulse X-ray free-electron laser, Nature Commun. 6 (2015) 6369.
[44] E. Allaria, D. Castronovo, P. Cinquegrana, P. Craievich, M. Dal Forno, M. Danailov, G. D'Auria, A. Demidovich, G. De Ninno, S. Di Mitri, et al., Two-stage seeded soft-X-ray free-electron laser, Nat. Photonics 7 (11) (2013) 913–918.

[45] A. Petralia, M. Anania, M. Artioli, A. Bacci, M. Bellaveglia, M. Carpanese, E. Chiadroni, A. Cianchi, F. Ciocci, G. Dattoli, et al., Two-color radiation generated in a seeded free-electron laser with two electron beams, Phys. Rev. Lett. 115 (1) (2015) 014801.
[46] E. Ferrari, E. Allaria, J. Buck, G. De Ninno, B. Diviacco, D. Gauthier, L. Giannessi, L. Glaser, Z. Huang, M. Ilchen, et al., Single shot polarization characterization of XUV fel pulses from crossed polarized undulators, Sci. Rep. 5 (2015) 13531.
[47] A.A. Lutman, J.P. MacArthur, M. Ilchen, A.O. Lindahl, J. Buck, R.N. Coffee, G.L. Dakovski, L. Dammann, Y. Ding, H.A. Dürr, et al., Polarization control in an X-ray free-electron laser, Nat. Photonics 10 (7) (2016) 468.
[48] A. Marinelli, J. MacArthur, P. Emma, M. Guetg, C. Field, D. Kharakh, A. Lutman, Y. Ding, Z. Huang, Experimental demonstration of a single-spike hard-X-ray free-electron laser starting from noise, Appl. Phys. Lett. 111 (15) (2017) 151101.
[49] N. Hartmann, G. Hartmann, R. Heider, M. Wagner, M. Ilchen, J. Buck, A. Lindahl, C. Benko, J. Grünert, J. Krzywinski, et al., Attosecond time–energy structure of X-ray free-electron laser pulses, Nat. Photonics 12 (4) (2018) 215.
[50] J. Duris, S. Li, T. Driver, E.G. Champenois, J.P. MacArthur, A.A. Lutman, Z. Zhang, P. Rosenberger, J.W. Aldrich, R. Coffee, et al., Tunable isolated attosecond X-ray pulses with gigawatt peak power from a free-electron laser, Nat. Photonics 14 (1) (2020) 30–36.
[51] D. Strickland, G. Mourou, Compression of amplified chirped optical pulses, Opt. Commun. 55 (6) (1985) 447–449.
[52] V. Malka, J. Faure, Y.A. Gauduel, E. Lefebvre, A. Rousse, K.T. Phuoc, Principles and applications of compact laser–plasma accelerators, Nat. Phys. 4 (6) (2008) 447–453.
[53] E. Esarey, C. Schroeder, W. Leemans, Physics of laser-driven plasma-based electron accelerators, Rev. Modern Phys. 81 (2009) 1229–1285, http://dx.doi.org/10.1103/RevModPhys.81.1229, URL http://link.aps.org/doi/10.1103/RevModPhys.81.1229.
[54] C. Geddes, C. Toth, J. Van Tilborg, E. Esarey, C. Schroeder, D. Bruhwiler, C. Nieter, J. Cary, W. Leemans, High-quality electron beams from a laser wakefield accelerator using plasma-channel guiding, Nature 431 (7008) (2004) 538–541.
[55] J. Faure, Y. Glinec, A. Pukhov, S. Kiselev, S. Gordienko, E. Lefebvre, J. Rousseau, F. Burgy, V. Malka, A laser-plasma accelerator producing monoenergetic electron beams, Nature 431 (2004) 541–544.
[56] S. Mangles, C. Murphy, Z. Najmudin, A. Thomas, J. Collier, A. Dangor, E. Divall, P. Foster, J. Gallacher, C. Hooker, D. Jaroszynski, A. Langley, W. Mori, P. Norreys, F. Tsung, R. Viskup, B. Walton, K. Krushelnick, Monoenergetic beams of relativistic electrons from intense laser-plasma interactions, Nature 431 (2004) 538–541.
[57] V. Malka, J. Faure, Y. Glinec, A. Pukhov, J.-P. Rousseau, Monoenergetic electron beam optimization in the bubble regime, Phys. Plasmas 12 (5) (2005) 56702–56709.
[58] W. Leemans, B. Nagler, A. Gonsalves, C. Toth, K. Nakamura, C. Geddes, E. Esarey, C. Schroeder, S. Hooker, Gev electron beams from a centimetre-scale accelerator, Nat. Phys. 2 (10) (2006) 696–699.
[59] A. Gonsalves, K. Nakamura, J. Daniels, C. Benedetti, C. Pieronek, T. De Raadt, S. Steinke, J. Bin, S. Bulanov, J. Van Tilborg, et al., Petawatt laser guiding and electron beam acceleration to 8 GeV in a laser-heated capillary discharge waveguide, Phys. Rev. Lett. 122 (8) (2019) 084801.
[60] O. Lundh, J. Lim, C. Rechatin, L. Ammoura, A. Ben-Ismail, X. Davoine, G. Gallot, J.-P. Goddet, E. Lefebvre, V. Malka, J. Faure, Few femtosecond, few kiloampere electron bunch produced by a laser-plasma accelerator, Nat. Phys. 7 (3) (2011) 219–222.
[61] J. Couperus, R. Pausch, A. Köhler, O. Zarini, J. Krämer, M. Garten, A. Huebl, R. Gebhardt, U. Helbig, S. Bock, et al., Demonstration of a beam loaded nanocoulomb-class laser wakefield accelerator, Nature Commun. 8 (1) (2017) 1–7.
[62] A. Döpp, C. Thaury, E. Guillaume, F. Massimo, A. Lifschitz, I. Andriyash, J.-P. Goddet, A. Tazfi, K. Ta Phuoc, V. Malka, Energy-chirp compensation in a laser wakefield accelerator, Phys. Rev. Lett. 121 (2018) 074802, http://dx.doi.org/10.1103/PhysRevLett.121.074802, URL https://link.aps.org/doi/10.1103/PhysRevLett.121.074802.
[63] A. Martinez de la Ossa, R. Assmann, M. Bussmann, S. Corde, J. Couperus Cabadağ, A. Debus, A. Döpp, A. Ferran Pousa, M. Gilljohann, T. Heinemann, et al., Hybrid LWFA–PWFA staging as a beam energy and brightness transformer: conceptual design and simulations, Phil. Trans. R. Soc. A 377 (2151) (2019) 20180175.
[64] P. Chen, J. Dawson, R.W. Huff, T. Katsouleas, Acceleration of electrons by the interaction of a bunched electron beam with a plasma, Phys. Rev. Lett. 54 (7) (1985) 693.
[65] M. Litos, E. Adli, W. An, C. Clarke, C. Clayton, S. Corde, J. Delahaye, R. England, A. Fisher, J. Frederico, et al., High-efficiency acceleration of an electron beam in a plasma wakefield accelerator, Nature 515 (7525) (2014) 92–95.
[66] E. Esarey, P. Sprangle, J. Krall, A. Ting, Overview of plasma-based accelerator concepts, IEEE Trans. Plasma Sci. 24 (2) (1996) 252–288.
[67] W. Lu, C. Huang, M. Zhou, M. Tzoufras, F. Tsung, W.B. Mori, T. Katsouleas, A nonlinear theory for multidimensional relativistic plasma wave wakefields, Phys. Plasmas 13 (5) (2006) 056709, http://dx.doi.org/10.1063/1.2203364.
[68] B. Hidding, A. Beaton, L. Boulton, S. Corde, A. Doepp, F.A. Habib, T. Heinemann, A. Irman, S. Karsch, G. Kirwan, et al., Fundamentals and applications of hybrid lwfa-pwfa, Appl. Sci. 9 (13) (2019) 2626.
[69] P. Baxevanis, Z. Huang, Multipole Field Effects in a Transverse Gradient Undulator, in: Proceedings of IPAC2017, Copenhagen, Denmark, 2017.
[70] F. Grüner, S. Becker, U. Schramm, T. Eichner, M. Fuchs, R. Weingartner, D. Habs, J. Meyer-ter Vehn, M. Geissler, M. Ferrario, et al., Design considerations for table-top, laser-based VUV and X-ray free electron lasers, Appl. Phys. B 86 (3) (2007) 431–435.
[71] K. Nakajima, Compact X-ray sources: Towards a table-top free-electron laser, Nat. Phys. 4 (2) (2008) 92–93.
[72] M. Couprie, M. Labat, C. Evain, C. Szwaj, S. Bielawski, N. Hubert, C. Benabderrahmane, F. Briquez, L. Chapuis, F. Marteau, et al., Strategies towards a compact XUV free electron laser adopted for the LUNEX5 project, J. Modern Opt. 63 (4) (2016) 309–323.
[73] M.-E. Couprie, A. Loulergue, M. Labat, R. Lehe, V. Malka, Towards a free electron laser based on laser plasma accelerators, J. Phys. B: At. Mol. Opt. Phys. 47 (23) (2014) 234001.
[74] H.-P. Schlenvoigt, K. Haupt, A. Debus, F. Budde, O. Jäckel, S. Pfotenhauer, H. Schwoerer, E. Rohwer, J. Gallacher, E. Brunetti, et al., A compact synchrotron radiation source driven by a laser-plasma wakefield accelerator, Nat. Phys. 4 (2) (2008) 130.
[75] M. Fuchs, R. Weingartner, A. Popp, Z. Major, S. Becker, J. Osterhoff, I. Cortrie, B. Zeitler, R. Hörlein, G.D. Tsakiris, et al., Laser-driven soft-X-ray undulator source, Nat. Phys. 5 (11) (2009) 826.
[76] M.P. Anania, E. Brunetti, S. Wiggins, D.W. Grant, G.H. Welsh, R. Issac, S. Cipiccia, R. Shanks, G. Manahan, C. Aniculaesei, et al., An ultrashort pulse ultra-violet radiation undulator source driven by a laser plasma wakefield accelerator, Appl. Phys. Lett. 104 (26) (2014) 264102.
[77] G. Lambert, S. Corde, K.T. Phuoc, V. Malka, A.B. Ismail, E. Benveniste, A. Specka, M. Labat, A. Loulergue, R. Bachelard, et al., Progress on the generation of undulator radiation in the UV from a plasma-based electron beam, in: Proceed. FEL Conf., Nara, Japan, 2012, p. 2.
[78] T. André, I. Andriyash, A. Loulergue, M. Labat, E. Roussel, A. Ghaith, M. Khojoyan, C. Thaury, M. Valléau, F. Briquez, F. Marteau, K. Tavakoli, P. N'Gotta, Y. Dietrich, G. Lambert, V. Malka, C. Benabderrahmane, J. Vétéran, L. Chapuis, T. El Ajjouri, M. Sebdaoui, N. Hubert, O. Marcouillé, P. Berteaud, N. Leclercq, M. El Ajjouri, P. Rommeluère, F. Bouvet, J. Duval, C. Kitegi, F. Blache, B. Mahieu, S. Corde, J. Gautier, K. Ta Phuoc, J. Goddet, A. Lestrade, C. Herbeaux, C. Evain, C. Szwaj, S. Bielawski, A. Tafzi, P. Rousseau, S. Smartsev, F. Polack, D. Dennetière, C. Bourassin-Bouchet, C. De Oliveira, M. Couprie, Control of laser plasma accelerated electrons for light sources, Nature Commun. 9 (1) (2018) 1334.
[79] A. Ghaith, D. Oumbarek, E. Roussel, S. Corde, M. Labat, T. André, A. Loulergue, I. Andriyash, O. Chubar, O. Kononenko, et al., Tunable high spatio-spectral purity undulator radiation from a transported laser plasma accelerated electron beam, Sci. Rep. 9 (1) (2019) 1–12.
[80] A. Ghaith, T. André, I. Andriyash, S. Bielawski, F. Blache, F. Bouvet, F. Briquez, S. Corde, M.-E. Couprie, Y. Dietrich, et al., Transportation and manipulation of a laser plasma acceleration beam, in: 60th ICFA Advanced Beam Dynamics Workshop on Future Light Sources (FLS'18), Shanghai, China, 5-9 March 2018, JACOW Publishing, Geneva, Switzerland, 2018, pp. 56–61.

[81] A. Ghaith, D. Oumbarek-Espinos, T. André, E. Roussel, A. Loulergue, M. Labat, S. Corde, O. Kononenko, M. Valléau, O. Marcouillé, et al., Control of undulator radiation using a laser plasma acceleration source, in: Journal of Physics: Conference Series, 1596, (1) IOP Publishing, 2020, 012045.
[82] A.R. Maier, N. Kajumba, A. Guggenmos, C. Werle, J. Wenz, N. Delbos, B. Zeitler, I. Dornmair, J. Schmidt, E. Gullikson, et al., Water-window X-Ray pulses from a laser-plasma driven undulator, Sci. Rep. 10 (1) (2020) 1–8.
[83] LUX, http://lux.cfel.de/index.htm.
[84] K. Floettmann, Some basic features of the beam emittance, Phys. Rev. ST Accel. Beams 6 (2003) 034202, http://dx.doi.org/10.1103/PhysRevSTAB.6.034202, URL https://link.aps.org/doi/10.1103/PhysRevSTAB.6.034202.
[85] M. Migliorati, A. Bacci, C. Benedetti, E. Chiadroni, M. Ferrario, A. Mostacci, L. Palumbo, A. Rossi, L. Serafini, P. Antici, Intrinsic normalized emittance growth in laser-driven electron accelerators, Phys. Rev. ST Accel. Beams 16 (1) (2013) 011302.
[86] P. Antici, A. Bacci, C. Benedetti, E. Chiadroni, M. Ferrario, A. Rossi, L. Lancia, M. Migliorati, A. Mostacci, L. Palumbo, et al., Laser-driven electron beamlines generated by coupling laser-plasma sources with conventional transport systems, J. Appl. Phys. 112 (4) (2012) 044902.
[87] M. Khojoyan, F. Briquez, M. Labat, A. Loulergue, O. Marcouillé, F. Marteau, G. Sharma, M. Couprie, Transport studies of LPA electron beam towards the FEL amplification at COXINEL, Nucl. Instrum. Methods Phys. Res. A 829 (2016) 260–264.
[88] A. Maier, A. Meseck, S. Reiche, C. Schroeder, T. Seggebrock, F. Gruener, Demonstration scheme for a laser-plasma-driven free-electron laser, Phys. Rev. X 2 (3) (2012) 031019.
[89] Z. Huang, Y. Ding, C.B. Schroeder, Compact X-ray free-electron-laser from a laser-plasma accelerator using a transverse-gradient undulator, PRL 109 (2012) 204801.
[90] T. Smith, J. Madey, L. Elias, D.G. Deacon, Reducing the sensitivity of a free electron laser to electron energy , J. Appl. Phys. 50 (1979) 4580.
[91] R. D'Arcy, S. Wesch, A. Aschikhin, S. Bohlen, C. Behrens, M. Garland, L. Goldberg, P. Gonzalez, A. Knetsch, V. Libov, et al., Tunable plasma-based energy dechirper, Phys. Rev. Lett. 122 (3) (2019) 034801.
[92] Y. Wu, Y. Du, J. Zhang, Z. Zhou, Z. Cheng, S. Zhou, J. Hua, C. Pai, W. Lu, A preliminary experimental study of energy chirp reduction by a plasma dechirper, in: Proceedings of IPAC17, Copenhagen, 2017, pp. 1258–1260.
[93] V. Shpakov, M. Anania, M. Bellaveglia, A. Biagioni, F. Bisesto, F. Cardelli, M. Cesarini, E. Chiadroni, A. Cianchi, G. Costa, et al., Longitudinal phase-space manipulation with beam-driven plasma wakefields, Phys. Rev. Lett. 122 (11) (2019) 114801.
[94] W. Wang, K. Feng, L. Ke, C. Yu, Y. Xu, R. Qi, Y. Chen, Z. Qin, Z. Zhang, M. Fang, et al., Free-electron lasing at 27 nanometres based on a laser wakefield accelerator, Nature 595 (7868) (2021) 516–520.
[95] P. Elleaume, J. Chavanne, B. Faatz, Design considerations for a 1åSASE undulator, Nucl. Instrum. Methods Phys. Res. A 455 (3) (2000) 503–523.
[96] J. Derouillat, A. Beck, F. Pérez, T. Vinci, M. Chiaramello, A. Grassi, M. Flé, G. Bouchard, I. Plotnikov, N. Aunai, J. Dargent, C. Riconda, M. Grech, Smilei : A collaborative, open-source, multi-purpose particle-in-cell code for plasma simulation, Comput. Phys. Comm. 222 (2018) 351–373, http://dx.doi.org/10.1016/j.cpc.2017.09.024, URL http://www.sciencedirect.com/science/article/pii/S0010465517303314.
[97] V. Malka, S. Fritzler, E. Lefebvre, M.-M. Aleonard, F. Burgy, J.-P. Chambaret, J.-F. Chemin, K. Krushelnick, G. Malka, S. Mangles, Z. Najmudin, M. Pittman, J.-P. Rousseau, J.-N. Scheurer, B. Walton, A. Dangor, Electron acceleration by a wake field forced by an intense ultrashort laser pulse, Science 298 (5598) (2002) 1596–1600, http://dx.doi.org/10.1126/science.1076782, arXiv:http://science.sciencemag.org/content/298/5598/1596.full.pdf, URL http://science.sciencemag.org/content/298/5598/1596.
[98] S. Mangles, C. Murphy, Z. Najmudin, A. Thomas, J. Collier, A. Dangor, E. Divall, P. Foster, J. Gallacher, C. Hooker, D. Jaroszynski, A. Langley, W. Mori, P. Norreys, F. Tsung, R. Viskup, B. Walton, K. Krushelnick, Monoenergetic beams of relativistic electrons from intense laser-plasma interactions, Nature 431 (2004) 535–538.
[99] C. Geddes, C. Toth, J. van Tilborg, E. Esarey, C. Schroeder, D. Bruhwiler, C. Nieter, J. Cary, W. Leemans, High-quality electron beams from a laser wakefield accelerator using plasma-channel guiding, Nature 431 (2004) 538–541.
[100] J. Faure, Y. Glinec, A. Pukhov, S. Kiselev, S. Gordienko, E. Lefebvre, J.-P. Rousseau, F. Burgy, V. Malka, A laser-plasma accelerator producing monoenergetic electron beams, Nature 431 (2004) 541–544.
[101] A. Pukhov, Strong field interaction of laser radiation, Rep. Progr. Phys. 66 (1) (2002) 47.
[102] W. Lu, C. Huang, M. Zhou, W. Mori, T. Katsouleas, Nonlinear theory for relativistic plasma wakefields in the blowout regime, Phys. Rev. Lett. 96 (2006) 165002, http://dx.doi.org/10.1103/PhysRevLett.96.165002, URL https://link.aps.org/doi/10.1103/PhysRevLett.96.165002.
[103] P. Sprangle, C.-M. Tang, E. Esarey, Relativistic self-focusing of short-pulse radiation beams in plasmas, IEEE Trans. Plasma Sci. 15 (1987) 145, http://dx.doi.org/10.1109/TPS.1987.4316677, URL http://ieeexplore.ieee.org/document/4316677/.
[104] G.-Z. Sun, E. Ott, Y. Lee, P. Guzdar, Self-focusing of short intense pulses in plasmas, Phys. Fluids 30 (2) (1987) 526–532, http://dx.doi.org/10.1063/1.866349, arXiv:http://aip.scitation.org/doi/pdf/10.1063/1.866349.
[105] S. Kalmykov, S. Yi, V. Khudik, G. Shvets, Electron self-injection and trapping into an evolving plasma bubble, Phys. Rev. Lett. 103 (2009) 135004, http://dx.doi.org/10.1103/PhysRevLett.103.135004, URL http://link.aps.org/doi/10.1103/PhysRevLett.103.135004.
[106] S. Kalmykov, A. Beck, S. Yi, V. Khudik, M. Downer, E. Lefebvre, B. Shadwick, D. Umstadter, Electron self-injection into an evolving plasma bubble: Quasi-monoenergetic laser-plasma acceleration in the blowout regime, Phys. Plasmas 18 (5) (2011) 056704, http://dx.doi.org/10.1063/1.3566062.
[107] E. Esarey, R. Hubbard, W. Leemans, A. Ting, P. Sprangle, Electron injection into plasma wakefields by colliding laser pulses, Phys. Rev. Lett. 79 (1997) 2682–2685, http://dx.doi.org/10.1103/PhysRevLett.79.2682, URL https://link.aps.org/doi/10.1103/PhysRevLett.79.2682.
[108] J. Faure, C. Rechatin, A. Norlin, A. Lifschitz, Y. Glinec, V. Malka, Controlled injection and acceleration of electrons in plasma wakefields by colliding laser pulses, Nature 444 (2006) 737–739.
[109] C. Rechatin, X. Davoine, A. Lifschitz, A.B. Ismail, J. Lim, E. Lefebvre, J. Faure, V. Malka, Observation of beam loading in a laser-plasma accelerator, Phys. Rev. Lett. 103 (2009) 194804, http://dx.doi.org/10.1103/PhysRevLett.103.194804, URL https://link.aps.org/doi/10.1103/PhysRevLett.103.194804.
[110] C. McGuffey, A. Thomas, W. Schumaker, T. Matsuoka, V. Chvykov, F. Dollar, G. Kalintchenko, V. Yanovsky, A. Maksimchuk, K. Krushelnick, V.Y. Bychenkov, I. Glazyrin, A. Karpeev, Ionization induced trapping in a laser wakefield accelerator, Phys. Rev. Lett. 104 (2010) 025004, http://dx.doi.org/10.1103/PhysRevLett.104.025004, URL http://link.aps.org/doi/10.1103/PhysRevLett.104.025004.
[111] A. Pak, K. Marsh, S. Martins, W. Lu, W. Mori, C. Joshi, Injection and trapping of tunnel-ionized electrons into laser-produced wakes, Phys. Rev. Lett. 104 (2010) 025003, http://dx.doi.org/10.1103/PhysRevLett.104.025003, URL https://link.aps.org/doi/10.1103/PhysRevLett.104.025003.
[112] B. Pollock, C. Clayton, J. Ralph, F. Albert, A. Davidson, L. Divol, C. Filip, S. Glenzer, K. Herpoldt, W. Lu, K. Marsh, J. Meinecke, W. Mori, A. Pak, T. Rensink, J. Ross, J. Shaw, G. Tynan, C. Joshi, D. Froula, Demonstration of a narrow energy spread, ∼0.5 GeV electron beam from a two-stage laser wakefield accelerator, Phys. Rev. Lett. 107 (2011) 045001, http://dx.doi.org/10.1103/PhysRevLett.107.045001, URL http://link.aps.org/doi/10.1103/PhysRevLett.107.045001.
[113] G. Golovin, S. Chen, N. Powers, C. Liu, S. Banerjee, J. Zhang, M. Zeng, Z. Sheng, D. Umstadter, Tunable monoenergetic electron beams from independently controllable laser-wakefield acceleration and injection, Phys. Rev. ST Accel. Beams 18 (2015) 011301, http://dx.doi.org/10.1103/PhysRevSTAB.18.011301, URL https://link.aps.org/doi/10.1103/PhysRevSTAB.18.011301.
[114] S. Bulanov, N. Naumova, F. Pegoraro, J. Sakai, Particle injection into the wave acceleration phase due to nonlinear wake wave breaking, Phys. Rev. E 58 (1998) R5257–R5260, http://dx.doi.org/10.1103/PhysRevE.58.R5257, URL http://link.aps.org/doi/10.1103/PhysRevE.58.R5257.

[115] J. Faure, C. Rechatin, O. Lundh, L. Ammoura, V. Malka, Injection and acceleration of quasimonoenergetic relativistic electron beams using density gradients at the edges of a plasma channel, Phys. Plasmas 17 (8) (2010) 083107, http://dx.doi.org/10.1063/1.3469581.
[116] C. Geddes, K. Nakamura, G. Plateau, C. Toth, E. Cormier-Michel, E. Esarey, C. Schroeder, J. Cary, W. Leemans, Plasma-density-gradient injection of low absolute-momentum-spread electron bunches, Phys. Rev. Lett. 100 (2008) 215004, http://dx.doi.org/10.1103/PhysRevLett.100.215004, URL http://link.aps.org/doi/10.1103/PhysRevLett.100.215004.
[117] A. Gonsalves, K. Nakamura, C. Lin, D. Panasenko, S. Shiraishi, T. Sokollik, C. Benedetti, C. Schroeder, C. Geddes, J. van Tilborg, J. Osterhoff, E. Esarey, C. Toth, W. Leemans, Tunable laser plasma accelerator based on longitudinal density tailoring, Nat. Phys. 7 (11) (2011) 862–866, URL http://dx.doi.org/10.1038/nphys2071.
[118] S.A. Samant, A.K. Upadhyay, S. Krishnagopal, High brightness electron beams from density transition laser wakefield acceleration for short-wavelength free-electron lasers, Plasma Phys. Control. Fusion 56 (9) (2014) 095003, URL http://stacks.iop.org/0741-3335/56/i=9/a=095003.
[119] K. Schmid, A. Buck, C. Sears, J. Mikhailova, R. Tautz, D. Herrmann, M. Geissler, F. Krausz, L. Veisz, Density-transition based electron injector for laser driven wakefield accelerators, Phys. Rev. ST Accel. Beams 13 (2010) 091301, http://dx.doi.org/10.1103/PhysRevSTAB.13.091301, URL https://link.aps.org/doi/10.1103/PhysRevSTAB.13.091301.
[120] A. Buck, J. Wenz, J. Xu, K. Khrennikov, K. Schmid, M. Heigoldt, J. Mikhailova, M. Geissler, B. Shen, F. Krausz, S. Karsch, L. Veisz, Shock-front injector for high-quality laser-plasma acceleration, Phys. Rev. Lett. 110 (2013) 185006, http://dx.doi.org/10.1103/PhysRevLett.110.185006, URL https://link.aps.org/doi/10.1103/PhysRevLett.110.185006.
[121] C. Thaury, E. Guillaume, A. Lifschitz, K. Ta Phuoc, M. Hansson, G. Grittani, J. Gautier, J.-P. Goddet, A. Tafzi, O. Lundh, V. Malka, Shock assisted ionization injection in laser-plasma accelerators, Sci. Rep. 5 (2015) 16310, http://dx.doi.org/10.1038/srep16310, URL http://dx.doi.org/10.1038/srep16310.
[122] F. Massimo, A. Lifschitz, C. Thaury, V. Malka, Numerical studies of density transition injection in laser wakefield acceleration, Plasma Phys. Control. Fusion 59 (8) (2017) 085004, URL http://stacks.iop.org/0741-3335/59/i=8/a=085004.
[123] W. Leemans, A. Gonsalves, H.-S. Mao, K. Nakamura, C. Benedetti, C. Schroeder, C. Tóth, J. Daniels, D. Mittelberger, S. Bulanov, J.-L. Vay, C. Geddes, E. Esarey, Multi-gev electron beams from capillary-discharge-guided subpetawatt laser pulses in the self-trapping regime, Phys. Rev. Lett. 113 (2014) 245002, http://dx.doi.org/10.1103/PhysRevLett.113.245002, URL http://link.aps.org/doi/10.1103/PhysRevLett.113.245002.
[124] H.T. Kim, K.H. Pae, H.J. Cha, I.J. Kim, T.J. Yu, J.H. Sung, S.K. Lee, T.M. Jeong, J. Lee, Enhancement of electron energy to the multi-gev regime by a dual-stage laser-wakefield accelerator pumped by petawatt laser pulses, Phys. Rev. Lett. 111 (2013) 165002, http://dx.doi.org/10.1103/PhysRevLett.111.165002, URL https://link.aps.org/doi/10.1103/PhysRevLett.111.165002.
[125] S. Steinke, J. van Tilborg, C. Benedetti, C. Geddes, C. Schroeder, J. Daniels, K. Swanson, A. Gonsalves, K. Nakamura, N. Matlis, B. Shaw, E. Esarey, W. Leemans, Multistage coupling of independent laser-plasma accelerators, Nature 530 (7589) (2016) 190–193, URL http://dx.doi.org/10.1038/nature16525.
[126] A.R. Maier, N.M. Delbos, T. Eichner, L. Hübner, S. Jalas, L. Jeppe, S.W. Jolly, M. Kirchen, V. Leroux, P. Messner, et al., Decoding sources of energy variability in a laser-plasma accelerator, Phys. Rev. X 10 (3) (2020) 031039.
[127] W.P. Leemans, B. Nagler, A.J. Gonsalves, C. Toth, K. Nakamura, C.G. Geddes, E. Esarey, C.B. Schroeder, S.M. Hooker, Gev electron beams from a cm-scale accelerator, Nat. Phys. 2 (2006) 696–699, http://dx.doi.org/10.1038/nphys418.
[128] J. Osterhoff, A. Popp, Z. Major, B. Marx, T. Rowlands-Rees, M. Fuchs, M. Geissler, R. Hörlein, B. Hidding, S. Becker, E. Peralta, U. Schramm, F. Grüner, D. Habs, F. Krausz, S. Hooker, S. Karsch, Generation of stable, low-divergence electron beams by laser-wakefield acceleration in a steady-state-flow gas cell, Phys. Rev. Lett. 101 (2008) 085002, http://dx.doi.org/10.1103/PhysRevLett.101.085002, URL https://link.aps.org/doi/10.1103/PhysRevLett.101.085002.
[129] S. Kneip, S. Nagel, S. Martins, S. Mangles, C. Bellei, O. Chekhlov, R. Clarke, N. Delerue, E. Divall, G. Doucas, K. Ertel, F. Fiuza, R. Fonseca, P. Foster, S. Hawkes, C. Hooker, K. Krushelnick, W. Mori, C. Palmer, K.T. Phuoc, P. Rajeev, J. Schreiber, M. Streeter, D. Urner, J. Vieira, L. Silva, Z. Najmudin, Near-gev acceleration of electrons by a nonlinear plasma wave driven by a self-guided laser pulse, Phys. Rev. Lett. 103 (2009) 035002, http://dx.doi.org/10.1103/PhysRevLett.103.035002, URL https://link.aps.org/doi/10.1103/PhysRevLett.103.035002.
[130] X. Wang, R. Zgadzaj, N. Fazel, Z. Li, S. Yi, X. Zhang, W. Henderson, Y.Y. Chang, R. Korzekwa, H.E. Tsai, C.H. Pai, H. Quevedo, G. Dyer, E. Gaul, M. Martinez, A. Bernstein, T. Borger, M. Spinks, M. Donovan, V. Khudik, G. Shvets, T. Ditmire, M. Downer, Quasi-monoenergetic laser-plasma acceleration of electrons to 2 GeV, Nature Commun. 4 (2013) 1988 EP, URL http://dx.doi.org/10.1038/ncomms2988.
[131] E. Guillaume, A. Döpp, C. Thaury, K. Ta Phuoc, A. Lifschitz, G. Grittani, J.-P. Goddet, A. Tafzi, S.W. Chou, L. Veisz, V. Malka, Electron rephasing in a laser-wakefield accelerator, Phys. Rev. Lett. 115 (2015) 155002, http://dx.doi.org/10.1103/PhysRevLett.115.155002, URL https://link.aps.org/doi/10.1103/PhysRevLett.115.155002.
[132] Y. Li, D. Li, K. Huang, M. Tao, M. Li, J. Zhao, Y. Ma, X. Guo, J. Wang, M. Chen, N. Hafz, J. Zhang, L. Chen, Generation of 20 ka electron beam from a laser wakefield accelerator, Phys. Plasmas 24 (2) (2017) 023108, http://dx.doi.org/10.1063/1.4975613.
[133] M. Hansson, B. Aurand, H. Ekerfelt, A. Persson, O. Lundh, Injection of electrons by colliding laser pulses in a laser wakefield accelerator, Nucl. Instrum. Methods Phys. Res. A 829 (2016) 99–103, http://dx.doi.org/10.1016/j.nima.2016.02.070, URL http://www.sciencedirect.com/science/article/pii/S0168900216002461, 2nd European Advanced Accelerator Concepts Workshop - EAAC 2015.
[134] M. Mirzaie, S. Li, M. Zeng, N. Hafz, M. Chen, G. Li, Q. Zhu, H. Liao, T. Sokollik, F. Liu, Y. Ma, L. Chen, Z. Sheng, J. Zhang, Demonstration of self-truncated ionization injection for GeV electron beams, Sci. Rep. 5 (1) (2015) 14659, http://dx.doi.org/10.1038/srep14659, URL https://doi.org/10.1038/srep14659.
[135] A. Irman, J. Couperus, A. Debus, A. Köhler, J. Krämer, R. Pausch, O. Zarini, U. Schramm, Improved performance of laser wakefield acceleration by tailored self-truncated ionization injection, Plasma Phys. Control. Fusion 60 (4) (2018) 044015.
[136] M. Burza, A. Gonoskov, K. Svensson, F. Wojda, A. Persson, M. Hansson, G. Genoud, M. Marklund, C.-G. Wahlström, O. Lundh, Laser wakefield acceleration using wire produced double density ramps, Phys. Rev. ST Accel. Beams 16 (2013) 011301, http://dx.doi.org/10.1103/PhysRevSTAB.16.011301, URL https://link.aps.org/doi/10.1103/PhysRevSTAB.16.011301.
[137] M. Hansson, B. Aurand, X. Davoine, H. Ekerfelt, K. Svensson, A. Persson, C.-G. Wahlström, O. Lundh, Down-ramp injection and independently controlled acceleration of electrons in a tailored laser wakefield accelerator, Phys. Rev. ST Accel. Beams 18 (2015) 071303, http://dx.doi.org/10.1103/PhysRevSTAB.18.071303, URL https://link.aps.org/doi/10.1103/PhysRevSTAB.18.071303.
[138] W. Wang, W. Li, J. Liu, Z. Zhang, R. Qi, C. Yu, J. Liu, M. Fang, Z. Qin, C. Wang, Y. Xu, F. Wu, Y. Leng, R. Li, Z. Xu, High-brightness high-energy electron beams from a laser wakefield accelerator via energy chirp control, Phys. Rev. Lett. 117 (2016) 124801, http://dx.doi.org/10.1103/PhysRevLett.117.124801, URL https://link.aps.org/doi/10.1103/PhysRevLett.117.124801.
[139] K. Swanson, H.-E. Tsai, S. Barber, R. Lehe, H.-S. Mao, S. Steinke, J. van Tilborg, K. Nakamura, C.R. Geddes, C. Schroeder, E. Esarey, W. Leemans, Control of tunable, monoenergetic laser-plasma-accelerated electron beams using a shock-induced density downramp injector, Phys. Rev. Accel. Beams 20 (2017) 051301, http://dx.doi.org/10.1103/PhysRevAccelBeams.20.051301, URL https://link.aps.org/doi/10.1103/PhysRevAccelBeams.20.051301.
[140] M. Hansson, T.L. Audet, H. Ekerfelt, B. Aurand, I.G. González, F.G. Desforges, X. Davoine, A. Maitrallain, S. Reymond, P. Monot, A. Persson, S.D. Dufrénoy, C.-G. Wahlström, B. Cros, O. Lundh, Localization of ionization-induced trapping in a laser wakefield accelerator using a density down-ramp, Plasma Phys. Control. Fusion 58 (5) (2016) 055009, URL http://stacks.iop.org/0741-3335/58/i=5/a=055009.

[141] M. Downer, R. Zgadzaj, A. Debus, U. Schramm, M. Kaluza, Diagnostics for plasma-based electron accelerators, Rev. Modern Phys. 90 (3) (2018) 035002.
[142] P. Mora, T.M. Antonsen Jr., Kinetic modeling of intense, short laser pulses propagating in tenuous plasmas, Phys. Plasmas 4 (1) (1997) 217–229, http://dx.doi.org/10.1063/1.872134, URL https://doi.org/10.1063/1.872134.
[143] L. Gorbunov, V. Kirsanov, Excitation of plasma waves by an electromagnetic wave packet, Sov. Phys.—JETP 66 (2) (1987) 290–294.
[144] P. Sprangle, G. Joyce, E. Esarey, A. Ting, Laser wakefield acceleration and relativstic optical guiding, in: AIP Conference Proceedings, 175, (1) American Institute of Physics, 1988, pp. 231–239.
[145] P. Sprangle, E. Esarey, Interaction of ultrahigh laser fields with beams and plasmas, Phys. Fluids B 4 (7) (1992) 2241–2248, http://dx.doi.org/10.1063/1.860192, URL https://doi.org/10.1063/1.860192.
[146] A. Pukhov, J. Meyer-Ter-Vehn, Laser wake field acceleration: the highly non-linear broken-wave regime, Appl. Phys. B 74 (2002) 355, URL https://link.springer.com/article/10.1007/s003400200795.
[147] S. Gordienko, A. Pukhov, Scalings for ultrarelativistic laser plasmas and quasimonoenergetic electrons, Phys. Plasmas 12 (4) (2005) 043109, http://dx.doi.org/10.1063/1.1884126, URL https://doi.org/10.1063/1.1884126.
[148] W. Lu, M. Tzoufras, C. Joshi, F. Tsung, W. Mori, J. Vieira, R. Fonseca, L. Silva, Generating multi-gev electron bunches using single stage laser wakefield acceleration in a 3D nonlinear regime, Phys. Rev. ST Accel. Beams 10 (2007) 061301, http://dx.doi.org/10.1103/PhysRevSTAB.10.061301, URL https://link.aps.org/doi/10.1103/PhysRevSTAB.10.061301.
[149] I. Kostyukov, A. Pukhov, S. Kiselev, Phenomenological theory of laser-plasma interaction in "bubble" regime, Phys. Plasmas 11 (11) (2004) 5256–5264, http://dx.doi.org/10.1063/1.1799371, URL https://doi.org/10.1063/1.1799371.
[150] R. Lehe, Improvement of laser-wakefield accelerators: towards a compact free electron laser, (Ph.D. thesis), Ecole Polytechnique, 2014, URL https://pastel.archives-ouvertes.fr/tel-01088398.
[151] C. Decker, W. Mori, K.-C. Tzeng, T. Katsouleas, The evolution of ultra-intense, short-pulse lasers in underdense plasmas, Phys. Plasmas 3 (5) (1996) 2047–2056, http://dx.doi.org/10.1063/1.872001, URL https://doi.org/10.1063/1.872001.
[152] G. Plateau, C. Geddes, D. Thorn, M. Chen, C. Benedetti, E. Esarey, A. Gonsalves, N. Matlis, K. Nakamura, C. Schroeder, S. Shiraishi, T. Sokollik, J. van Tilborg, C. Toth, S. Trotsenko, T. Kim, M. Battaglia, T. Stöhlker, W. Leemans, Low-emittance electron bunches from a laser-plasma accelerator measured using single-shot X-Ray spectroscopy, Phys. Rev. Lett. 109 (2012) 064802, http://dx.doi.org/10.1103/PhysRevLett.109.064802, URL https://link.aps.org/doi/10.1103/PhysRevLett.109.064802.
[153] R. Weingartner, S. Raith, A. Popp, S. Chou, J. Wenz, K. Khrennikov, M. Heigoldt, A. Maier, N. Kajumba, M. Fuchs, B. Zeitler, F. Krausz, S. Karsch, F. Grüner, Ultralow emittance electron beams from a laser-wakefield accelerator, Phys. Rev. ST Accel. Beams 15 (2012) 111302, http://dx.doi.org/10.1103/PhysRevSTAB.15.111302, URL https://link.aps.org/doi/10.1103/PhysRevSTAB.15.111302.
[154] S. Kneip, C. McGuffey, J. Martins, M. Bloom, V. Chvykov, F. Dollar, R. Fonseca, S. Jolly, G. Kalintchenko, K. Krushelnick, A. Maksimchuk, S. Mangles, Z. Najmudin, C. Palmer, K.T. Phuoc, W. Schumaker, L. Silva, J. Vieira, V. Yanovsky, A. Thomas, Characterization of transverse beam emittance of electrons from a laser-plasma wakefield accelerator in the bubble regime using betatron x-ray radiation, Phys. Rev. ST Accel. Beams 15 (2012) 021302, http://dx.doi.org/10.1103/PhysRevSTAB.15.021302, URL https://link.aps.org/doi/10.1103/PhysRevSTAB.15.021302.
[155] T. Mehrling, J. Grebenyuk, F. Tsung, K. Floettmann, J. Osterhoff, Transverse emittance growth in staged laser-wakefield acceleration, Phys. Rev. ST Accel. Beams 15 (2012) 111303, http://dx.doi.org/10.1103/PhysRevSTAB.15.111303, URL https://link.aps.org/doi/10.1103/PhysRevSTAB.15.111303.
[156] I. Dornmair, K. Floettmann, A. Maier, Emittance conservation by tailored focusing profiles in a plasma accelerator, Phys. Rev. ST Accel. Beams 18 (2015) 041302, http://dx.doi.org/10.1103/PhysRevSTAB.18.041302, URL https://link.aps.org/doi/10.1103/PhysRevSTAB.18.041302.
[157] A. Ghaith, C. Kitegi, T. André, M. Valléau, F. Marteau, J. Vétéran, F. Blache, C. Benabderrahmane, O. Cosson, F. Forest, et al., Tunable high gradient quadrupoles for a laser plasma acceleration based FEL, Nucl. Instrum. Methods Phys. Res. A 909 (2018) 290–293.
[158] C. Thaury, E. Guillaume, A. Döpp, R. Lehe, A. Lifschitz, K.T. Phuoc, J. Gautier, J.-P. Goddet, A. Tafzi, A. Flacco, et al., Demonstration of relativistic electron beam focusing by a laser-plasma lens, Nature Commun. 6 (2015).
[159] J. Van Tilborg, S. Steinke, C. Geddes, N. Matlis, B. Shaw, A. Gonsalves, J. Huijts, K. Nakamura, J. Daniels, C. Schroeder, et al., Active plasma lensing for relativistic laser-plasma-accelerated electron beams, Phys. Rev. Lett. 115 (18) (2015) 184802.
[160] N. Nakanii, T. Hosokai, K. Iwasa, S. Masuda, A. Zhidkov, N. Pathak, H. Nakahara, Y. Mizuta, N. Takeguchi, R. Kodama, Transient magnetized plasma as an optical element for high power laser pulses, Phys. Rev. ST Accel. Beams 18 (2) (2015) 021303.
[161] J.M. Dawson, Particle simulation of plasmas, Rev. Modern Phys. 55 (1983) 403–447, http://dx.doi.org/10.1103/RevModPhys.55.403, URL https://link.aps.org/doi/10.1103/RevModPhys.55.403.
[162] R. Hockney, J. Eastwood, Computer Simulation using Particles, CRC Press, 1988.
[163] C. Birdsall, A. Langdon, Plasma Physics Via Computer Simulation, Taylor and Francis Group, 2004.
[164] J. Boris, Relativistic Plasma Simulation - Optimization of a Hybrid Code, in: Proceedings, Fourth Conference on the Numerical Simulation of Plasma, 1970.
[165] J.-L. Vay, Simulation of beams or plasmas crossing at relativistic velocity, Phys. Plasmas 15 (5) (2008) 056701.
[166] K. Yee, Numerical solution of initial boundary value problems involving maxwell's equations in isotropic media, IEEE Trans. Antennas and Propagation 14 (1966) 302–307, http://dx.doi.org/10.1109/TAP.1966.1138693.
[167] A. Taflove, S. Hagness, Computational Electrodynamics: The Finite-Difference Time-Domain Method, third ed., Artech House, Norwood, MA, 2005.
[168] T. Esirkepov, Exact charge conservation scheme for particle-in-cell simulation with an arbitrary form-factor, Comput. Phys. Comm. 135 (2) (2001) 144–153, http://dx.doi.org/10.1016/S0010-4655(00)00228-9, URL http://www.sciencedirect.com/science/article/pii/S0010465500002289.
[169] X. Davoine, E. Lefebvre, J. Faure, C. Rechatin, A. Lifschitz, V. Malka, Simulation of quasimonoenergetic electron beams produced by colliding pulse wakefield acceleration, Phys. Plasmas 15 (11) (2008) 113102, http://dx.doi.org/10.1063/1.3008051.
[170] A. Lifschitz, X. Davoine, E. Lefebvre, J. Faure, C. Rechatin, V. Malka, Particle-in-cell modelling of laser-plasma interaction using Fourier decomposition, J. Comput. Phys. 228 (5) (2009) 1803–1814, http://dx.doi.org/10.1016/j.jcp.2008.11.017, URL http://www.sciencedirect.com/science/article/pii/S0021999108005950.
[171] J.-L. Vay, Noninvariance of space-and time-scale ranges under a Lorentz transformation and the implications for the study of relativistic interactions, Phys. Rev. Lett. 98 (13) (2007) 130405.
[172] B. Godfrey, Numerical cherenkov instabilities in electromagnetic particle codes, J. Comput. Phys. 15 (1974) 504–521, http://dx.doi.org/10.1016/0021-9991(74)90076-X.
[173] R. Nuter, M. Grech, P.G. de Alaiza Martinez, G. Bonnaud, E. d'Humières, Maxwell solvers for the simulations of the laser-matter interaction, Eur. Phys. J. D 68 (6) (2014) 1–9.
[174] A. Blinne, D. Schinkel, S. Kuschel, N. Elkina, S.G. Rykovanov, M. Zepf, A systematic approach to numerical dispersion in maxwell solvers, Comput. Phys. Comm. 224 (2018) 273–281.
[175] J.-L. Vay, I. Haber, B. Godfrey, A domain decomposition method for pseudo-spectral electromagnetic simulations of plasmas, J. Comput. Phys. 243 (2013) 260–268, http://dx.doi.org/10.1016/j.jcp.2013.03.010, URL http://www.sciencedirect.com/science/article/pii/S0021999113001873.

[176] I.A. Andriyash, R. Lehe, A. Lifschitz, Laser-plasma interactions with a Fourier-bessel particle-in-cell method, Phys. Plasmas 23 (3) (2016) http://dx.doi.org/10.1063/1.4943281, URL http://scitation.aip.org/content/aip/journal/pop/23/3/10.1063/1.4943281.
[177] R. Lehe, M. Kirchen, I.A. Andriyash, B.B. Godfrey, J.-L. Vay, A spectral, quasi-cylindrical and dispersion-free particle-in-cell algorithm, Comput. Phys. Comm. 203 (2016) 66–82, http://dx.doi.org/10.1016/j.cpc.2016.02.007, URL http://www.sciencedirect.com/science/article/pii/S0010465516300224.
[178] A. Pukhov, X-dispersionless maxwell solver for plasma-based particle acceleration, J. Comput. Phys. 418 (2020) 109622.
[179] A. Beck, S. Kalmykov, X. Davoine, A. Lifschitz, B. Shadwick, V. Malka, A. Specka, Physical processes at work in sub-30fs, PW laser pulse-driven plasma accelerators: Towards GeV electron acceleration experiments at cilex facility, Nucl. Instrum. Methods Phys. Res. A 740 (2014) 67–73, http://dx.doi.org/10.1016/j.nima.2013.11.003, URL http://www.sciencedirect.com/science/article/pii/S0168900213015039, Proceedings of the first European Advanced Accelerator Concepts Workshop 2013.
[180] R. Lehe, A. Lifschitz, C. Thaury, V. Malka, X. Davoine, Numerical growth of emittance in simulations of laser-wakefield acceleration, Phys. Rev. ST Accel. Beams 16 (2013) 021301, http://dx.doi.org/10.1103/PhysRevSTAB.16.021301, URL http://link.aps.org/doi/10.1103/PhysRevSTAB.16.021301.
[181] X. Wang, R. Zgadzaj, N. Fazel, Z. Li, S. Yi, X. Zhang, W. Henderson, Y.Y. Chang, R. Korzekwa, H.E. Tsai, C.H. Pai, H. Quevedo, G. Dyer, E. Gaul, M. Martinez, A. Bernstein, T. Borger, M. Spinks, M. Donovan, V. Khudik, G. Shvets, T. Ditmire, M. Downer, Quasi-monoenergetic laser-plasma acceleration of electrons to 2 GeV, Nature Commun. 4 (2013) 1988 EP, URL http://dx.doi.org/10.1038/ncomms2988.
[182] G. Pariente, V. Gallet, A. Borot, O. Gobert, F. Quéré, Space–time characterization of ultra-intense femtosecond laser beams, Nat. Photonics 10 (2016) 547 EP, URL http://dx.doi.org/10.1038/nphoton.2016.140.
[183] J. Larmor, On the theory of the magnetic influence on spectra and on the radiation from moving ions, Lond. Edinb. Dublin Philos. Mag. J. Sci. 44 (271) (1897) 503–512.
[184] A. Liénard, La théorie de Lorentz et celle de Larmor, ÉClairage ÉLectrique 16 (1898) 320–334.
[185] G.A. Schott, On the radiation from groups of electrons, Ann. Physics 24 (1907) 635–660.
[186] D. Iwanenko, I. Pomeranchuk, On the maximal energy attainable in a betatron, Phys. Rev. 65 (11–12) (1944) 343.
[187] M. Oliphant, The acceleration of particles to very high energies, 1943, Classified Memo Submitted To DSIR University of Birmingham Archive.
[188] E.M. McMillan, The synchrotron–A proposed high energy particle accelerator, Phys. Rev. 68 (5–6) (1945) 143.
[189] V. Veksler, J. of Phys, USSR 9 (1945) 153–158.
[190] J. Schwinger, Electron radiation in high energy accelerators, in: Physical Review, 70, (9–10) American Physical Soc one Physics Ellipse, College PK, MD 20740-3844 USA, 1946, pp. 798–799.
[191] J. Schwinger, On the classical radiation of accelerated electrons, Phys. Rev. 75 (12) (1949) 1912.
[192] J.P. Blewett, Radiation losses in the induction electron accelerator, Phys. Rev. 69 (3–4) (1946) 87.
[193] F. Elder, A. Gurewitsch, R. Langmuir, H. Pollock, Radiation from electrons in a synchrotron, Phys. Rev. 71 (11) (1947) 829.
[194] V.L. Ginzburg, Microwave radiation and its absorption in air, Bull. Acad. Sci. USSR 11 (2) (1947) 165–182.
[195] H. Motz, Applications of the radiation from fast electron beams, J. Appl. Phys. 22 (5) (1951) 527–535.
[196] H. Motz, M. Nakamura, Radiation of an electron in an infinitely long waveguide, Ann. Physics 7 (1) (1959) 84–131.
[197] H. Motz, W. Thon, R. Whitehurst, Experiments on radiation by fast electron beams, J. Appl. Phys. 24 (7) (1953) 826–833.
[198] R. Combe, T. Frelot, Production d'ondes millimétriques par un ondulateur magnétique, Note de M. René Combe et de Mme Thérèse Frelot, présentée par M. Louis de Broglie, SÉance Du 28 Novembre 1955, C. R. Hebd. Seances Acad. Sci. 241 (1955) 1959–1960.
[199] A. Medvedev, M. Nikitin, Undulator radiation, Russian Phys. J. 17 (10) (1974) 1452–1453.
[200] A. Hofmann, Quasi-monochromatic synchrotron radiation from undulators, Nucl. Instrum. Methods 152 (1) (1978) 17–21.
[201] R. Coisson, Angular-spectral distribution and polarization of synchrotron radiation from a" short" magnet, Phys. Rev. A 20 (2) (1979) 524.
[202] R. Coisson, Spatial coherence of synchrotron radiation, Appl. Opt. 34 (5) (1995) 904–908.
[203] O. Chubar, P. Elleaume, Accurate and efficient computation of synchrotron radiation in the near field region, in: Proc. of the EPAC98 Conference, 1998, pp. 1177–1179.
[204] R. Walker, Near field effects in off-axis undulator radiation, Nucl. Instrum. Methods Phys. Res. A 267 (2–3) (1988) 537–546.
[205] R.P. Walker, Interference effects in undulator and wiggler radiation sources, Nucl. Instrum. Methods Phys. Res. A 335 (1–2) (1993) 328–337.
[206] H. Onuki, P. Elleaume, Undulators, Wigglers and their Applications, CRC Press, 2003.
[207] K.-J. Kim, Brightness, coherence and propagation characteristics of synchrotron radiation, Nucl. Instrum. Methods Phys. Res. A 246 (1–3) (1986) 71–76.
[208] G. Geloni, E. Saldin, E. Schneidmiller, M. Yurkov, Transverse coherence properties of X-ray beams in third-generation synchrotron radiation sources, Nucl. Instrum. Methods Phys. Res. A 588 (3) (2008) 463–493.
[209] R. Coisson, R. Walker, Phase space distribution of brilliance of undulator sources, in: Insertion Devices for Synchrotron Sources, 582, International Society for Optics and Photonics, 1986, pp. 24–31.
[210] R.P. Walker, Insertion devices: Undulators and wigglers, CERN, 1998.
[211] R.R. Lindberg, K.-J. Kim, Compact representations of partially coherent undulator radiation suitable for wave propagation, Phys. Rev. Special Top. Accelerators Beams 18 (9) (2015) 090702.
[212] R.P. Walker, Undulator radiation brightness and coherence near the diffraction limit, Phys. Rev. Accel. Beams 22 (5) (2019) 050704.
[213] G. Dattoli, A. Renieri, Experimental and theoretical aspects of the free-electron laser, in: Laser Handbook, Elsevier, 1985, pp. 1–141.
[214] F. Ciocci, D. Giuseppe, R. Alberto, T. Amalia, Insertion devices for synchrotron radiation and free electron laser, vol. 6, World Scientific, 2000.
[215] D.A. Deacon, L. Elias, J.M. Madey, G. Ramian, H. Schwettman, T. Smith, First operation of a free electron laser, Phys. Rev. Lett. 38 (16) (1977) 892–894.
[216] M. Billardon, P. Elleaume, J. Ortéga, C. Bazin, M. Bergher, M. Velghe, Y. Petroff, D. Deacon, K. Robinson, J. Madey, First operation of a storage-ring free-electron laser, Phys. Rev. Lett. 51 (18) (1983) 1652–1655.
[217] R. Warren, B. Newnam, W. Stein, J. Winston, R. Sheffield, M. Lynch, J. Goldstein, M. Whitehead, O. Norris, G. Luedemann, T. Gibson, C. Humphry, First operation of the los alamos free-electron laser oscillator, in: Sixth International Conference on Lasers and Applications, Lasers, San Franscisco, December 12-16, 1983, 425, (4) Society for Optical and Quantum Electronics, 1983, 042016.
[218] J. Edighoffer, G. Neil, C. Hess, T.I. Smith, S. Fornaca, H. Schwettman, Variable-wiggler free-electron-laser oscillation, Phys. Rev. Lett. 52 (5) (1984) 344.
[219] N. Kroll, P.L. Morton, M. Rosenbluth, Variable parameter free-electron laser, in: Free-Electron Generators of Coherent Radiation : Edited By SF Jacobs, HS Pilloff, M. Sargent, MO Scully and R. Spitzer, 1, 1980, pp. 89–112.
[220] D.W. Feldman, H. Takeda, R.W. Warren, J.E. Sollid, W.E. Stein, W.J. Johnson, A.H. Lumpkin, R.B. Feldman, High extraction efficiency experiments with the los alamos free electron laser, Nucl. Instrum. Methods Phys. Res. A 285 (1–2) (1989) 11–16.
[221] M. Couprie, Storage rings FELs, Nucl. Instrum. Methods Phys. Res. A 393 (1–3) (1997) 13–17.
[222] M.E. Couprie, Short wavelength free-electron laser sources, C. R. de l'Académie Des Sci. Ser. IV Phys. 1 (3) (2000) 329–345.
[223] N. Vinokurov, I. Drobyazko, G. Kulipanov, V. Litvinenko, I. Pinayev, Lasing in visible and ultraviolet regions in an optical klystron installed on the VEPP-3 storage ring, Rev. Sci. Instrum. 60 (7) (1989) 1435–1438.

[224] M. Couprie, D. Garzella, M. Billardon, Operation of the super-ACO free-electron laser in the UV range at 800 MeV, Europhys. Lett. 21 (9) (1993) 909.
[225] D. Nutarelli, D. Garzella, E. Renault, L. Nahon, M.E. Couprie, Super-ACO FEL oscillation at 300 nm, Nucl. Instrum. Methods Phys. Res. A 445 (1) (2000) 143–148.
[226] T. Yamazaki, K. Yamada, S. Sugiyama, H. Ohgaki, N. Sei, T. Mikado, T. Noguchi, M. Chiwaki, R. Suzuki, M. Kawai, et al., First lasing of the NIJI-IV storage-ring free-electron laser, Nucl. Instrum. Methods Phys. Res. A 331 (1–3) (1993) 27–33.
[227] R. Roux, M. Couprie, R. Bakker, D. Garzella, D. Nutarelli, L. Nahon, M. Billardon, High current operation of a storage-ring free-electron laser, Phys. Rev. E 58 (5) (1998) 6584.
[228] M. Hosaka, S. Koda, M. Katoh, J. Yamazaki, K. Hayashi, K. Takashima, T. Gejo, H. Hama, From the operation of an SRFEL to a user facility, Nucl. Instrum. Methods Phys. Res. A 483 (1) (2002) 146–151.
[229] T.D.G. Berges, K. Dunkel, A. Lüdecke, B. Keil, E. Kasel, A. Jankowiak, C. Piel, T. Weis, D. Zimmoch, D. Nölle, et al., First lasing of the FELICITA I FEL at DELTA, Nucl. Instrum. Methods Phys. Res. A 445 (1) (2000) 128–133.
[230] V. Litvinenko, S. Park, I. Pinayev, Y. Wu, M. Emamian, N. Hower, P. Morcombe, O. Oakeley, G. Swift, P. Wang, OK-4/Duke storage ring FEL lasing in the deep-UV, Nucl. Instrum. Methods Phys. Res. A 429 (1) (1999) 151–158.
[231] V.N. Litvinenko, S.H. Park, I.V. Pinayev, Y. Wu, Operation of the OK-4/Duke storage ring FEL below 200nm, Nucl. Instrum. Methods Phys. Res. A 475 (1) (2001) 195–204.
[232] M. Marsi, M. Trovo, R. Walker, L. Giannessi, G. Dattoli, A. Gatto, N. Kaiser, S. Günster, D. Ristau, M. Couprie, D. Garzella, J. Clarke, M. Poole, Operation and performance of a free electron laser oscillator down to 190 nm, Appl. Phys. Lett. 80 (16) (2002) 2851–2853.
[233] M. Trovo, J. Clarke, M. Couprie, G. Dattoli, D. Garzella, A. Gatto, L. Giannessi, S. Günster, N. Kaiser, M. Marsi, et al., Operation of the European storage ring FEL at ELETTRA down to 190nm, Nucl. Instrum. Methods Phys. Res. A 483 (1) (2002) 157–161.
[234] A. Gatto, J. Heber, N. Kaiser, D. Ristau, S. Günster, J. Kohlhaas, M. Marsi, M. Trovo, R. Walker, High-performance UV/VUV optics for the storage ring FEL at ELETTRA , Nucl. Instrum. Methods Phys. Res. A 483 (1) (2002) 357–362.
[235] A. Gatto, R. Thielsch, J. Heber, N. Kaiser, D. Ristau, S. Günster, J. Kohlhaas, M. Marsi, M. Trovò, R. Walker, et al., High-performance deep-ultraviolet optics for free-electron lasers, Appl. Opt. 41 (16) (2002) 3236–3241.
[236] D. Garzella, M. Couprie, T. Hara, L. Nahon, M. Brazuna, A. Delboulbé, M. Billardon, Mirror degradation and heating in storage ring FELs, Nucl. Instrum. Methods Phys. Res. A 358 (1) (1995) 387–391.
[237] B. Girard, Y. Lapierre, J. Ortéga, C. Bazin, M. Billardon, P. Elleaume, M. Bergher, M. Velghe, Y. Petroff, Optical frequency multiplication by an optical klystron, Phys. Rev. Lett. 53 (25) (1984) 2405–2408.
[238] R. Prazeres, J. Ortéga, C. Bazin, M. Bergher, M. Billardon, M. Couprie, H. Fang, M. Velghe, Y. Petroff, First production of vacuum-ultraviolet coherent light by frequency multiplication in a relativistic electron beam, Europhys. Lett. 4 (7) (1987) 817.
[239] R. Prazeres, J. Ortega, C. Bazin, M. Bergher, M. Billardon, M. Couprie, M. Velghe, Y. Petroff, Coherent harmonic generation in the vacuum ultraviolet spectral range on the storage ring ACO, Nucl. Instrum. Methods Phys. Res. A 272 (1–2) (1988) 68–72.
[240] S. Werin, M. Eriksson, J. Larsson, A. Persson, S. Svanberg, First results in coherent harmonic generation using the undulator at the MAX-lab electron storage ring, Nucl. Instrum. Methods Phys. Res. A 290 (2–3) (1990) 589–596.
[241] R. Prazeres, P. Guyot-Sionnest, J. Ortéga, D. Jaroszynski, M. Billardon, M. Couprie, M. Velghe, Y. Petroff, Coherent harmonic generation in VUV with the optical klystron on the storage ring super-ACO, Nucl. Instrum. Methods Phys. Res. A 304 (1) (1991) 72–76.
[242] M. Labat, M. Hosaka, A. Mochihashi, M. Shimada, M. Katoh, G. Lambert, T. Hara, Y. Takashima, M. Couprie, Coherent harmonic generation on UVSOR-II storage ring, Eur. Phys. J. D 44 (1) (2007) 187.
[243] V.N. Litvinenko, New results and prospects for harmonic generation in storage ring FELs, Nucl. Instrum. Methods Phys. Res. A 507 (1) (2003) 265–273.
[244] T. Orzechowski, B. Anderson, W. Fawley, D. Prosnitz, E. Scharlemann, S. Yarema, D. Hopkins, A. Paul, A. Sessler, J. Wurtele, Microwave radiation from a high-gain free-electron laser amplifier, Phys. Rev. Lett. 54 (9) (1985) 889.
[245] D. Kirkpatrick, G. Bekefi, A. Dirienzo, H. Freund, A. Ganguly, A high power, 600 μm wavelength free electron laser, Nucl. Instrum. Methods Phys. Res. A 285 (1–2) (1989) 43–46.
[246] T. Lefevre, J. Gardelle, G. Marchese, J. Rullier, J. Donohue, Self-amplified spontaneous emission and bunching at 3 GHz in a microwave free-electron laser, Phys. Rev. Lett. 82 (2) (1999) 323.
[247] S. Okuda, J. Ohkuma, N. Kimura, Y. Honda, T. Okada, S. Takamuku, T. Yamamoto, K. Tsumori, Self-amplified spontaneous emission at wavelengths of 20 and 40 μm from single-bunch electron beams, Nucl. Instrum. Methods Phys. Res. A 331 (1–3) (1993) 76–78.
[248] D. Bocek, P. Kung, H.-C. Lihn, C. Settakorn, H. Wiedemann, Observation of SASE at 47 μm, Nucl. Instrum. Methods Phys. Res. A 375 (1–3) (1996) 13–16.
[249] R. Prazeres, J. Ortéga, F. Glotin, D. Jaroszynski, O. Marcouillé, Observation of self-amplified spontaneous emission in the mid-infrared in a free-electron laser, Phys. Rev. Lett. 78 (11) (1997) 2124.
[250] M. Babzien, I. Ben-Zvi, P. Catravas, J. Fang, T. Marshall, X. Wang, J. Wurtele, V. Yakimenko, L. Yu, Observation of self-amplified spontaneous emission in the near-infrared and visible wavelengths, Phys. Rev. E 57 (1998) 6093–6100.
[251] D. Nguyen, R. Sheffield, C. Fortgang, J. Goldstein, J. Kinross-Wright, N. Ebrahim, Self-amplified spontaneous emission driven by a high-brightness electron beam, Phys. Rev. Lett. 81 (4) (1998) 810.
[252] M. Hogan, C. Pellegrini, J. Rosenzweig, G. Travish, A. Varfolomeev, S. Anderson, K. Bishofberger, P. Frigola, A. Murokh, N. Osmanov, et al., Measurements of high gain and intensity fluctuations in a self-amplified, spontaneous-emission free-electron laser, Phys. Rev. Lett. 80 (2) (1998) 289.
[253] M. Hogan, C. Pellegrini, J. Rosenzweig, S. Anderson, P. Frigola, A. Tremaine, C. Fortgang, D. Nguyen, R. Sheffield, J. Kinross-Wright, et al., Measurements of gain larger than 10^5 at 12 μm in a self-amplified spontaneous-emission free-electron laser, Phys. Rev. Lett. 81 (22) (1998) 4867.
[254] A. Tremaine, X. Wang, M. Babzien, I. Ben-Zvi, M. Cornacchia, H.-D. Nuhn, R. Malone, A. Murokh, C. Pellegrini, S. Reiche, et al., Experimental characterization of nonlinear harmonic radiation from a visible self-amplified spontaneous emission free-electron laser at saturation, Phys. Rev. Lett. 88 (20) (2002) 204801.
[255] A. Murokh, R. Agustsson, M. Babzien, I. Ben-Zvi, L. Bertolini, K. van Bibber, R. Carr, M. Cornacchia, P. Frigola, J. Hill, et al., Properties of the ultrashort gain length, self-amplified spontaneous emission free-electron laser in the linear regime and saturation, Phys. Rev. E 67 (6) (2003) 066501.
[256] S. Milton, E. Gluskin, S. Biedron, R. Dejus, P. Den Hartog, J. Galayda, K.-J. Kim, J. Lewellen, E. Moog, V. Sajaev, et al., Observation of self-amplified spontaneous emission and exponential growth at 530 nm, Phys. Rev. Lett. 85 (5) (2000) 988.
[257] S. Milton, E. Gluskin, N. Arnold, C. Benson, W. Berg, S. Biedron, M. Borland, Y.-C. Chae, R. Dejus, P. Den Hartog, B. Deriy, M. Erdmann, Y. Eidelman, M. Hahne, Z. Huang, K.-J. Kim, J. Lewellen, Y. Li, A. Lumpkin, O. Makarov, E. Moog, A. Massiri, V. Sajaev, R. Soliday, B. Tieman, E. Trakhtenberg, G. Travish, I. Vasserman, N. Vinokurov, X. Wang, G. Wiemerslage, B. Yang, Exponential gain and saturation of a self-amplified spontaneous emission free-electron laser, Science 292 (5524) (2001) 2037–2041.

[258] J. Andruszkow, B. Aune, V. Ayvazyan, N. Baboi, R. Bakker, V. Balakin, D. Barni, A. Bazhan, M. Bernard, A. Bosotti, J. Bourdon, W. Brefeld, R. Brinkmann, S. Buhler, J.-P. Carneiro, M. Castellano, P. Castro, L. Catani, S. Chel, Y. Cho, S. Choroba, E. Colby, W. Decking, P. Den Hartog, M. Desmons, M. Dohlus, D. Edwards, H. Edwards, B. Faatz, J. Feldhaus, M. Ferrario, M. Fitch, K. Flöttmann, M. Fouaidy, A. Gamp, T. Garvey, C. Gerth, M. Geitz, E. Gluskin, V. Gretchko, U. Hahn, W. Hartung, D. Hubert, M. Hüning, R. Ischebek, M. Jablonka, J. Joly, M. Juillard, T. Junquera, P. Jurkiewicz, A. Kabel, J. Kahl, H. Kaiser, T. Kamps, V. Katelev, J. Kirchgessner, M. Körfer, L. Kravchuk, G. Kreps, J. Krzywinski, T. Lokajczyk, R. Lange, B. Leblond, M. Leenen, J. Lesrel, M. Liepe, A. Liero, T. Limberg, R. Lorenz, L.H. Hua, L.F. Hai, C. Magne, M. Maslov, G. Materlik, A. Matheisen, J. Menzel, P. Michelato, W.-D. Möller, A. Mosnier, U.-C. Müller, O. Napoly, A. Novokhatski, M. Omeich, H. Padamsee, C. Pagani, F. Peters, B. Petersen, P. Pierini, J. Pflüger, P. Piot, B. Phung Ngoc, L. Plucinski, D. Proch, K. Rehlich, S. Reiche, D. Reschke, I. Reyzl, J. Rosenzweig, J. Rossbach, S. Roth, E. Saldin, W. Sandner, Z. Sanok, H. Schlarb, G. Schmidt, P. Schmüser, J. Schneider, E. Schneidmiller, H.-J. Schreiber, S. Schreiber, P. Schütt, J. Sekutowicz, L. Serafini, D. Sertore, S. Setzer, S. Simrock, B. Sonntag, B. Sparr, F. Stephan, V. Sytchev, S. Tazzari, F. Tazzioli, M. Tigner, M. Timm, M. Tonutti, E. Trakhtenberg, R. Treusch, D. Trines, V. Verzilov, T. Vielitz, V. Vogel, G.v. Walter, R. Wanzenberg, T. Weiland, H. Weise, J. Weisend, M. Wendt, M. Werner, M.M. White, I. Will, S. Wolff, M. Yurkov, K. Zapfe, P. Zhogolev, F. Zhou, First observation of self-amplified spontaneous emission in a free-electron laser at 109 nm wavelength, Phys. Rev. Lett. 85 (2000) 3825–3829, http://dx.doi.org/10.1103/PhysRevLett.85.3825, URL http://link.aps.org/doi/10.1103/PhysRevLett.85.3825.

[259] V. Ayvazyan, N. Baboi, I. Bohnet, R. Brinkmann, M. Castellano, P. Castro, L. Catani, S. Choroba, A. Cianchi, M. Dohlus, et al., A new powerful source for coherent VUV radiation: Demonstration of exponential growth and saturation at the TTF free-electron laser, Eur. Phys. J. D 20 (1) (2002) 149–156.

[260] V. Ayvazyan, N. Baboi, I. Bohnet, R. Brinkmann, M. Castellano, P. Castro, L. Catani, S. Choroba, A. Cianchi, M. Dohlus, H. Edwards, B. Faatz, A. Fateev, J. Feldhaus, K. Flöttmann, A. Gamp, T. Garvey, H. Genz, C. Gerth, V. Gretchko, B. Grigoryan, U. Hahn, C. Hessler, K. Honkavaara, M. Hüning, R. Ischebeck, M. Jablonka, T. Kamps, M. Körfer, M. Krassilnikov, J. Krzywinski, M. Liepe, A. Liero, T. Limberg, H. Loos, M. Luong, C. Magne, J. Menzel, P. Michelato, M. Minty, U.-C. Müller, D. Nölle, A. Novokhatski, C. Pagani, F. Peters, J. Pflüger, P. Piot, L. Plucinski, K. Rehlich, I. Reyzl, A. Richter, J. Rossbach, E. Saldin, W. Sandner, H. Schlarb, G. Schmidt, P. Schmüser, J. Schneider, E. Schneidmiller, H.-J. Schreiber, S. Schreiber, D. Sertore, S. Setzer, S. Simrock, R. Sobierajski, B. Sonntag, B. Steeg, F. Stephan, K. Sytchev, K. Tiedtke, M. Tonutti, R. Treusch, D. Trines, D. Türke, V. Verzilov, R. Wanzenberg, T. Weiland, H. Weise, M. Wendt, I. Will, S. Wolff, K. Wittenburg, M. Yurkov, K. Zapfe, Generation of GW radiation pulses from a VUV free-electron laser operating in the femtosecond regime, Phys. Rev. Lett. 88 (2002) 104802, http://dx.doi.org/10.1103/PhysRevLett.88.104802, URL http://link.aps.org/doi/10.1103/PhysRevLett.88.104802.

[261] T. Shintake, H. Tanaka, T. Hara, T. Tanaka, K. Togawa, M. Yabashi, Y. Otake, Y. Asano, T. Bizen, T. Fukui, S. Goto, A. Higashiya, T. Hirono, N. Hosoda, T. Inagaki, S. Inoue, M. Ishii, Y. Kim, H. Kimura, M. Kitamura, T. Kobayashi, H. Maesaka, T. Masuda, S. Matsui, T. Matsushita, X. Maréchal, M. Nagasono, H. Ohashi, T. Ohata, T. Ohshima, K. Onoe, K. Shirasawa, T. Takagi, S. Takahashi, M. Takeuchi, K. Tamasaku, R. Tanaka, Y. Tanaka, T. Tanikawa, T. Togashi, S. Wu, A. Yamashita, K. Yanagida, C. Zhang, H. Kitamura, T. Ishikawa, A compact free-electron laser for generating coherent radiation in the extreme ultraviolet region, Nat. Photonics 2 (9) (2008) 555–559.

[262] T. Shintake, H. Tanaka, T. Hara, T. Tanaka, K. Togawa, M. ÄÄ, Y. Otake, Y. Asano, T. Fukui, T. Hasegawa, et al., Stable operation of a self-amplified spontaneous-emission free-electron laser in the extremely ultraviolet region, Phys. Rev. Special Top. Accelerators Beams 12 (7) (2009) 070701.

[263] S. Schreiber, et al., First Lasing in the Water Window with 4.1 nm at FLASH, in: Proceeding of FEL, 2011.

[264] P. Emma, R. Akre, J. Arthur, R. Bionta, C. Bostedt, J. Bozek, A. Brachmann, P. Bucksbaum, R. Coffee, F.-J. Decker, Y. Ding, D. Dowell, S. Edstrom, A. Fisher, J. Frisch, S. Gilevich, J. Hastings, G. Hays, P. Hering, Z. Huang, R. Iverson, H. Loos, M. Messerschmidt, A. Miahnahri, S. Moeller, H.-D. Nuhn, G. Pile, D. Ratner, J. Rzepiela, D. Schultz, T. Smith, P. Stefan, H. Tompkins, J. Turner, J. Welch, W. White, J. Wu, G. Yocky, J. Galayda, First lasing and operation of an ångstrom-wavelength free-electron laser, Nat. Photonics 4 (9) (2010) 641–647.

[265] T. Ishikawa, H. Aoyagi, T. Asaka, Y. Asano, N. Azumi, T. Bizen, H. Ego, K. Fukami, T. Fukui, Y. Furukawa, S. Goto, H. Hanaki, T. Hara, T. Hasegawa, T. Hatsui, A. Higashiya, T. Hirono, N. Hosoda, M. Ishii, T. Inagaki, Y. Inubushi, T. Itoga, Y. Joti, M. Kago, T. Kameshima, H. Kimura, Y. Kirihara, A. Kiyomichi, T. Kobayashi, C. Kondo, T. Kudo, H. Maesaka, X. Maréchal, T. Masuda, S. Matsubara, T. Matsumoto, T. Matsushita, S. Matsui, M. Nagasono, N. Nariyama, H. Ohashi, T. Ohata, T. Ohshima, S. Ono, Y. Otake, C. Saji, T. Sakurai, T. Sato, K. Sawada, T. Seike, K. Shirasawa, T. Sugimoto, S. Suzuki, S. Takahashi, H. Takebe, K. Takeshita, K. Tamasaku, H. Tanaka, R. Tanaka, T. Tanaka, T. Togashi, K. Togawa, A. Tokuhisa, H. Tomizawa, K. Tono, S. Wu, M. Yabashi, M. Yamaga, A. Yamashita, K. Yanagida, C. Zhang, T. Shintake, H. Kitamura, N. Kumagai, A compact X-ray free-electron laser emitting in the sub-angstrom region, Nat. Photonics 6 (8) (2012) 540–544.

[266] H.-S. Kang, C.-K. Min, H. Heo, C. Kim, H. Yang, G. Kim, I. Nam, S.Y. Baek, H.-J. Choi, G. Mun, et al., Hard X-ray free-electron laser with femtosecond-scale timing jitter, Nat. Photonics 11 (2017) 708.

[267] C.J. Milne, T. Schietinger, M. Aiba, A. Alarcon, J. Alex, A. Anghel, V. Arsov, C. Beard, P. Beaud, S. Bettoni, et al., Swissfel: The swiss X-ray free electron laser, Appl. Sci. 7 (7) (2017) 720.

[268] H. Weise, The European XFEL—Status and commissioning, CERN Yellow Rep. Sch. Proc. 1 (2018) 597.

[269] C. Bostedt, S. Boutet, D.M. Fritz, Z. Huang, H.J. Lee, H.T. Lemke, A. Robert, W.F. Schlotter, J.J. Turner, G.J. Williams, Linac coherent light source: The first five years, Rev. Modern Phys. 88 (1) (2016) 015007.

[270] Y. Ding, A. Brachmann, F.-J. Decker, D. Dowell, P. Emma, J. Frisch, S. Gilevich, G. Hays, P. Hering, Z. Huang, R. Iverson, H. Loos, A. Miahnahri, H.-D. Nuhn, D. Ratner, J. Turner, J. Welch, W. White, J. Wu, Measurements and simulations of ultralow emittance and ultrashort electron beams in the linac coherent light source, Phys. Rev. Lett. 102 (25) (2009) 254801–254805.

[271] E.L. Saldin, E.A. Schneidmiller, M. Yurkov, Statistical properties of radiation from VUV and X-ray free electron laser, Opt. Commun. 148 (4) (1998) 383–403.

[272] S. Reiche, P. Musumeci, C. Pellegrini, J. Rosenzweig, Development of ultra-short pulse, single coherent spike for SASE X-ray FELs, Nucl. Instrum. Methods Phys. Res. A 593 (1) (2008) 45–48.

[273] L. Giannessi, A. Bacci, M. Bellaveglia, F. Briquez, M. Castellano, E. Chiadroni, A. Cianchi, F. Ciocci, M. Couprie, L. Cultrera, G. Dattoli, D. Filippetto, M. Del Franco, G. Di Pirro, M. Ferrario, L. Ficcadenti, F. Frassetto, A. Gallo, G. Gatti, M. Labat, G. Marcus, M. Moreno, A. Mostacci, E. Pace, A. Petralia, V. Petrillo, L. Poletto, M. Quattromini, J. Rau, C. Ronsivalle, J. Rosenzweig, A. Rossi, V. Rossi Albertini, E. Sabia, M. Serluca, S. Spampinati, I. Spassovsky, B. Spataro, V. Surrenti, C. Vaccarezza, C. Vicario, Self-amplified spontaneous emission free-electron laser with an energy-chirped electron beam and undulator tapering, Phys. Rev. Lett. 106 (2011) 144801.

[274] Z. Huang, K.-J. Kim, Three-dimensional analysis of harmonic generation in high-gain free-electron lasers, Phys. Rev. E 62 (5) (2000) 7295.

[275] G. Dattoli, P. Ottaviani, S. Pagnutti, Nonlinear harmonic generation in high-gain free-electron lasers, J. Appl. Phys. 97 (11) (2005) 113102.

[276] G. Dattoli, P. Ottaviani, S. Pagnutti, Pulse propagation and nonlinear harmonic generation in free electron laser oscillators, J. Appl. Phys. 101 (2) (2007) 024914.

[277] L.H. Yu, Generation of intense UV radiation by subharmonically seeded single-pass free-electron lasers, Phys. Rev. A 44 (8) (1991) 5178.

[278] L.H. Yu, J. Wu, Theory of high gain harmonic generation: An analytical estimate, Nucl. Instrum. Methods Phys. Res. A 483 (1) (2002) 493–498.

[279] I. Ben-Zvi, K. Yang, L. Yu, The "fresh-bunch" technique in FELs, Nucl. Instrum. Methods Phys. Res. A 318 (1–3) (1992) 726–729.

[280] L.-H. Yu, M. Babzien, I. Ben-Zvi, L. DiMauro, A. Doyuran, W. Graves, E. Johnson, S. Krinsky, R. Malone, I. Pogorelsky, J. Skaritka, G. Rakowsky, L. Solomon, X. Wang, M. Woodle, V. Yakimenko, S. Biedron, J. Galayda, E. Gluskin, J. Jagger, V. Sajaev, I. Vasserman, High-gain harmonic-generation free-electron laser, Science 289 (5481) (2000) 932–934.

[281] G. Lambert, T. Hara, D. Garzella, T. Tanikawa, M. Labat, B. Carre, H. Kitamura, T. Shintake, M. Bougeard, S. Inoue, Y. Tanaka, P. Salieres, H. Merdji, O. Chubar, O. Gobert, K. Tahara, M.-E. Couprie, Injection of harmonics generated in gas in a free-electron laser providing intense and coherent extreme-ultraviolet light, Nat. Phys. 4 (4) (2008) 296–300.
[282] M. Labat, M. Bellaveglia, M. Bougeard, B. Carré, F. Ciocci, E. Chiadroni, A. Cianchi, M. Couprie, L. Cultrera, M. Del Franco, et al., High-gain harmonic-generation free-electron laser seeded by harmonics generated in gas, Phys. Rev. Lett. 107 (22) (2011) 224801.
[283] T. Togashi, E.J. Takahashi, K. Midorikawa, M. Aoyama, K. Yamakawa, T. Sato, A. Iwasaki, S. Owada, T. Okino, K. Yamanouchi, et al., Extreme ultraviolet free electron laser seeded with high-order harmonic of ti: sapphire laser, Opt. Express 19 (1) (2011) 317–324.
[284] S. Ackermann, A. Azima, S. Bajt, J. Bödewadt, F. Curbis, H. Dachraoui, H. Delsim-Hashemi, M. Drescher, S. Düsterer, B. Faatz, et al., Generation of coherent 19-and 38-nm radiation at a free-electron laser directly seeded at 38 nm, Phys. Rev. Lett. 111 (11) (2013) 114801.
[285] E. Allaria, C. Callegari, D. Cocco, W.M. Fawley, M. Kiskinova, C. Masciovecchio, F. Parmigiani, The fermi@ elettra free-electron-laser source for coherent X-ray physics: photon properties, beam transport system and applications, New J. Phys. 12 (7) (2010) 075002.
[286] E. Allaria, R. Appio, L. Badano, W. Barletta, S. Bassanese, S. Biedron, A. Borga, E. Busetto, D. Castronovo, P. Cinquegrana, et al., Highly coherent and stable pulses from the FERMI seeded free-electron laser in the extreme ultraviolet, Nat. Photonics 6 (10) (2012) 699–704.
[287] E. Allaria, R. Appio, L. Badano, W. Barletta, S. Bassanese, S. Biedron, A. Borga, E. Busetto, D. Castronovo, P. Cinquegrana, S. Cleva, D. Cocco, M. Cornacchia, P. Craievich, I. Cudin, G. D'Auria, M. Dal Forno, M. Danailov, R. De Monte, G. De Ninno, P. Delgiusto, A. Demidovich, S. Di Mitri, B. Diviacco, A. Fabris, R. Fabris, W. Fawley, M. Ferianis, E. Ferrari, S. Ferry, L. Froehlich, P. Furlan, G. Gaio, F. Gelmetti, L. Giannessi, M. Giannini, R. Gobessi, R. Ivanov, E. Karantzoulis, M. Lonza, A. Lutman, B. Mahieu, M. Milloch, S. Milton, M. Musardo, I. Nikolov, S. Noe, F. Parmigiani, G. Penco, M. Petronio, L. Pivetta, M. Predonzani, F. Rossi, L. Rumiz, A. Salom, C. Scafuri, C. Serpico, P. Sigalotti, S. Spampinati, C. Spezzani, M. Svandrlik, C. Svetina, S. Tazzari, M. Trovo, R. Umer, A. Vascotto, M. Veronese, R. Visintini, M. Zaccaria, D. Zangrando, M. Zangrando, Highly coherent and stable pulses from the FERMI seeded free-electron laser in the extreme ultraviolet, Nat. Photonics 6 (10) (2012) 699–704.
[288] G. Wang, Commissioning status of the dalian coherent light source, in: 8th Int. Particle Accelerator Conf.(IPAC'17), Copenhagen, Denmark, 14â 19 May, 2017, JACOW, Geneva, Switzerland, 2017, pp. 2709–2712.
[289] J. Feldhaus, E. Saldin, J. Schneider, E. Schneidmiller, M. Yurkov, Possible application of X-ray optical elements for reducing the spectral bandwidth of an X-ray SASE FEL, Opt. Commun. 140 (4) (1997) 341–352.
[290] G. Geloni, V. Kocharyan, E. Saldin, A novel self-seeding scheme for hard X-ray FELs, J. Modern Opt. 58 (16) (2011) 1391–1403.
[291] J. Amann, W. Berg, V. Blank, F.-J. Decker, Y. Ding, P. Emma, Y. Feng, J. Frisch, D. Fritz, J. Hastings, Z. Huang, J. Krzywinski, R. Lindberg, H. Loos, A. Lutman, H.-D. Nuhn, D. Ratner, J. Rzepiela, D. Shu, Y. Shvyd'ko, S. Spampinati, S. Stoupin, S. Terentyev, E. Trakhtenberg, D. Walz, J. Welch, J. Wu, A. Zholents, D. Zhu, Demonstration of self-seeding in a hard-X-ray free-electron laser, Nat. Photonics 6 (10) (2012) 693–698.
[292] D. Ratner, R. Abela, J. Amann, C. Behrens, D. Bohler, G. Bouchard, C. Bostedt, M. Boyes, K. Chow, D. Cocco, et al., Experimental demonstration of a soft X-ray self-seeded free-electron laser, Phys. Rev. Lett. 114 (5) (2015) 054801.
[293] M. Yabashi, T. Tanaka, X-RAys: Self-seeded FEL emits hard X-rays, Nat. Photonics 6 (10) (2012) 648–649.
[294] G. Stupakov, Using the beam-echo effect for generation of short-wavelength radiation, Phys. Rev. Lett. 102 (7) (2009) 074801–074804.
[295] D. Xiang, E. Colby, M. Dunning, S. Gilevich, C. Hast, K. Jobe, D. McCormick, J. Nelson, T. Raubenheimer, K. Soong, G. Stupakov, Z. Szalata, D. Walz, S. Weathersby, M. Woodley, Demonstration of the echo-enabled harmonic generation technique for short-wavelength seeded free electron lasers, Phys. Rev. Lett. 105 (11) (2010) 114801–114804.
[296] Z. Zhao, D. Wang, J. Chen, Z. Chen, H. Deng, J. Ding, C. Feng, Q. Gu, M. Huang, T. Lan, L. YB, D. Li, G. Lin, B. Liu, E. Prat, X. Wang, Z. Wang, K. Ye, L. Yu, H. Zhang, J. Zhang, M. Zhang, M. Zhang, T. Zhang, S. Zhong, Q. Zhou, First lasing of an echo-enabled harmonic generation free-electron laser, Nat. Photonics 6 (6) (2012) 360–363.
[297] E. Hemsing, M. Dunning, C. Hast, T. Raubenheimer, S. Weathersby, D. Xiang, Highly coherent vacuum ultraviolet radiation at the 15th harmonic with echo-enabled harmonic generation technique, Phys. Rev. Special Top. Accelerators Beams 17 (7) (2014) 070702.
[298] E. Hemsing, M. Dunning, B. Garcia, C. Hast, T. Raubenheimer, G. Stupakov, D. Xiang, Echo-enabled harmonics up to the 75th order from precisely tailored electron beams, Nat. Photonics (2016).
[299] P. Rebernik Ribič, E. Roussel, G. Penn, G. De Ninno, L. Giannessi, G. Penco, E. Allaria, Echo-enabled harmonic generation studies for the FERMI free-electron laser, in: Photonics, 4, (1) Multidisciplinary Digital Publishing Institute, 2017, p. 19.
[300] P.R. Ribič, A. Abrami, L. Badano, M. Bossi, H.-H. Braun, N. Bruchon, F. Capotondi, D. Castronovo, M. Cautero, P. Cinquegrana, et al., Coherent soft X-ray pulses from an echo-enabled harmonic generation free-electron laser, Nat. Photonics (2019) 1.
[301] H. Al Abawi, F. Hopf, P. Meystre, Electron dynamics in a free-electron laser, Phys. Rev. A 16 (2) (1977) 666.
[302] W.B. Colson, Free electron laser theory., Tech. Rep., BERKELEY RESEARCH ASSOCIATES INC CA, 1986.
[303] A. Bambini, A. Renieri, The free electron laser: A single particle classical model, in: Coherence in Spectroscopy and Modern Physics, Springer, 1978, pp. 361–379.
[304] P. Sprangle, V. Granatstein, Stimulated cyclotron resonance scattering and production of powerful submillimeter radiation, Appl. Phys. Lett. 25 (7) (1974) 377–379.
[305] P. Sprangle, V. Granatstein, L. Baker, Stimulated collective scattering from a magnetized relativistic electron beam, Phys. Rev. A 12 (4) (1975) 1697.
[306] F. Hopf, P. Meystre, M. Scully, W. Louisell, Classical theory of a free-electron laser, Phys. Rev. Lett. 37 (18) (1976) 1215.
[307] F. Hopf, P. Meystre, M. Scully, W. Louisell, Strong-signal theory of a free-electron laser, Phys. Rev. Lett. 37 (20) (1976) 1342.
[308] N.M. Kroll, W.A. McMullin, Stimulated emission from relativistic electrons passing through a spatially periodic transverse magnetic field, Phys. Rev. A 17 (1) (1978) 300.
[309] Y.S. Derbenev, A. Kondratenko, E. Saldin, On the possibility of using a free electron laser for polarization of electrons in storage rings, Nucl. Instrum. Methods Phys. Res. 193 (3) (1982) 415–421.
[310] R. Bonifacio, F. Casagrande, G. Casati, Cooperative and chaotic transition of a free electron laser Hamiltonian model, Opt. Commun. 40 (3) (1982) 219–223.
[311] G. Dattoli, T. Letardi, A. Renieri, J. Madey, Limits on the single-pass higher harmonics FEL operation, IEEE J. Quantum Electron. 20 (1984) 1003–1005, http://dx.doi.org/10.1109/JQE.1984.1072516.
[312] W. Colson, J. Gallardo, P. Bosco, Free-electron-laser gain degradation and electron-beam quality, Phys. Rev. A 34 (1986) 4875–4881, http://dx.doi.org/10.1103/PhysRevA.34.4875.
[313] G. Dattoli, A. Renieri, A. Torre, R. Caloi, Inhomogeneous broadening effects in high-gain free electron laser operation: A simple parametrization, Il Nuovo Cimento D 11 (1989) 393–404, http://dx.doi.org/10.1007/BF02450989.
[314] M. Xie, Design optimization for an X-ray free electron laser driven by slac linac, in: Proceedings Particle Accelerator Conference, 1, IEEE, 1995, pp. 183–185.
[315] G. Dattoli, L. Giannessi, P. Ottaviani, C. Ronsivalle, Semi-analytical model of self-amplified spontaneous-emission free-electron lasers, including diffraction and pulse-propagation effects, J. Appl. Phys. 95 (2004) 3206–3210, http://dx.doi.org/10.1063/1.1645979.
[316] G. Dattoli, P. Ottaviani, S. Pagnutti, Booklet of FEL design, 2007, http://fel.enea.it/booklet/pdf/Booklet_for_FEL_design.pdf.
[317] M. Artioli, G. Dattoli, http://fel.enea.it/booklet/live/index.html, 2016.
[318] W. Colson, C. Pellegrini, A. Renieri, Classical free electron laser theory, Laser Handb. 6 (115) (1990) 75.

[319] G. Dattoli, A. Renieri, A. Torre, Lectures on the Free Electron Laser Theory and Related Topics, World Scientific, 1993.
[320] G. Dattoli, A. Torre, C. Centioli, M. Richetta, Free-electron laser operation in the intermediate gain region, IEEE J. Quantum Electron. 25 (11) (1989) 2327–2331.
[321] M. Artioli, G. Dattoli, S. Licciardi, S. Pagnutti, Fractional derivatives, memory kernels and solution of a free electron laser volterra type equation, Mathematics 5 (4) (2017) 73.
[322] C.-C. Shih, A. Yariv, Single-electron analysis of the space-charge effect in free-electron lasers, Phys. Rev. A 22 (6) (1980) 2717.
[323] C.-C. Shih, A. Yariv, Inclusion of space-charge effects with maxwell's equations in the single-particle analysis of free-electron lasers, IEEE J. Quantum Electron. 17 (8) (1981) 1387–1394.
[324] W. Colson, The nonlinear wave equation for higher harmonics in free-electron lasers, IEEE J. Quantum Electron. 17 (8) (1981) 1417–1427.
[325] P. Sprangle, C.-M. Tang, W. Manheimer, Nonlinear formulation and efficiency enhancement of free-electron lasers, Phys. Rev. Lett. 43 (26) (1979) 1932.
[326] P. Sprangle, C.-M. Tang, W. Manheimer, Nonlinear theory of free-electron lasers and efficiency enhancement, Phys. Rev. A 21 (1) (1980) 302.
[327] D.B. McDermott, T. Marshall, The collective free-electron laser, in: Free-Electron Generators of Coherent Radiation, 1980, pp. 509–522.
[328] A. Gover, Z. Livni, Operation regimes of cerenkov-smith-purcell free electron lasers and tw amplifiers, Opt. Commun. 26 (3) (1978) 375–380.
[329] E. Saldin, E. Schneidmiller, M. Yurkov, Method for calculating the space charge effects in a free electron laser, Opt. Commun. 103 (3–4) (1993) 205–210.
[330] G. Marcus, E. Hemsing, J. Rosenzweig, Gain length fitting formula for free-electron lasers with strong space-charge effects, Phys. Rev. Special Top. Accelerators Beams 14 (8) (2011) 080702.
[331] G. Dattoli, H. Fares, S. Licciardi, Space charge and quantum corrections in free electron laser evolution, 2020, arXiv preprint arXiv:2003.09637.
[332] I. Zagorodnov, M. Dohlus, S. Tomin, Accelerator beam dynamics at the European X-ray free electron laser, Phys. Rev. Accel. Beams 22 (2) (2019) 024401.
[333] R. Bonifacio, L. De Salvo, P. Pierini, N. Piovella, C. Pellegrini, Spectrum, temporal structure, and fluctuations in a high-gain free-electron laser starting from noise, Phys. Rev. Lett. 73 (1) (1994) 70.
[334] L. Chapon, I. Boscaro-Clarke, A. Dent, A. Harrison, M. Launchbury, D. Stuart, R. Walker (Eds.), Diamond-II Conceptual Design Report, Diamond Light Source Ltd, 2019.
[335] J. Ablett, A. Ackerman, R. Alforque, M. Allaire, D. Arena, A. Baron, B. Deborah, R. Beauman, J. Beebe-Wang, J. Bengtsson, et al., Nsls-II, conceptual design report, Tech. Rep., Brookhaven National Laboratory, Upton, NY, 2006.
[336] Linac Coherent Light Source II Conceptual Design Report, SLAC National Accelerator Laboratory, 2011.
[337] J.e.a. Arthur, Linac Coherent Light Source Conceptual Design Report, SLAC National Accelerator Laboratory, 2002.
[338] S. Kim, R. Wehrle, L. Genens, Vacuum chamber for an undulator straight section, in: Proceedings, 1987 IEEE Particle Accelerator Conference (PAC 1987): Washington DC, USA, Mar 16-19, 1987, pp. 1625.
[339] L. Nadolski, Between model and reality, Part II, in: Proceedings, CERN Accelerator School Beam Diagnostics, Dourdan, France, 2008, pp. 229.
[340] M.e.a. Altarelli (Ed.), The European X-Ray Free-Electron Laser Technical design report, Deutsches Elektronen-Synchrotron, 2007.
[341] J. Clarke, The Science and Technology of Undulators and Wigglers, Oxford University Press, 2004.
[342] T. Tanaka, Universal representation of undulator phase errors, Phys. Rev. Accel. Beams 21 (11) (2018) 110704.
[343] R.P. Walker, Phase errors and their effect on undulator radiation properties, Phys. Rev. Special Top. Accelerators Beams 16 (1) (2013) 010704.
[344] T. Hara, T. Tanaka, T. Tanabe, X.-M. Maréchal, H. Kitamura, P. Elleaume, B. Morrison, J. Chavanne, P. Van Vaerenbergh, D. Schmidt, Spring-8 in-vacuum undulator beam test at the ESRF, J. Synchrotron Radiat. 5 (3) (1998) 406–408.
[345] J. Pflüger, B. Faatz, M. Tischer, T. Vielitz, Radiation exposure and magnetic performance of the undulator system for the VUV fel at the TESLA test facility phase-1 after 3 years of operation, Nucl. Instrum. Methods Phys. Res. A 507 (1–2) (2003) 186–190.
[346] H. Nuhn, C. Field, S. Mao, Y. Levashov, M. Santana, J. Welch, Z. Wolf, Undulator radiation damage experience at LCLS, Tech. Rep., SLAC National Accelerator Lab., Menlo Park, CA (United States), 2015.
[347] H. Winick, K. Bane, R. Boyce, G. Loew, P. Morton, H.-D. Nuhn, J. Paterson, P. Pianetta, T. Raubenheimer, J. Seeman, et al., A 2-4 nm linac coherent light source (LCLS) using the SLAC linac, in: Particle Accelerator Conference, 1993., Proceedings of the 1993, IEEE, 1993, pp. 1445–1447.
[348] K. Halbach, Physical and optical properties of rare earth cobalt magnets, Nucl. Instrum. Methods Phys. Res. 187 (1) (1981) 109–117.
[349] K. Halbach, Permanent magnet undulators, Le J. de Physique Colloques 44 (C1) (1983) C1–211.
[350] K. Halbach, Application of permanent magnets in accelerators and electron storage rings, J. Appl. Phys. 57 (8) (1985) 3605–3608.
[351] O. Chubar, P. Elleaume, J. Chavanne, A three-dimensional magnetostatics computer code for insertion devices, J. Synchrotron Radiat. 5 (3) (1998) 481–484.
[352] W. Gudat, J. Pflüger, J. Chatzipetros, W. Peatman, An undulator/multipole wiggler for the BESSY storage ring, Nucl. Instrum. Methods Phys. Res. A 246 (1–3) (1986) 50–53.
[353] T. Tanaka, T. Hara, R. Tsuru, D. Iwaki, X. Marechal, T. Bizen, T. Seike, H. Kitamura, In-vacuum undulators, in: Proceedings of the 27th International Free Electron Conference, 2005, 370–377.
[354] S. Yamamoto, T. Shioya, M. Hara, H. Kitamura, X.W. Zhang, T. Mochizuki, H. Sugiyama, M. Ando, Construction of an in-vacuum type undulator for production of undulator x rays in the 5–25 kev region, Rev. Sci. Instrum. 63 (1) (1992) 400–403.
[355] T. Eichner, F. Grüner, S. Becker, M. Fuchs, D. Habs, R. Weingartner, U. Schramm, H. Backe, P. Kunz, W. Lauth, Miniature magnetic devices for laser-based, table-top free-electron lasers, Phys. Rev. Special Top. Accelerators Beams 10 (8) (2007) 082401.
[356] R. Kersevan, M. Hahn, I. Parat, D. Schmied, Machine operation issue related to the vacuum system of the ESRF, in: EPAC08, 2008, pp. 3705.
[357] T. Hara, T. Tanaka, T. Tanabe, X.-M. Maréchal, S. Okada, H. Kitamura, In-vacuum undulators of spring-8, J. Synchrotron Radiat. 5 (3) (1998) 403–405.
[358] J.M.D. Coey, Rare-Earth Iron Permanent Magnets, (54) Oxford University Press, 1996.
[359] S. Pan, The first generation rare earth permanent-magnet alloys, in: Rare Earth Permanent-Magnet Alloys' High Temperature Phase Transformation, Springer, 2013, pp. 27–93.
[360] D. Givord, H. Li, R.P. De La Bâthie, Magnetic properties of Y2fe14b and Nd2Fe14B single crystals, Solid State Commun. 51 (11) (1984) 857–860.
[361] M. Sagawa, S. Hirosawa, H. Yamamoto, S. Fujimura, Y. Matsuura, Nd–fe–b permanent magnet materials, Japan. J. Appl. Phys. 26 (6R) (1987) 785.
[362] T. Bizen, Y. Asano, T. Hara, X. Marechal, T. Seike, T. Tanaka, H. Lee, D. Kim, C. Chung, H. Kitamura, Baking effect for NdFeB magnets against demagnetization induced by high-energy electrons, Nucl. Instrum. Methods Phys. Res. A 515 (3) (2003) 850–852.
[363] T. Bizen, Y. Asano, X.-M. Maréchal, T. Seike, T. Aoki, K. Fukami, N. Hosoda, H. Yonehara, T. Takagi, T. Hara, et al., High-energy electron irradiation of NdFeB permanent magnets: Dependence of radiation damage on the electron energy, Nucl. Instrum. Methods Phys. Res. A 574 (3) (2007) 401–406.
[364] S. Yamamoto, Undulator development towards very short period lengths, Synchrotron Radiat. News 28 (3) (2015) 19–22.
[365] S. Yamamoto, Development of undulator magnets towards very short period lengths, in: AIP Conference Proceedings, 1741, (1) AIP Publishing, 2016, 020029.

[366] T. Hara, T. Tanaka, H. Kitamura, T. Bizen, X. Maréchal, T. Seike, T. Kohda, Y. Matsuura, Cryogenic permanent magnet undulators, Phys. Rev. Special Top. Accelerators Beams 7 (5) (2004) 050702.
[367] J. Bahrdt, E. Gluskin, Cryogenic permanent magnet and superconducting undulators, Nucl. Instrum. Methods Phys. Res. A 907 (2018) 149–168.
[368] D. Dufeu, P. Lethuillier, High sensitivity 2 t vibrating sample magnetometer, Rev. Sci. Instrum. 70 (7) (1999) 3035–3039.
[369] C. Benabderrahmane, P. Berteaud, M. Valléau, C. Kitegi, K. Tavakoli, N. Béchu, A. Mary, J. Filhol, M. Couprie, Nd2fe14b and Pr2Fe14B magnets characterisation and modelling for cryogenic permanent magnet undulator applications, Nucl. Instrum. Methods Phys. Res. A 669 (2012) 1–6.
[370] M.-E. Couprie, F. Briquez, G. Sharma, C. Benabderrahmane, F. Marteau, O. Marcouillé, P. Berteaud, T. El Ajjouri, J. Vétéran, L. Chapuis, et al., Cryogenic undulators, in: Advances in X-Ray Free-Electron Lasers Instrumentation III, 9512, International Society for Optics and Photonics, 2015, 951204.
[371] C. Abache, H. Oesterreicher, Magnetic properties of compounds R2fe14b, J. Appl. Phys. 57 (8) (1985) 4112–4114.
[372] S. Hirosawa, Y. Matsuura, H. Yamamoto, S. Fujimura, M. Sagawa, H. Yamauchi, Magnetization and magnetic anisotropy of R2fe14b measured on single crystals, J. Appl. Phys. 59 (3) (1986) 873–879.
[373] L. García, J. Chaboy, F. Bartolomé, J. Goedkoop, Orbital magnetic moment instability at the spin reorientation transition of $Nd_2Fe_{14}B$, Phys. Rev. Lett. 85 (2) (2000) 429.
[374] H. Hiroyoshi, N. Saito, G. Kido, Y. Nakagawa, S. Hirosawa, M. Sagawa, High-field magnetization of R2fe14b single crystals, J. Magn. Magn. Mater. 54 (1986) 583–584.
[375] D. Goll, M. Seeger, H. Kronmüller, Magnetic and microstructural properties of nanocrystalline exchange coupled PrFeB permanent magnets, J. Magn. Magn. Mater. 185 (1) (1998) 49–60.
[376] M. Couprie, SPIE Optics Optoelectronics, International Society for Optics, 951204.
[377] J. Chavanne, G. Lebec, C. Penel, F. Revol, C. Kitegi, Cryogenic permanent magnet undulators, in: AIP Conference Proceedings, 1234, (1) AIP, 2010, pp. 25–28.
[378] J.-C. Huang, H. Kitamura, C.-K. Yang, C.-H. Chang, C.-H. Chang, C.-S. Hwang, Challenges of in-vacuum and cryogenic permanent magnet undulator technologies, Phys. Rev. Accel. Beams 20 (6) (2017) 064801.
[379] T. Tanaka, T. Seike, H. Kitamura, Measurement of SPring-8 XFEL undulator prototype with the SAFALI system, in: FEL, vol. 8, 2008, pp. 371.
[380] J. Chavanne, M. Hahn, R. Kersevan, C. Kitegi, C. Penel, F. Revol, E.G. France, Construction of a cryogenic permanent magnet undulator at the ESRF, in: EPAC08, Genoa, 2008, pp. 2243–2245.
[381] C. Benabderrahmane, N. Béchu, P. Berteaud, M. Couprie, J. Filhol, C. Herbeaux, C. Kitegi, J. Marlats, K. Tavakoli, M. Valléau, et al., Development of a PrFeB cryogenic undulator at SOLEIL, in: Proceedings of the 1st International Particle Accelerator Conference (IPAC'10), Kyoto, Japan, 2010, pp. 3096–3098.
[382] T. Tanaka, R. Tsuru, T. Nakajima, H. Kitamura, Magnetic characterization for cryogenic permanent-magnet undulators: A first result, J. Synchrotron Radiat. 14 (5) (2007) 416–420.
[383] T. Tanaka, T. Seike, A. Kagamihata, T. Schmidt, A. Anghel, M. Brügger, W. Bulgheroni, B. Jakob, H. Kitamura, In situ correction of field errors induced by temperature gradient in cryogenic undulators, Phys. Rev. Special Top. Accelerators Beams 12 (12) (2009) 120702.
[384] C. Kuhn, H.-J. Baecker, J. Bahrdt, A. Gaupp, B. Schulz, Hall-probe bench for cryogenic in-vacuum-undulators, in: Proceedings of IPAC2013, Shanghai, China, 2013, pp. 2126–2128.
[385] T. Tanabe, O. Chubar, D.A. Harder, M. Lehecka, J. Rank, G. Rakowsky, C. Spataro, Cryogenic field measurement of Pr 2 Fe 14 B undulator and performance enhancement options at the NSLS-II, in: AIP Conference Proceedings, 1234, (1) AIP, 2010, pp. 29–32.
[386] C. Kitegi, P. Cappadoro, O. Chubar, T. Corwin, D. Harder, P. He, H. Fernendez, G. Rakowsky, C. Rhein, J. Rank, et al., Development of a PrFeB cryogenic undulator at NSLS-II, in: Proceedings of IPAC2012, New Orleans, Louisiana, USA, 2012, pp. 762–764.
[387] M. Couprie, C. Benabderrahmane, P. Berteaud, F. Briquez, C. Bourassin-Bouchet, F. Bouvet, L. Cassinari, L. Chapuis, M. Diop, J. Daillant, et al., The status of the LUNEX5 project, in: Proceedings FEL, vol. 14, 2014.
[388] M. Valléau, F. Briquez, A. Ghaith, F. Marteau, O. Marcouillé, C. Kitegi, F. Blache, M.-E. Couprie, Development of cryogenic permanent magnet undulators at SOLEIL, Synchrotron Radiat. News 31 (3) (2018) 42–47.
[389] J. Bahrdt, H. Bäcker, M. Dirsatt, W. Frentrup, A. Gaupp, D. Just, D. Pflückhahn, M. Scheer, B. Schulz, R. Weingartner, et al., Cryogenic design of a prfeb-based undulator, Proc. IPAC (2010) 3111–3113.
[390] C. Kuhn, B. Schulz, J. Bahrdt, M. Scheer, A. Gaupp, Developing of Advanced Magnet Structures for Cryogenic in Vacuum Permanent Magnet Undulators, in: IPAC2014, Dresden, Germany, 2014, pp. 2004–2006.
[391] F. Holy, A. Maier, B. Zeitler, R. Weingartner, S. Raith, N. Kajumba, M. El Ghazaly, W. Lauth, D. Krambrich, A. Gaupp, et al., First spectral measurements of a cryogenic high-field short-period undulator, Phys. Rev. Special Top. Accelerators Beams 17 (5) (2014) 050704.
[392] A. Murokh, V. Solovyov, R. Agustsson, F.H. O'Shea, O. Chubar, Y. Chen, T. Grandsaert II, Textured dysprosium and gadolinium poles for high-field, short-period hybrid undulators, Nucl. Instrum. Methods Phys. Res. A 735 (2014) 521–527.
[393] F. O'Shea, A. Palmowski, E. Spranza, R. Agustsson, Y.-C. Chen, Development of a Short Period Cryogenic Undulator at RadiaBeam, in: Proceedings of NAPAC2016, Chicago, IL, USA, 2017, pp. 995–997.
[394] J. Chavanne, C. Penel, P. Elleaume, Development and operation of a prototype cryogenic permanent magnet undulator at the ESRF, Taylor & Francis, 2009.
[395] J. Chavanne, G. Lebec, C. Penel, F. Revol, C. Kitegi, First operational experience with a cryogenic permanent magnet undulator at the ESRF, in: The 23rd Particle Accelerator Conference, 2009, pp. 2414–2416.
[396] C. Kitegi, J. Chavanne, D. Cognie, P. Elleaume, F. Revol, C. Penel, B. Plan, M. Rossat, Development of a cryogenic permanent magnet in-vacuum undulator at the ESRF, in: Proceedings of EPAC 2006, Edinburgh, Scotland, 2006, pp. 3559–3561.
[397] J. Chavanne, C. Benabderrahmane, G. Le Bec, C. Penel, Recent developments in insertion devices at the ESRF: working toward diffraction-limited storage rings, Synchrotron Radiat. News 28 (3) (2015) 15–18.
[398] T. Schmidt, S. Reiche, Undulators for the SwissFEL, in: Proceedings of the FEL Conference, 2009.
[399] M. Calvi, T. Schmidt, A. Anghel, A. Cervellino, S. Leake, P. Willmott, T. Tanaka, Commissioning results of the U14 cryogenic undulator at SLS, in: Journal of Physics: Conference Series, 425, (3) IOP Publishing, 2013, 032017.
[400] C. Benabderrahmane, M. Valléau, P. Berteaud, K. Tavakoli, J. Marlats, R. Nagaoka, N. Béchu, D. Zerbib, P. Brunelle, L. Chapuis, et al., Development of a 2 m $Pr_2Fe_{14}B$ cryogenic permanent magnet undulator at SOLEIL, in: Journal of Physics: Conference Series, 425, (3) IOP Publishing, 2013, 032019.
[401] M. Valléau, C. Benabderrahmane, F. Briquez, P. Berteaud, K. Tavakoli, D. Zerbib, L. Chapuis, F. Marteau, O. Marcouillé, T. El Ajjouri, et al., Development of cryogenic undulators with PrFeB magnets at SOLEIL, in: AIP Conference Proceedings, 1741, (1) AIP Publishing, 2016, 020024.
[402] C. Benabderrahmane, M. Valléau, A. Ghaith, P. Berteaud, L. Chapuis, F. Marteau, F. Briquez, O. Marcouille, J.-L. Marlats, K. Tavakoli, et al., Development and operation of a Pr 2 Fe 14 B based cryogenic permanent magnet undulator for a high spatial resolution x-ray beam line, Phys. Rev. Accel. Beams 20 (3) (2017) 033201.
[403] A. Ghaith, A. Somogyi, P. Berteaud, M.-E. Couprie, M. Valléau, M. Sebdaoui, N. Béchu, F. Blache, F. Briquez, M. Tilmont, et al., Progress of Pr2Fe14B based hybrid cryogenic undulators at SOLEIL, in: Proceedings of IPAC2017, Copenhagen, Denmark, 2017, pp. 1213–1216.

[404] M. Valléau, P. Berteaud, F. Briquez, P. Brunelle, N. Béchu, M.-E. Couprie, J. Da Silva Castro, J.-M. Dubuisson, A. Ghaith, C. Herbeaux, et al., Construction and optimization of cryogenic undulators at SOLEIL, in: 60th ICFA Advanced Beam Dynamics Workshop on Future Light Sources (FLS'18), Shanghai, China, 5-9 March 2018, JACOW Publishing, Geneva, Switzerland, 2018, pp. 193–198.
[405] A. Ghaith, P. Berteaud, M.-E. Couprie, M. Sebdaoui, N. Béchu, M. Labat, I. Andriyash, F. Briquez, M. Tilmont, C. Herbeaux, et al., Cryogenic Permanent Magnet Undulator for an FEL Application, in: 38th International Free Electron Laser Conference, Santa Fe, NM, USA, 2018, pp. 546–548.
[406] M. Couprie, M. Labat, C. Evain, F. Marteau, F. Briquez, M. Khojoyan, C. Benabderrahmane, L. Chapuis, N. Hubert, C. Bourassin-Bouchet, et al., An application of laser–plasma acceleration: towards a free-electron laser amplification, Plasma Phys. Control. Fusion 58 (3) (2016) 034020.
[407] T. André, I. Andriyash, C. Basset, C. Benabderrahmane, P. Berteaud, S. Bielawski, S. Bonnin, F. Bouvet, F. Briquez, L. Cassinari, et al., First electron beam measurements on COXINEL, in: 7th International Particle Accelerator Conference (IPAC'16), Busan, Korea, 2016, pp. 712–715.
[408] J. Schouten, E. Rial, Electron beam heating and operation of the cryogenic undulator and superconducting wigglers at DIAMOND, in: Proceedings of the 2nd International Particle Accelerator Conference, San SebastiáN, Spain, 2011, p. 3323.
[409] C. Ostenfeld, M. Pedersen, Cryogenic in-vacuum undulator at danfysik, in: Proceedings of IPAC'10, Kyoto, Japan, JACOW, Geneva, Switzerland, 2010, pp. 3093–3095.
[410] J. Bahrdt, C. Kuhn, Cryogenic permanent magnet undulator development at HZB/BESSY II, Synchrotron Radiat. News 28 (2015) 9, http://dx.doi.org/10.1080/08940886.2015.1037673.
[411] J. Bahrdt, H.-J. Bäcker, W. Frentrup, C. Rethfeldt, M. Scheer, B. Schulz, S. Gottschlich, A canted double undulator system with a wide energy range for EMIL, in: Proc. IPAC'15, 2015, pp. 1442–1444.
[412] J. Bahrdt, D. Engel, W. Frentrup, P. Goslawski, P. Kuske, R. Müller, M. Ries, M. Ruprecht, A. Schälicke, Measurements of the lattice modifications for the cryogenic undulator CPMU17, in: 7th International Particle Accelerator Conference (IPAC'16), Busan, Korea, May 8-13, 2016, JACOW, Geneva, Switzerland, 2016, pp. 4031–4034.
[413] J. Bahrdt, W. Frentrup, S. Gottschlich, S. Grimmer, M. Huck, C. Kuhn, A. Meseck, C. Rethfeldt, E. Rial, M. Scheer, et al., Characterization and implementation of the cryogenic permanent magnet undulator CPMU17 at bessy ii, in: 10th Int. Partile Accelerator Conf.(IPAC'19), Melbourne, Australia, 19-24 May 2019, JACOW Publishing, Geneva, Switzerland, 2019, pp. 1415–1418.
[414] J.-C. Huang, H. Kitamura, C.-Y. Kuo, C.-K. Yang, C.-H. Chang, Y.-T. Yu, Y.-Y. Lin, C.-S. Hwang, Design of a magnetic circuit for a cryogenic undulator in Taiwan photon source, in: AIP Conference Proceedings, 1741, (1) AIP Publishing, 2016, 020016.
[415] J.-C. Huang, C.-S. Yang, T. Kohda, H. Kitamura, C.-K. Yang, Performance of TPS cryogenic permanent magnet undulators at NSRRC, 2019, pp. 1559–1561.
[416] J.-C. Huang, H. Kitamura, C.-S. Yang, C.-K. Yang, S. Mizumoto, C.-H. Chang, C.-H. Chang, C.-S. Hwang, Development of cryogenic permanent magnet undulators at NSRRC, in: AIP Conference Proceedings, 2054, (1) AIP Publishing, 2019, 030022.
[417] Y. Yang, H. Lu, S. Sun, X. Zhang, Field error correction considerations of cryogenic permanent magnet undulator (CPMU) for high energy photon source test facility (HEPS-TF), in: 7th International Particle Accelerator Conference (IPAC'16), Busan, Korea, May 8-13, 2016, JACOW, Geneva, Switzerland, 2016, pp. 4038–4040.
[418] H. Lu, Z. Li, W. Chen, L. Gong, S. Zhao, X. Zhang, Y. Sun, L. Zhang, X.Y. Li, S. Sun, et al., Development of a PrFeB cryogenic permanent magnet undulator (cpmu) prototype at IHEP, in: Proceedings of IPAC2017, Copenhagen, Denmark, JACOW, Geneva, Switzerland.
[419] C.-K. Yang, C.-H. Chang, C.-S. Hwang, J.-C. Huang, T.-Y. Chung, Y.Y. Lin, Design of a System at NSRRC to Measure the Field for an In-vacuum Cryogenic Undulator with Permanent Magnet, in: Proceedings of the 5th International Particle Accelerator Conference (IPAC2014), Dresden, Germany, 2014, pp. 2041–2043.
[420] H. Wang, J. Zhang, M. Qian, W. Zhang, Y. Ding, Q. Zhou, The magnetic field measurement systems for a cryogenic undulator and a superconducting undulator at SSRF, in: Journal of Physics: Conference Series, 1067, (8) IOP Publishing, 2018, 082016.
[421] T. Tanaka, T. Hara, T. Bizen, T. Seike, R. Tsuru, X. Marechal, H. Hirano, M. Morita, H. Teshima, S. Nariki, et al., Development of cryogenic permanent undulators operating around liquid nitrogen temperature, New J. Phys. 8 (11) (2006) 287.
[422] O. Chubar, J. Bengtsson, A. Blednykh, C. Kitegi, G. Rakowsky, T. Tanabe, J. Clarke, Segmented adaptive-gap in-vacuum undulators-potential solution for beamlines requiring high hard X-Ray flux and brightness in medium energy synchrotron sources? in: Journal of Physics: Conference Series, 425, (3) IOP Publishing, 2013, 032005.
[423] K.-J. Kim, Circular polarization with crossed-planar undulators in high-gain FELs, Nucl. Instrum. Methods Phys. Res. A 445 (1–3) (2000) 329–332.
[424] H. Onuki, Elliptically polarized synchrotron radiation source with crossed and retarded magnetic fields, Nucl. Instrum. Methods Phys. Res. A 246 (1–3) (1986) 94–98.
[425] T. Schmidt, M. Calvi, Apple x undulator for the swissfel soft X-ray beamline athos, Synchrotron Radiat. News 31 (3) (2018) 35–40.
[426] T. Tanaka, X.-M. Maréchal, T. Hara, T. Tanabe, H. Kitamura, In-vacuum figure-8 undulator for hard X-rays with both horizontal and vertical polarization, J. Synchrotron Radiat. 5 (3) (1998) 412–413.
[427] T. Hara, T. Tanaka, T. Seike, T. Bizen, X. Maréchal, T. Kohda, K. Inoue, T. Oka, T. Suzuki, N. Yagi, et al., In-vacuum x-ray helical undulator for high flux beamline at spring-8, Nucl. Instrum. Methods Phys. Res. A 467 (2001) 165–168.
[428] A.B. Temnykh, Delta undulator for Cornell energy recovery linac, Phys. Rev. Special Top. Accelerators Beams 11 (12) (2008) 120702.
[429] J. Bahrdt, S. Grimmer, In-vacuum APPLE II undulator with force compensation, in: AIP Conference Proceedings, 2054, (1) AIP Publishing, 2019, 030031.
[430] J. Clarke, T. Bradshaw, Superconducting undulator workshop report, ICFA Beam Dyn. Newsl. 65 (2014) 148.
[431] S. Casalbuoni, A. Cecilia, S. Gerstl, N. Glamann, A. Grau, T. Holubek, C. Meuter, D. Saez de Jauregui, R. Voutta, C. Boffo, T. Gerhard, M. Turenne, W. Walter, Recent Developments on Superconducting Undulators at ANKA, in: Proceedings of IPAC2015, Richmond, USA, 2015, p. 2485.
[432] Y. Ivanyushenkov, C. Doose, J. Fuerst, K. Harkay, Q. Hasse, M. Kasa, D. Skiadopoulos, E. Trakhtenberg, Y. Shiroyanagi, E. Gluskin, Development and Performance of 1.1-m Long Superconducting Undulator at the Advanced Photon Source, in: Proceedings of IPAC2015, Richmond, USA, 2015, p. 1794.
[433] J. Bahrdt, E. Gluskin, Cryogenic permanent magnet and superconducting undulators, Nuclear Instrum. Methods A 907 (2018) 149–168, http://dx.doi.org/10.1016/j.nima.2018.03.069.
[434] P. Emma, N. Holtkamp, H.-D. Nuhn, D. Arbelaez, J. Corlett, S. Myers, S. Prestemon, R. Schlueter, C. Doose, J. Fuerst, Q. Hasse, Y. Ivanyushenkov, M. Kasa, G. Pile, E. Trakhtenberg, E. Gluskin, A Plan for the Development of Superconducting Undulator Prototypes for LCLS-II and Future FELs, in: Proceedings of FEL2014, Basel, Switzerland, 2014, p. 649.
[435] Y. Ivanyushenkov, Magnetic Simulation of a Superconducting Undulator for the Advanced Photon Source, in: Proceedings of PAC09, Vancouver, BC, Canada, 2009, p. 310.
[436] I. Kesgin, Y. Ivanyushenkov, E. Gluskin, ICFA Beam Dyn. Newsl. (2019).
[437] G. Elwood, V. Bayliss, S. Canfer, T. Bradshaw, J. Clarke, Final prototype SC helical undulator measured, 2013, EuCARD-REP-2013-016.
[438] J. Corlett, Design Concepts for a Next Generation Light Source at LBNL, in: Proceedings of FEL2013, New York, NY, USA, 2013, p. 193.
[439] J. Clarke, V. Bayliss, T. Bradshaw, S. Brown, A. Brummitt, G. Burton, S. Canfer, B. Green, S. Hughes, E. Longhi, J. Schouten, B. Shepherd, S. Watson, Status of the UK Superconducting Planar Undulator Project, in: Proceedings of IPAC2013, Shanghai, China, 2013, p. 2259.
[440] Y. Ivanyushenkov, Advances in Superconducting Undulators, in: Proceedings of PAC2013, Pasadena, CA USA, 2013, p. 1468.

[441] S. Casalbuoni, A. Cecilia, S. Gerstl, N. Glamann, A. Grau, T. Holubek, C. Meuter, D. Saez de Jauregui, R. Voutta, C. Boffo, T. Gerhard, M. Turenne, W. Walter, Characterization and long term operation of a novel superconducting undulator with 15 mm period length in a synchrotron light source, Phys. Rev. Acc. Beams 19 (2016) 110702.
[442] S. Casalbuoni, N. Glamann, A. Grau, T. Holubek, D. Saez de Jauregui, C. Boffo, T. Gerhard, M. Turenne, W. Walter, Field quality of 1.5 m long conduction cooled superconducting undulator coils with 20 mm period length, J. Phys.: Conf. Ser. 874 (2017) 012015.
[443] S. Casalbuoni, N. Glamann, A. Grau, T. Holubek, D. Saez de Jauregui, S. Bauer, C. Boffo, T. Gerhard, M. Turenne, W. Walter, Superconducting undulators: from development towards a commercial product, Synch. Rad. News 31 (2018) 24.
[444] Y. Ivanyushenkov, K. Harkay, M. Borland, R. Dejus, J. Dooling, C. Doose, L. Emery, J. Fuerst, J. Gagliano, Q. Hasse, M. Kasa, P. Kenesei, V. Sajaev, K. Schroeder, N. Sereno, S. Shastri, Y. Shiroyanagi, D. Skiadopoulos, M. Smith, X. Sun, E. Trakhtenberg, A. Xiao, A. Zholents, E. Gluskin, Development and operating experience of a 1.1-m-long superconducting undulator at the advanced photon source, Phys. Rev. Accel. Beams 20 (2017) 100701, http://dx.doi.org/10.1103/PhysRevAccelBeams.20.100701, URL https://link.aps.org/doi/10.1103/PhysRevAccelBeams.20.100701.
[445] Y. Ivanyushenkov, Development and operating experience of a short-period superconducting undulator at the advanced photon source, Phys. Rev. ST Accel. Beams 18 (2015) 040703.
[446] J. Fuerst, Y. Ivanyushenkov, M. Hasse, I. Kesgin, Y. Shiroyanagi, E. Gluskin, Review OF NEW developments IN superconducting UNDULATOR technology at THE aps, in: Proc. of 60th ICFA Advanced Beam Dynamics Workshop on Future Light Sources FLS2018, Shanghai, China, 2018, http://dx.doi.org/10.18429/JACoW-FLS2018-MOA2PL03.
[447] D. Scott, J. Clarke, D. Baynham, V. Bayliss, T. Bradshaw, G. Burton, A. Brummitt, S. Carr, A. Lintern, J. Rochford, O. Taylor, Y. Ivanyushenkov, Demonstration of a high-field short-period superconducting helical undulator suitable for future teV-Scale linear collider positron sources, Phys. Rev. Lett. 107 (2011) 174803, http://dx.doi.org/10.1103/PhysRevLett.107.174803, URL https://link.aps.org/doi/10.1103/PhysRevLett.107.174803.
[448] J. Clarke, K. Marinov, B. Shepherd, N. Thompson, V. Bayliss, J. Boehm, T. Bradshaw, A. Brummitt, S. Canfer, M. Courthold, B. Green, T. Hayler, P. Jeffery, C. Lockett, D. Wilsher, S. Milward, E. Rial, Optimization OF superconducting undulators FOR low repetition rate FELS, in: Proc. of 38th International Free Electron Laser Conference FEL2017, Santa Fe, NM, USA, 2017, p. 403, http://dx.doi.org/10.18429/JACoW-FEL2017-WEC02.
[449] F. Nguyen, A. Aksoy, A. Bernhard, M. Calvi, J.A. Clarke, H.M. Castañeda Cortés, A.W. Cross, G. Dattoli, D. Dunning, R. Geometrante, et al., XLS Deliverable D5.1: Technologies for the CompactLight undulator, 2019, https://www.compactlight.eu/uploads/Main/D5.1_XLS_Final.pdf.
[450] Y. Ding, P. Baxevanis, Y. Cai, Z. Huang, R. Ruth, High-gain X-ray FELs using a transverse gradient undulator in a diffraction-limited storage ring, in: Proceedings of the International Particle Accelerator Conference IPAC2013, 2013, p. WEPWA075.
[451] H. Deng, C. Feng, Using off-resonance laser modulation for beam energy spread cooling in generation of short-wavelength radiation, Phys. Rev. Lett. 111 (2013) 084801, http://dx.doi.org/10.1103/PhysRevLett.111.084801, arXiv:1305.7041v1.
[452] P. Baxevanis, Y. Ding, Z. Huang, R. Ruth, 3D theroy of a high-gain free-electron laser based on a transverse gradient undulator, Phys. Rev. ST Accel. Beams 17 (2014) 020701.
[453] F. Wu, Z. Zhang, X. Yang, J. Hu, P. Ji, J. Gui, C. Wang, J. Chen, Y. Peng, X. Liu, et al., Performance improvement of a 200tw/1hz ti: sapphire laser for laser wakefield electron accelerator, Opt. Laser Technol. 131 (2020) 106453.
[454] F. Ciocci, G. Dattoli, E. Sabia, Transverse gradient undulators and FEL operating with large energy spread, Opt. Commun. 356 (2015) 582–588.
[455] A. Bernhard, N. Braun, V.A. Rodrí guez, P. Peiffer, R. Rossmanith, C. Widmann, M. Scheer, Radiation emitted by transverse-gradient undulators, Phys. Rev. Accel. Beams 19 (2016) 090704, http://dx.doi.org/10.1103/PhysRevAccelBeams.19.090704, URL http://link.aps.org/doi/10.1103/PhysRevAccelBeams.19.090704.
[456] V. Afonso Rodríguez, Electromagnetic design, implementation and test of a superconducting undulator with a transverse gradient field amplitude, (Ph.D. thesis), Karlsruhe Institute of Technology, 2015, http://dx.doi.org/10.5445/IR/1000050911.
[457] G. Fuchert, A. Bernhard, S. Ehlers, P. Peiffer, R. Rossmanith, T. Baumbach, A novel undulator concept for electron beams with a very large energy spread, Nucl. Instrum. Methods Phys. Res. A 672 (2012) 33–37.
[458] V. Afonso Rodriguez, A. Bernhard, A. Keilmann, P. Peiffer, R. Rossmanith, C. Widmann, T. Baumbach, M. Nicolai, M. Kaluza, Development of a non-planar superconducting undulator for the JETI-laser-wakefield accelerator, IEEE Trans. Appl. Supercond. 23 (3 Part 2) (2013) 4101505.
[459] M. Calvi, C. Camenzuli, E. Prat, T. Schmidt, Transverse gradient in apple-type undulators, J. Synchrotron Radiat. 24 (3) (2017) 600–608, http://dx.doi.org/10.1107/S1600577517004726, URL https://doi.org/10.1107/S1600577517004726.
[460] S. Lee, J.-H. Han, Conceptual design of superconducting transverse gradient undulator for PAL-XFEL beamline, in: Proceedings of the 60th ICFA Advanced Beam Dynamics Workshop on Future Light Sources FLS2018, Shanghai, China, 2018, http://dx.doi.org/10.18429/JACoW-FLS2018-WEP2PT033.
[461] Q. Jia, H. Li, Normal planar undulators doubling as transverse gradient undulators, Phys. Rev. Accel. Beams 20 (2017) 020707, http://dx.doi.org/10.1103/PhysRevAccelBeams.20.020707, URL https://link.aps.org/doi/10.1103/PhysRevAccelBeams.20.020707.
[462] T. Liu, T. Zhang, D. Wang, Z. Huang, J. Liu, Beam Transport Line of the LPA-FEL Facility based on Transverse Gradient Undulator, in: Proceedings of IPAC 2016, Busan, Korea, 2016.
[463] T. Liu, T. Zhang, D. Wang, Z. Huang, Compact beam transport system for free-electron lasers driven by a laser plasma accelerator, Phys. Rev. Accel. Beams 20 (2017) 020701, http://dx.doi.org/10.1103/PhysRevAccelBeams.20.020701, URL https://link.aps.org/doi/10.1103/PhysRevAccelBeams.20.020701.
[464] V. Afonso Rodriguez, A. Bernhard, A. Grau, P. Peiffer, R. Rossmanith, M. Weber, C. Widmann, A. Will, M. Kaluza, M. Nicolai, A. Sävert, M. Reuter, Construction and first magnetic field test of a superconducting transversal gradient undulator for the laser wakefield accelerator in Jena, in: Proceedings of the International Particle Accelerator Conference IPAC2014, 2014.
[465] A. Bernhard, V.A. Rodriguez, S. Kuschel, M. Leier, P. Peiffer, A. Saevert, M. Schwab, W. Werner, C. Widmann, A. Will, et al., Progress on experiments towards LWFA-driven transverse gradient undulator-based FELs, Nucl. Instrum. Methods Phys. Res. A 909 (2018) 391–397.
[466] G. Dattoli, L. Giannessi, P. Ottaviani, H. Freund, S. Biedron, S. Milton, Two harmonic undulators and harmonic generation in high gain free electron lasers, Nucl. Instrum. Methods Phys. Res. A 495 (1) (2002) 48–57, http://dx.doi.org/10.1016/S0168-9002(02)01281-0, URL http://www.sciencedirect.com/science/article/pii/S0168900202012810.
[467] G. Dattoli, A. Doria, L. Giannessi, P. Ottaviani, Bunching and exotic undulator configurations in SASE FELs, in: K.-J. Kim, S. Milton, E. Gluskin (Eds.), Free Electron Lasers 2002, Elsevier, Amsterdam, 2003, pp. 388–391, http://dx.doi.org/10.1016/B978-0-444-51417-2.50091-2, URL http://www.sciencedirect.com/science/article/pii/B9780444514172500912.
[468] G. Dattoli, V. Mikhailin, P. Ottaviani, K.V. Zhukovsky, Two-frequency undulator and harmonic generation by an ultrarelativistic electron, J. Appl. Phys. 100 (8) (2006) 084507, http://dx.doi.org/10.1063/1.2357841.
[469] G. Dattoli, N. Mirian, E. DiPalma, V. Petrillo, Two-color free-electron laser with two orthogonal undulators, Phys. Rev. ST Accel. Beams 17 (5) (2014) 050702, http://dx.doi.org/10.1103/PhysRevSTAB.17.050702.
[470] M. Asakawa, N. Inoue, K. Mima, S. Nakai, K. Imasaki, M. Fujita, J. Chen, C. Yamanaka, N. Nakao, T. Agari, et al., Development of a modified wiggler for higher harmonic lasing of a free-electron laser, Nucl. Instrum. Methods Phys. Res. A 358 (1–3) (1995) 399–402.
[471] G. Dattoli, G. Voykov, Spectral properties of two-harmonic undulator radiation, Phys. Rev. E 48 (4) (1993) 3030.
[472] D.H. Whittum, A.M. Sessler, J.M. Dawson, Ion-channel laser, Phys. Rev. Lett. 64 (1990) 2511–2514, http://dx.doi.org/10.1103/PhysRevLett.64.2511, URL http://link.aps.org/doi/10.1103/PhysRevLett.64.2511.

[473] R. Williams, C. Clayton, C. Joshi, T. Katsouleas, Studies of classical radiation emission from plasma wave undulators, IEEE Trans. Plasma Sci. 21 (1) (1993) 156–166, http://dx.doi.org/10.1109/27.221115.
[474] S. Corde, K. Ta Phuoc, Plasma wave undulator for laser-accelerated electrons, Phys. Plasmas (1994-Present) 18 (3) (2011) 033111, http://dx.doi.org/10.1063/1.3569827, URL http://scitation.aip.org/content/aip/journal/pop/18/3/10.1063/1.3569827.
[475] S. Rykovanov, C. Schroeder, E. Esarey, C.R. Geddes, W. Leemans, Plasma undulator based on laser excitation of wakefields in a plasma channel, Phys. Rev. Lett. 114 (2015) 145003, http://dx.doi.org/10.1103/PhysRevLett.114.145003, URL http://link.aps.org/doi/10.1103/PhysRevLett.114.145003.
[476] J. Luo, M. Chen, M. Zeng, J. Vieira, L. Yu, S. Weng, L. Silva, D. Jaroszynski, Z. Sheng, J. Zhang, A compact tunable polarized X-ray source based on laser-plasma helical undulators, Sci. Rep. 6 (2016) 29101, http://dx.doi.org/10.1038/srep29101, URL http://dx.doi.org/10.1038/srep29101.
[477] I. Andriyash, R. Lehe, A. Lifschitz, C. Thaury, J.-M. Rax, K. Krushelnick, V. Malka, An ultracompact X-ray source based on a laser-plasma undulator, Nature Commun. 5 (2014) http://dx.doi.org/10.1038/ncomms5736.
[478] R. Pantell, G. Soncini, H. Puthoff, Stimulated photon-electron scattering, IEEE J. Quantum Electron. 4 (11) (1968) 905–907.
[479] T. Shintake, Experimental results of microwave undulator, Proc. SPIE 0582 (1986) 0582 – 0582 – 8, http://dx.doi.org/10.1117/12.950944.
[480] S. Tantawi, M. Shumail, J. Neilson, G. Bowden, C. Chang, E. Hemsing, M. Dunning, Experimental demonstration of a tunable microwave undulator, Phys. Rev. Lett. 112 (2014) 164802, http://dx.doi.org/10.1103/PhysRevLett.112.164802.
[481] M. Shumail, S.G. Tantawi, Theory of electromagnetic insertion devices and the corresponding synchrotron radiation, Phys. Rev. Accel. Beams 19 (2016) 074001, http://dx.doi.org/10.1103/PhysRevAccelBeams.19.074001.
[482] L. Zhang, W. He, J. Clarke, K. Ronald, A. Phelps, A. Cross, Microwave undulator using a helically corrugated waveguide, IEEE Trans. Electron Devices 65 (12) (2018) 5499–5504, http://dx.doi.org/10.1109/TED.2018.2873726.
[483] L. Zhang, W. He, J. Clarke, K. Ronald, A.D. Phelps, A. Cross, Systematic study of a corrugated waveguide as a microwave undulator, J. Synchrotron Radiat. 26 (1) (2019) 11–17.
[484] J. Gea-Banacloche, G. Moore, R. Schlicher, M. Scully, H. Walther, Soft X-ray free-electron laser with a laser undulator, IEEE J. Quantum Electron. 23 (9) (1987) 1558–1570.
[485] A. Bacci, C. Maroli, V. Petrillo, A. Rossi, L. Serafini, P. Tomassini, Compact X-ray free-electron laser based on an optical undulator, Nucl. Instrum. Methods Phys. Res. A 587 (2–3) (2008) 388–397.
[486] K. Steiniger, M. Bussmann, R. Pausch, T. Cowan, A. Irman, A. Jochmann, R. Sauerbrey, U. Schramm, A. Debus, Optical free-electron lasers with traveling-wave thomson-scattering, J. Phys. B: At. Mol. Opt. Phys. 47 (23) (2014) 234011.
[487] P.A. Walker, P. Alesini, A. Alexandrova, M.P. Anania, N. Andreev, I. Andriyash, A. Aschikhin, R. Assmann, T. Audet, A. Bacci, et al., Horizon 2020 EuPRAXIA design study, in: Journal of Physics: Conference Series, 874, (1) IOP Publishing, 2017, 012029.
[488] R. Lehe, C. Thaury, E. Guillaume, A. Lifschitz, V. Malka, Laser-plasma lens for laser-wakefield accelerators, Phys. Rev. Special Top. Accelerators Beams 17 (12) (2014) 121301.
[489] S.C. Gottschalk, K. Kangas, T.E. DeHart, J.T. Volk, C.M. Spencer, Performance of an adjustable strength permanent magnet quadrupole, in: Proceedings of the Particle Accelerator Conference, 2005. PAC 2005, IEEE, 2005, pp. 2071–2073.
[490] T. Mihara, Y. Iwashita, M. Kumada, C.M. Spencer, Variable permanent magnet quadrupole, IEEE Trans. Appl. Supercond. 16 (2) (2006) 224–227.
[491] B.J. Shepherd, J.A. Clarke, N. Marks, N.A. Collomb, J.A. Richmond, Novel adjustable permanent magnet quadrupoles for the CLIC drive beam decelerator, IEEE Trans. Appl. Supercond. 22 (3) (2012) 4004204.
[492] G. Tosin, P.P. Sanchez, J.F. Citadini, C.C. Vergasta, Super hybrid quadrupoles, Nucl. Instrum. Methods Phys. Res. A 674 (2012) 67–73.
[493] J.T. Volk, J. DiMarco, G. Foster, W. Fowler, V. Kashikhin, A. Makarov, V. Tsvetkov, C. Rago, A. Ringwall, C. Spencer, et al., Adjustable permanent quadrupoles for the next linear collider, in: Particle Accelerator Conference, 2001. PAC 2001. Proceedings of the 2001, 1, IEEE, 2001, pp. 217–219.
[494] F. Marteau, A. Ghaith, P. N'Gotta, C. Benabderrahmane, M. Valléau, C. Kitegi, A. Loulergue, J. Vétéran, M. Sebdaoui, T. André, et al., Variable high gradient permanent magnet quadrupole (QUAPEVA), Appl. Phys. Lett. 111 (25) (2017) 253503.
[495] C. Benabderrahmane, M. Couprie, F. Forest, O. Cosson, Adjustable magnetic multipole, Europe : PCT/EP2015/069649 of 27/08/2015, WOBL14SSOQUA / CA.
[496] A. Ghaith, D. Oumbarek, C. Kitégi, M. Valléau, F. Marteau, M.-E. Couprie, Permanent magnet-based quadrupoles for plasma acceleration sources, Instruments 3 (2) (2019) 27.
[497] J. Van Tilborg, S. Barber, C. Benedetti, C. Schroeder, F. Isono, H.-E. Tsai, C. Geddes, W. Leemans, Comparative study of active plasma lenses in high-quality electron accelerator transport lines, Phys. Plasmas 25 (5) (2018) 056702.
[498] T. Seggebrock, A. Maier, I. Dornmair, F. Grüner, Bunch decompression for laser-plasma driven free-electron laser demonstration schemes, Phys. Rev. Special Top. Accelerators Beams 16 (7) (2013) 070703.
[499] A. Loulergue, M. Labat, C. Evain, C. Benabderrahmane, V. Malka, M. Couprie, Beam manipulation for compact laser wakefield accelerator based free-electron lasers, New J. Phys. 17 (2) (2015) 023028.
[500] N. Kroll, P. Morton, M. Rosenbluth, J. Eckstein, J. Madey, Theory of the transverse gradient wiggler, IEEE J. Quantum Electron. 17 (8) (1981) 1496–1507.
[501] C. Schroeder, E. Esarey, W. Leemans, J.v. Tilborg, F. Gruener, A. Maier, Y. Ding, Z. Huang, Free-electron lasers driven by laser-plasma accelerators using decompression or dispersion, in: Proceedings of FEL2013, New York, NY, USA, 2013, pp. 117–121.
[502] A. Maier, N. Kajumba, A. Guggenmos, C. Werle, J. Wenz, N. Delbos, B. Zeitler, I. Dornmair, J. Schmidt, E. Gullikson, F. Krausz, U. Schramm, U. Kleineberg, S. Karsch, F. Grüner, Water-window X-Ray pulses from a laser-plasma driven undulator, Sci. Rep. 10 (2020) 5634, http://dx.doi.org/10.1038/s41598-020-62401-4.
[503] M. Couprie, C. Benabderrahmane, P. Betinelli, F. Bouvet, A. Buteau, L. Cassinari, J. Daillant, J. Denard, P. Eymard, B. Gagey, et al., The LUNEX5 project in France, in: Journal of Physics: Conference Series, 425, (7) IOP Publishing, 2013, 072001.
[504] M.-E. Couprie, T. Andre, I. Andriyash, Coxinel: Towards free electron laser amplification to qualify laser plasma acceleration, Reza Kenkyu 45 (2) (2017) 94–98.
[505] K. Halbach, Design of permanent multipole magnets with oriented rare earth cobalt material, Nucl. Instrum. Methods 169 (1) (1980) 1–10.
[506] E. Roussel, T. Andre, I. Andriyash, F. Blache, F. Bouvet, S. Corde, D. Oumbarek-Espinos, A. Ghaith, J.-P. Goddet, C. Kitegi, et al., Energy spread tuning of a laser-plasma accelerated electron beam in a magnetic chicane, Plasma Phys. Control. Fusion (2020).
[507] M. Labat, M. El Ajjouri, N. Hubert, T. Andre, A. Loulergue, M.-E. Couprie, Electron and photon diagnostics for plasma acceleration-based FELs, J. Synchrotron Radiat. 25 (1) (2018) 59–67.
[508] A. Ghaith, A. Loulergue, D. Oumbarek, O. Marcouillé, M. Valléau, M. Labat, S. Corde, M.-E. Couprie, Electron beam brightness and undulator radiation brilliance for a laser plasma acceleration based free electron laser, Instruments 4 (1) (2020) 1.
[509] M.-E. Couprie, T. André, I. Andriyash, S. Bielawski, F. Blache, F. Bouvet, F. Briquez, S. Corde, Y. Dietrich, J.-P. Duval, et al., Control of laser plasma accelerated electrons: A route for compact free electron lasers, in: 10th Int. Partile Accelerator Conf.(IPAC'19), Melbourne, Australia, 19-24 May 2019, JACOW Publishing, Geneva, Switzerland, 2019, pp. 2280–2285.
[510] D.O. Espinos, A. Ghaith, A. Loulergue, T. André, C. Kitégi, M. Sebdaoui, F. Marteau, F. Blache, M. Valléau, M. Labat, et al., Coxinel transport of laser plasma accelerated electrons, Plasma Phys. Control. Fusion 62 (3) (2020) 034001.

[511] D. Oumbarek Espinos, A. Ghaith, T. André, C. Kitégi, M. Sebdaoui, A. Loulergue, F. Marteau, F. Blache, M. Valléau, M. Labat, et al., Skew quadrupole effect of laser plasma electron beam transport, Appl. Sci. 9 (12) (2019) 2447.
[512] L. Giannessi, M. Bellaveglia, E. Chiadroni, A. Cianchi, M. Couprie, M. Del Franco, G. Di Pirro, M. Ferrario, G. Gatti, M. Labat, et al., Superradiant cascade in a seeded free-electron laser, Phys. Rev. Lett. 110 (4) (2013) 044801.
[513] G. Lambert, T. Hara, D. Garzella, T. Tanikawa, M. Labat, B. Carre, H. Kitamura, T. Shintake, M. Bougeard, S. Inoue, et al., Injection of harmonics generated in gas in a free-electron laser providing intense and coherent extreme-ultraviolet light, Nat. Phys. 4 (4) (2008) 296–300.
[514] T. Tanikawa, G. Lambert, T. Hara, M. Labat, Y. Tanaka, M. Yabashi, O. Chubar, M. Couprie, Nonlinear harmonic generation in a free-electron laser seeded with high harmonic radiation, Europhys. Lett. 94 (3) (2011) 34001.
[515] N. Delbos, C. Werle, I. Dornmair, T. Eichner, L. Hübner, S. Jalas, S. Jolly, M. Kirchen, V. Leroux, P. Messner, M. Schnepp, M. Trunk, P. Walker, P. Winkler, A. Maier, Lux – a laser-plasma driven undulator beamline, Nucl. Instrum. Methods Phys. Res. A 909 (2018) 318, http://dx.doi.org/10.1016/j.nima.2018.01.082.
[516] C. Werle, First undulator experiments at the LUX beamline, (Ph.D. thesis), Universität Hamburg, 2019.
[517] M. Labat, A. Loulergue, T. Andre, I. Andriyash, A. Ghaith, M. Khojoyan, F. Marteau, M. Valléau, F. Briquez, C. Benabderrahmane, et al., Robustness of a plasma acceleration based free electron laser, Phys. Rev. Accel. Beams 21 (11) (2018) 114802.
[518] S. Reiche, Genesis 1.3: a fully 3D time-dependent FEL simulation code, Nucl. Instrum. Methods Phys. Res. A 429 (1–3) (1999) 243–248.
[519] I. Andriyash, R. Lehe, V. Malka, A spectral unaveraged algorithm for free electron laser simulations, J. Comput. Phys. 282 (2015) 397–409, http://dx.doi.org/10.1016/j.jcp.2014.11.026, URL https://www.sciencedirect.com/science/article/pii/S0021999114007888.
[520] M. Labat, S. Bielawski, A. Loulergue, S. Corde, M.-E. Couprie, E. Roussel, Interferometry for full temporal reconstruction of laser-plasma accelerator-based seeded free electron lasers, New J. Phys. (2020).
[521] A. Maier, A. Meseck, S. Reiche, C. Schroeder, T. Seggebrock, F. Gruener, Demonstration scheme for a laser-plasma-driven free-electron laser, Phys. Rev. X 2 (3) (2012) 031019.
[522] H.-E. Tsai, K.K. Swanson, S.K. Barber, R. Lehe, H.-S. Mao, D.E. Mittelberger, S. Steinke, K. Nakamura, J. van Tilborg, C. Schroeder, et al., Control of quasi-monoenergetic electron beams from laser-plasma accelerators with adjustable shock density profile, Phys. Plasmas 25 (4) (2018) 043107.
[523] M. Borland, Elegant: A flexible SDDS-compliant code for accelerator simulation, Adv. Photon Source LS-287 (2000) http://dx.doi.org/10.2172/761286.
[524] J. Tilborg, Progress towards BELLA center's laser-plasma accelerator based free electron laser, 2019, URL: https://agenda.infn.it/event/17304/timetable/?view=standard.
[525] J. van Tilborg, M. Ambat, S. Barber, F. Isono, W. Leemans, C. Schroeder, et al., Progress towards BELLA center's free electron laser driven by a laser plasma accelerator, in: Proc. of ICFA Advanced Beam Dynamics Workshop (FLS'18), JACoW, 2018.
[526] S. Barber, J. van Tilborg, C. Schroeder, R. Lehe, H.-E. Tsai, K. Swanson, S. Steinke, K. Nakamura, C. Geddes, C. Benedetti, et al., Measured emittance dependence on the injection method in laser plasma accelerators, Phys. Rev. Lett. 119 (10) (2017) 104801.
[527] C. Widmann, V.A. Rodriguez, S. Kuschel, M. Nicolai, R. Rossmanith, A. Sävert, M. Schwab, W. Werner, M. Kaluza, A. Bernhard, et al., First tests of a beam transport system from a laser wakefield accelerator to a transverse gradient undulator, Gas 1 (Q2) (2015) Q3.
[528] C. Widmann, Simulation and first experimental tests of an electron beam transport system for a laser wakefield accelerator, (Ph.D. thesis), Karlsruher Institut für Technologie (KIT), 2016.
[529] F. Nguyen, A. Bernhard, A. Chancé, M.-E. Couprie, G. Dattoli, C. Lechner, A. Marocchino, G. Maynard, A. Petralia, A.R. Rossi, Free electron laser performance within the EuPRAXIA facility, Instruments 4 (1) (2020) http://dx.doi.org/10.3390/instruments4010005, URL https://www.mdpi.com/2410-390X/4/1/5.
[530] P. Tomassini, S. De Nicola, L. Labate, P. Londrillo, R. Fedele, D. Terzani, L.A. Gizzi, The resonant multi-pulse ionization injection, Phys. Plasmas 24 (10) (2017) 103120, http://dx.doi.org/10.1063/1.5000696, URL https://doi.org/10.1063/1.5000696.
[531] P. Tomassini, S. Nicola, L. Labate, P. Londrillo, R. Fedele, D. Terzani, F. Nguyen, G. Vantaggiato, L. Gizzi, Nucl. Instrum. Methods Phys. Res. A 909 (2018) 1, http://dx.doi.org/10.1016/j.nima.2018.03.002, 3rd European Advanced Accelerator Concepts workshop (EAAC2017).
[532] P. Tomassini, D. Terzani, L. Labate, G. Toci, A. Chance, P.A.P. Nghiem, L.A. Gizzi, High quality electron bunches for a multistage GeV accelerator with resonant multipulse ionization injection, Phys. Rev. Accel. Beams 22 (2019) 111302, http://dx.doi.org/10.1103/PhysRevAccelBeams.22.111302, URL https://link.aps.org/doi/10.1103/PhysRevAccelBeams.22.111302.
[533] X. Li, A. Mosnier, P.A.P. Nghiem, Design of a 5 GeV laser–plasma accelerating module in the quasi-linear regime, Nucl. Instrum. Methods Phys. Res. A 909 (2018) 49–53, http://dx.doi.org/10.1016/j.nima.2018.02.104, URL http://www.sciencedirect.com/science/article/pii/S0168900218302924, 3rd European Advanced Accelerator Concepts workshop (EAAC2017).
[534] X. Li, P.A.P. Nghiem, A. Mosnier, Toward low energy spread in plasma accelerators in quasilinear regime, Phys. Rev. Accel. Beams 21 (2018) http://dx.doi.org/10.1103/PhysRevAccelBeams.21.111301.
[535] A. Rossi, A. Bacci, M. Belleveglia, E. Chiadroni, A. Cianchi, G. Pirro, M. Ferrario, A. Gallo, G. Gatti, C. Maroli, A. Mostacci, V. Petrillo, L. Serafini, P. Tomassini, C. Vaccarezza, Nucl. Instrum. Methods Phys. Res. A 740 (2014) 60, http://dx.doi.org/10.1016/j.nima.2013.10.063, Proceedings of the first European Advanced Accelerator Concepts Workshop 2013.
[536] A. Giribono, A. Bacci, E. Chiadroni, A. Cianchi, M. Croia, M. Ferrario, A. Marocchino, V. Petrillo, R. Pompili, S. Romeo, M. Conti, A. Rossi, C. Vaccarezza, Nucl. Instrum. Methods Phys. Res. A 909 (2018) 282, http://dx.doi.org/10.1016/j.nima.2018.03.009, 3rd European Advanced Accelerator Concepts workshop (EAAC2017).
[537] A. Rossi, V. Petrillo, A. Bacci, E. Chiadroni, A. Cianchi, M. Ferrario, A. Giribono, A. Marocchino, M.R. Conti, L. Serafini, C. Vaccarezza, Plasma boosted electron beams for driving free electron lasers, Nucl. Instrum. Methods Phys. Res. A 909 (2018) 54–57, http://dx.doi.org/10.1016/j.nima.2018.02.092, URL http://www.sciencedirect.com/science/article/pii/S0168900218302730, 3rd European Advanced Accelerator Concepts workshop (EAAC2017).
[538] X. Li, A. Chancé, P.A.P. Nghiem, Preserving emittance by matching out and matching in plasma wakefield acceleration stage, Phys. Rev. Accel. Beams 22 (2019) 021304, http://dx.doi.org/10.1103/PhysRevAccelBeams.22.021304, URL https://link.aps.org/doi/10.1103/PhysRevAccelBeams.22.021304.
[539] M.R. Conti, A. Bacci, A. Giribono, V. Petrillo, A. Rossi, L. Serafini, C. Vaccarezza, Electron beam transfer line design for plasma driven free electron lasers, Nucl. Instrum. Methods Phys. Res. A 909 (2018) 84–89, http://dx.doi.org/10.1016/j.nima.2018.02.061, URL http://www.sciencedirect.com/science/article/pii/S0168900218302158, 3rd European Advanced Accelerator Concepts workshop (EAAC2017).
[540] R. Akre, L. Bentson, P. Emma, P. Krejcik, A transverse RF deflecting structure for bunch length and phase space diagnostics, in: PACS2001. Proceedings of the 2001 Particle Accelerator Conference (Cat. No.01CH37268), vol. 3, 2001, pp. 2353–2355, http://dx.doi.org/10.1109/PAC.2001.987379.
[541] J. Kennedy, R. Eberhart, Particle swarm optimization, in: Proceedings of ICNN'95 - International Conference on Neural Networks, 4, 1995, pp. 1942–1948 vol.4, http://dx.doi.org/10.1109/ICNN.1995.488968.
[542] M. Hestenes, E. Stiefel, Methods of conjugate gradients for solving linear systems, J. Res. NIST 49 (6) (1952) 409–436, http://dx.doi.org/10.6028/jres.049.044, URL http://dx.doi.org/10.6028/jres.049.044.

[543] D. Uriot, N. Pichoff, Status of TraceWin code, in: Proceedings, 6th International Particle Accelerator Conference (IPAC 2015): Richmond, Virginia, USA, May 3-8, 2015, 2015, p. MOPWA008, http://dx.doi.org/10.18429/JACoW-IPAC2015-MOPWA008, URL http://accelconf.web.cern.ch/AccelConf/IPAC2015/papers/mopwa008.pdf.
[544] K. Floettmann, et al., Astra: A space charge tracking algorithm, Manual, Version 3 (2011) 2014, URL http://www.desy.de/~mpyflo/Astra_manual/Astra-Manual_V3.2.pdf.
[545] R.W. Assmann, M.K. Weikum, T. Akhter, D. Alesini, A. Alexandrova, M.P. Anania, N. Andreev, I. Andriyash, M. Artioli, A. Aschikhin, et al., Eupraxia conceptual design report, 2019, http://www.eupraxia-project.eu/eupraxia-conceptual-design-report.html.
[546] R. Assmann, M. Weikum, T. Akhter, D. Alesini, A. Alexandrova, M. Anania, N. Andreev, I. Andriyash, M. Artioli, A. Aschikhin, et al., Erratum to: EuPRAXIA conceptual design report, Eur. Phys. J. Spec. Top. 229 (1) (2020) 11–31.
[547] E. Moog, R. Dejus, S. Sasaki, Comparison of achievable magnetic fields with superconducting and cryogenic permanent magnet undulators – A comprehensive study of computed and measured values, Technical Report ANL/APS/LS-348 137001, Argonne National Lab., Argonne – IL (United States), 2017, http://dx.doi.org/10.2172/1372292.
[548] L. Giannessi, OVERVIEW OF PERSEO, A SYSTEM FOR SIMULATING FEL DYNAMICS IN MATHCAD, in: 2006 Free Electron Laser Conference, 2006.
[549] G. Mourou, The nobel prize in physics 2018, in: Chirped Laser Pulse, 2018, https://www.nobelprize.org/prizes/physics/2018/mourou/facts/.